

# Investigation of Magnetization Structures in Ferromagnetic and Superconducting Samples by Magnetic Force Microscopy

INAUGURALDISSERTATION

zur

Erlangung der Würde eines Doktors der Philosophie

vorgelegt der

Philosophisch-Naturwissenschaftlichen Fakultät

der Universität Basel

von

Petrus J. A. van Schendel

aus den Niederlanden

Basel, 1999



Genehmigt von der Philosophisch-Naturwissenschaftlichen Fakultät  
auf Antrag der Herren Professoren:

Prof. Dr. H.-J. Güntherodt  
Prof. Dr. E. Meyer

Basel, den 7. December 1999

Prof. Dr. Andreas Zuberblier

# Contents

<b>List of Figures</b>	<b>ii</b>
<b>List of Symbols</b>	<b>iii</b>
<b>1 Introduction</b>	<b>1</b>
<b>2 Instrument</b>	<b>3</b>
2.1 General Properties of Scanning Force Microscopes . . . . .	3
2.1.1 Tip–Sample Positioning . . . . .	3
2.1.2 The Tip–Sample Interaction . . . . .	5
2.2 Measurement Modes . . . . .	6
2.2.1 Static Modes . . . . .	7
2.2.2 Dynamic Modes . . . . .	7
2.2.3 Comparing the Static and Dynamic Modes . . . . .	10
2.3 Levers and Tips for Magnetic Force Microscopy . . . . .	10
2.3.1 Cantilever Properties . . . . .	10
2.3.2 Geometrical Tip Properties . . . . .	11
2.3.3 Magnetic Tip Properties . . . . .	12
<b>3 Contrast formation</b>	<b>15</b>
3.1 Contrast mechanisms . . . . .	16
3.1.1 Negligible Sample Modification . . . . .	17
3.1.2 Reversible Sample Modification . . . . .	17
3.1.3 Irreversible Sample Modification . . . . .	18
3.2 Calculation of the Contrast . . . . .	18
3.2.1 Magnetostatic Fields in Fourier Space . . . . .	19
3.2.2 Computation of the Force on the Tip . . . . .	20
3.2.3 The Relation between the Force and the Measured Contrast . . . . .	21
3.2.4 The Instrument Calibration Function . . . . .	22
3.2.5 Testing for Negligible Modification . . . . .	23
3.2.6 Calculation of the Field from the Measured Signal . . . . .	24
3.3 Calibration of the Instrument . . . . .	25
3.3.1 Calibration Procedure . . . . .	26
3.3.2 Stray Field of the Tip . . . . .	28
3.4 Evaluation of the Experimental Image Contrast . . . . .	29
3.4.1 Results Obtained with Calibrated Tips . . . . .	30

3.4.2	Point-pole Tip Models . . . . .	32
3.4.3	Tip Model Based on Tip Geometry . . . . .	33
3.5	Comparison of MFM to Other Methods . . . . .	34
<b>4</b>	<b>MFM on Ferromagnetic Layers</b>	<b>37</b>
4.1	Properties of Cu/Ni/Cu/Si(001) . . . . .	38
4.1.1	Micromagnetic Properties . . . . .	38
4.1.2	Orientation of the Magnetization . . . . .	42
4.2	Magnetic Domains . . . . .	44
4.2.1	Stray Field of the Magnetic Domains . . . . .	45
4.2.2	Domain Walls . . . . .	46
4.3	Surface Anisotropy and the Magnetization Structure . . . . .	48
4.3.1	Surface Domains . . . . .	49
4.3.2	Homogeneous Weak Stripes . . . . .	50
4.3.3	Partial Closure Structure . . . . .	52
4.3.4	Domains in 15 nm Ni Samples . . . . .	53
<b>5</b>	<b>MFM on Superconductors</b>	<b>55</b>
5.1	Contrast Formation on Superconductors . . . . .	56
5.1.1	Stray Field due to Meissner Expulsion . . . . .	57
5.1.2	The Vortex Stray Field . . . . .	61
5.2	Evaluation of the Experimental Image Contrast . . . . .	65
5.2.1	Cause of the Vortex Contrast . . . . .	65
5.2.2	Dependence of the Contrast on $\lambda$ and $\xi$ . . . . .	66
<b>6</b>	<b>Conclusion</b>	<b>69</b>
6.1	Instrument . . . . .	69
6.2	Contrast Formation . . . . .	69
6.3	MFM on Ferromagnetic Samples . . . . .	71
6.4	MFM on Superconducting Samples . . . . .	71
<b>A</b>	<b>Stray Field of a Magnetic Layer</b>	<b>73</b>
	<b>Bibliography</b>	<b>74</b>
	<b>Acknowledgments</b>	<b>81</b>
	<b>Curriculum Vitae</b>	<b>83</b>
	<b>List of Publications</b>	<b>84</b>

# List of Figures

2.1	Stray field of the tip and coordinate system. . . . .	4
2.2	Tests of the instrument . . . . .	5
2.3	Comparison of measurement modes . . . . .	8
2.4	Effect of vibration amplitude on the image . . . . .	9
2.5	Tips used in this thesis . . . . .	12
3.1	The effect of the canted orientation of the cantilever . . . . .	22
3.2	Test of exponential decay with distance . . . . .	24
3.3	Flow chart of the calibration process. . . . .	26
3.4	Example of the calibration process. . . . .	27
3.5	Instrument response and noise as a function of $k$ and $\lambda$ . . . . .	28
3.6	magnetic flux density of different tips . . . . .	29
3.7	Average amplitude of the Fourier components of several tip calibration functions as a function of $k$ . . . . .	30
3.8	Effect of different calibrations in direct space. . . . .	31
3.9	Smallest measurable magnetic flux-density as a function of $k$ and $\lambda$ . . . . .	35
4.1	The hierarchy of descriptive levels of magnetic materials . . . . .	37
4.2	Anisotropy of the Cu/Ni/Cu samples . . . . .	42
4.3	Phase diagram for second and fourth order anisotropy . . . . .	43
4.4	Occurrence of a Canted Surface State . . . . .	45
4.5	Wall width as a function of Ni layer thickness . . . . .	47
4.6	Hysteresis loop of the sample containing 200 nm of Ni . . . . .	49
4.7	Measurement and simulations for different wall profiles . . . . .	50
4.8	Schematic representation of considered magnetization structures . . . . .	50
4.9	Magnetization structure for different wall widths . . . . .	51
4.10	Simulated spectra for two wall profiles, compared to measured spectrum . . . . .	52
4.11	Domain structure of a Cu/15 nm Ni/Cu sample . . . . .	53
5.1	Schematic representation of the calculation of the Meissner repulsion . . . . .	58
5.2	Meissner force versus distance curves . . . . .	60
5.3	Behavior of the Vortex stray field for different material parameters . . . . .	63
5.4	Vortex radius for as a function of layer thickness and $\kappa$ . . . . .	64
5.5	MFM Images of the magnetic stray field above a thin layer of $\text{YBa}_2\text{Cu}_3\text{O}_{7-x}$ . . . . .	65
5.6	Fit of the flux density distribution of a single vortex in a thin layer of $\text{YBa}_2\text{Cu}_3\text{O}_{7-x}$ . . . . .	67

# List of symbols

Symbol	Explanation
<b>A</b>	magnetic vector potential
$A$	exchange constant
$a_{Cu}, a_{Ni}$	lattice constants of Cu and Ni
$A_{rms}$	root-mean-squared vibration amplitude of the cantilever
$A_{11}$	2nd order magnetostriction constant
<b>B</b>	magnetic flux density
$B$	measurement bandwidth
$B_1$	(1st order) magnetostriction constant
$c_L$	force constant of the cantilever
$c_{12}, c_{11}$	elastic constants
$d$	thickness of the cantilever beam, sample thickness
$e$	electron charge
$d_c$	critical sample thickness for the formation of dislocations
$d_n$	deflection of the cantilever in the direction normal to its surface
$D_x, D_y$	dipole response functions in x- and y-direction
$d_{\perp, \parallel}$	thickness at which the perpendicular resp. parallel orientation of the magnetization becomes unstable
$E$	Young's modulus
$E_a$	anisotropy energy density
$E_c$	crystal anisotropy energy density
$E_d$	demagnetizing energy density
$E_{me}$	magneto-elastic energy density
$E_s$	surface anisotropy energy density
$E_x$	exchange energy density
$e_0$	biaxial in-plane strain
<b>F</b>	force acting on the cantilever
$f$	frequency of the cantilever vibration
$f_{res}$	resonance frequency of the cantilever
$F_n$	force acting on the cantilever in the direction normal to its surface
$f_0$	free resonance frequency (of the cantilever)

Symbol	Explanation
$g$	arbitrary function in direct space
$G$	arbitrary function in Fourier space
$\mathbf{H}$	stray field
$h$	Planck's constant
$\mathbf{j}$	current density vector
$H_c$	critical field of a superconductor
$\mathbf{k}$	position vector in 2D-Fourier space = $(k_x, k_y)$
$k$	magnitude or length of $\mathbf{k}$
$k_B$	Boltzmann's constant
$K_{c,(1,2)}$	1st and 2nd cubic crystal anisotropy constant
$K_d$	shape anisotropy constant
$K_{me}$	magneto-elastic anisotropy constant
$K_s$	interface anisotropy constant
$k_x, k_y$	x- and y-coordinate of wave vector
$K_{2,4}$	second, fourth order anisotropy constant
$K_{2,4}^{eff}$	second, fourth order effective anisotropy constant
$l$	length of the cantilever beam, an arbitrary closed path
$l_x, l_y$	size of the measurement in x- and y-direction
$LCF$	lever canting function, describes the effect of the canted orientation of the lever
$\mathbf{M}$	magnetization vector
$\mathbf{m}$	dipole moment, normalized magnetization vector
$m$	mass of the cantilever beam, arbitrary integer number
$M_s$	saturation magnetization
$M_v$	magnetization distribution of the vortex core
$m_x, m_y, m_z$	x-, y- and z- component of the dipole moment, x-, y- and z- component of the normalized magnetization vector
$\mathbf{n}$	normal direction (of the cantilever or sample surface)
$n$	arbitrary integer number
$n_{vortex}$	vortex density
$N_x, N_y$	number of measured points in x- and y-direction
$o$	arbitrary integer number
$p$	arbitrary integer number, propagation coefficient
$Q$	quality factor of a resonator
$q_0$	magnetic charge of a monopole tip
$\mathbf{r}$	position vector in 2D-direct space = $(x, y)$
$r$	reflection coefficient, distance from the center of a vortex

Symbol	Explanation
$S$	sensitivity of the measurement, an arbitrary simply connected surface
$S_{dd}$	amplitude spectrum of the displacement noise
$T$	absolute temperature
$t$	time, transmission coefficient
$T_c$	critical temperature (of a superconductor)
$V$	vorticity
$w$	width of the cantilever beam
$x$	x-coordinate (usually coordinate in fast scan direction)
$y$	y-coordinate (usually coordinate in slow scan direction)
$z$	z-coordinate (usually in direction away from the sample surface)
$\gamma_w$	wall surface energy density
$\delta_w$	domain wall thickness
$\theta$	angle between the normal of the cantilever and the normal of the sample surface, angle between the magnetization direction and the normal of the sample surface
$\theta_c$	angle between the stable magnetization direction and the normal of the sample surface in a cone state
$\eta$	lattice mismatch
$\kappa$	Ginsburg–Landau parameter
$\lambda$	wavelength of the magnetic field variation, penetration depth (of a superconductor)
$\lambda_d$	domain period
$\lambda_v$	weighed average vortex radius
$\mu_0$	permeability of free space
$\mu^*$	apparent permeability
$\xi$	coherence length
$\xi_v$	vortex core radius parameter
$\rho$	the specific density of the cantilever beam material
$\rho_M$	magnetic charge density
$\sigma_{ICF}$	standard deviation from the averaged instrument calibration function
$\sigma_M$	magnetic surface charge density
$\sigma_{tip}$	tip-equivalent surface charge distribution
$\phi_M$	magnetic scalar potential
$\phi_0$	superconducting flux quantum
$\phi'$	fluxoid
$\psi$	superconducting order parameter
$\nabla$	nabla operator



# Chapter 1

## Introduction

Even though the phenomenon of magnetic ordering in solids was already known to the ancient Greek<sup>1</sup>, the microscopic understanding of why certain materials show magnetic order dates from this century. In particular, even though some form of magnetic domains was already expected by Weiss when he formulated his theory of Ferromagnetic ordering in 1907 [1], direct experimental evidence of their existence was only provided in 1931 by measurements of v. Hámod and Thiessen [2] and Bitter [3]. In these experiments, the domain structure was determined by the imaging of small magnetic particles that decorate regions with high magnetic stray fields. This decoration is due to the interaction force between these particles and the sample stray field. Interestingly enough, the reason why the domains were formed was still unclear, and was only clarified in 1935 by Landau and Lifschitz.

The phenomenon of Superconductivity on the other hand, was discovered much more recently in 1911 by Kamerlingh Onnes. After its discovery, it took until 1933, when Meissner and Ochsenfeld found that superconductors are ideal diamagnets, repelling the magnetic flux from their inside, even if the field is applied before the superconductor becomes superconductive. Again, the existence of domains was first predicted from the theory published by Landau in 1937, but it took until the fifties before the first magnetic flux structures in superconductors were imaged, again using the decoration technique [4]. Thus, even though the theoretical understanding of the domains in ferromagnets and superconductors evolved almost simultaneously, the first direct observation of the latter took 23 years longer, which was probably due to the experimental difficulties of studying superconductors.

Magnetic force microscopy (MFM) is a relatively new technique for imaging these magnetization structures. It combines the properties of the decoration technique (the contrast formation is due the magnetic interaction between the stray field of the sample and a small magnetic particle) with the properties of the scanning force microscopy technique developed by Binnig, Quate and Gerber [5] (measuring the interaction be-

---

<sup>1</sup>Thales of Miletus, the first person to be active in the field of Phil. II, is generally credited to be the first to have studied electricity and magnetism around 600 BC. Independent from whether this is true or not, it is a fact that the names of both electricity and magnetism are derived from the ancient Greek language: The term electricity is derived from the greek word for amber, *ηλεκτρον*, a substance in which electrostatic charging was observed, the term magnetism is derived from the greek name *Μαγνησια*, an area in northern Greece where magnetic stones were found.

tween the particle and the sample as a function of position through the deflection of a cantilever beam). The first MFM measurements were made on ferromagnets [6, 7]. Again, the first observation of magnetization structures in superconductors took somewhat longer, until 1994 [8]. Nowadays with time and effort, the experimental difficulties of working with MFM at low temperatures have been diminished by the development of better instruments and improved measurement methods. The measurements presented in this thesis were made with such an instrument, the design of which is discussed in chapter 2.

Compared to other types of magnetic imaging,<sup>2</sup> the advantages of the MFM technique are a high spatial resolution imaging and relatively low requirements for sample preparation. Another, unique property of the MFM is that it can be used as a tool for determining the response of the sample to a local applied field and for modifying the sample. One of the main disadvantages of the MFM until now has been the difficulty to interpret the measured signal. In recent years, the improvement in the quality of the instrument and the subsequent improvement of the measurement quality has allowed the development of procedures that allow the quantitative interpretation of the measured contrast. The methods developed for quantitative evaluation of the MFM measurements as part of this thesis-work are described in more detail in chapter 3.

The application of the MFM method to the analysis of ferromagnetic materials is described in chapter 4. A point of interest in the research of these materials is the influence of the interfaces between ferromagnetic and other materials on the magnetic properties of the sample. Here, this influence was studied using Cu/Ni/Cu/Si(001) sandwich structures, because they show a particularly interesting dependence of the preferred orientation of the magnetization on the thickness of the nickel layer.

Finally, the application of the MFM method to the study of superconductors is described in chapter 5. In addition to the imaging of the magnetic structures occurring in the superconductor, the use of the MFM to study the response of the superconductor to a local applied field is discussed.

---

<sup>2</sup>see for example the overview in [9]

## Chapter 2

# Instrument

The experiments in this work were performed with a low-temperature scanning force microscope and its prototype, operated at room-temperature. These instruments were developed and built in the group of Dr. H.J. Hug. Although the design and operation of the instrument has already extensively been described in the literature [10, 11], some of the aspects of the operation of the instrument will be repeated and somewhat expanded on here. This is done to clarify the aspects of scanning force microscopy that are directly relevant to the contrast formation mechanism in magnetic force microscopy. First some of the general properties of scanning force microscopes are discussed in section 2.1 and then the different operation modes in which measurements can be made with these instruments are discussed in section 2.2. Finally, the desired properties of the probe-tip and the cantilever it is mounted on, are discussed in section 2.3.

### 2.1 General Properties of Scanning Force Microscopes

At the core of any scanning force microscope is a flexible cantilever beam, with a tip mounted on its end. During the measurement, the deflection signal of this cantilever is used to determine the interaction between the tip and the sample. To obtain an image of the tip-sample interaction, the tip position is scanned relative to the sample. In this section, the tip-sample positioning system is discussed first, then a general description of the imaged interaction is given.

#### 2.1.1 Tip-Sample Positioning

The instruments used for the measurements, presented in this thesis, has the ability to change the relative tip-sample position by several means. A piezo-tube scanner is used for positioning of the sample with respect to the spatially fixed cantilever with nanometer-scale precision. During scanning, the non-linearities of the tube scanner are compensated using feed-forward compensation [11], to ensure that the measured grid-points are equidistant, and at reproducible positions. In addition to the piezo-tube, two piezo motors are used for changing the tip-sample position with micrometer-scale precision. One motor moves the sample closer or further away from the tip, the other motor moves the cantilever parallel to the sample. To simplify the description of the tip-sample positioning, it is assumed that only the tip moves, and the the sample is

on a fixed position. Then, a coordinate system can be defined as shown in figure 2.1. The  $y$ -direction is parallel to the projection of the cantilever axis on the sample,  $+y$  is the direction along the cantilever, away from the tip. The  $z$ -direction is perpendicular to the sample surface,  $+z$  is the direction away from the sample. The  $x$ -direction is obtained from the cross product of the  $y$ - and  $z$ -direction. According to this definition, the fast scan direction in the instrument (left to right in the images) is usually the  $x$ -direction, whereas in the often used Nanoscope III, the fast scan direction is usually the  $y$ -direction. For the quantitative interpretation of the contrast in MFM (section 3.2, it is important to take into account that the cantilever is not exactly deflected in the  $z$ -direction, but in the direction of of the surface-normal to the cantilever,  $\mathbf{n}$ . In the instrument, the angle,  $\theta$ , between the cantilever normal and the  $z$ -direction is  $-12^\circ$ .

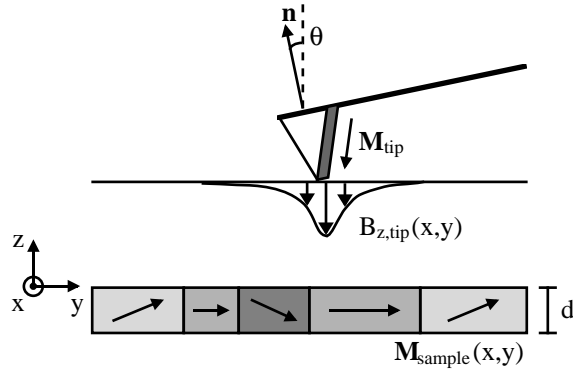


Figure 2.1: Stray field of the tip and coordinate system.

Tests of accuracy of the positioning system were previously described in the thesis work of Bruno Stiefel [10]. To estimate the magnitude of the signal error due to the remaining position errors, two consecutive measurements were made under identical conditions with the prototype instrument, one of which is shown in Fig. 2.2a. The elapsed time between these measurements is approximately 11 minutes. The difference between these measurements is shown in Fig. 2.2b.<sup>1</sup> The root-mean-squared (rms) error between the two, after subtracting the noise (see section 2.1.2), is 0.12 Hz, which is 2 % of the displayed range of values in Fig. 2.2a. Analysis of the difference between these images shows that it is mainly caused by a relative position shift of less than half a pixel, being less than 0.2 % of the scan range. The stability of the tip-to-sample distance was also tested. The distance was determined by the following experimental procedure. After the acquisition of MFM data the scan is stopped. After waiting one minute, the sample is slowly approached towards the tip until the cantilever snaps into contact with the sample. Then the sample is approached further until the cantilever deflection has the same value as it had at the start of the approach. The total displacement is assumed to be the tip-to-sample distance. From repeated measurements it is found that the drift between the start and the end of the measurement (8.5 minutes) is of the order of 1 nm. The errors in the position of the measured grid points may be due to drift of the microscope by thermal expansion, and thermally activated piezo-

<sup>1</sup>Note the difference in the frequency shift scales

creep. However, it is hard to separate between the two. Casual observations on the low temperature instrument show that the lateral position of the tip remains approximately constant over a temperature range of 70 K, and that the tip–sample distance is virtually constant at low temperatures. This suggests that piezo–creep is the main cause for the lateral position errors. On the other hand, the constant tip–sample distance is not necessarily due to reduced creep, but may also be due to a more stable temperature of the microscope.

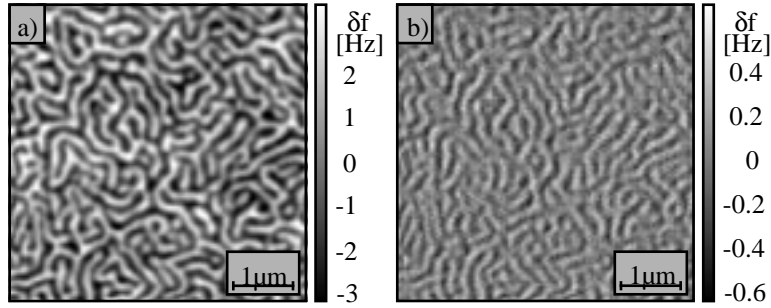


Figure 2.2: Measurements used for estimating magnitude of the signal error due to typical position errors.

- a) MFM data acquired on a Cu/200 nm Ni/Cu/Si(001)–film at a tip–to–sample distance of 52 nm.  
b) Difference between the MFM measurement shown in panel a) and a second one, obtained under (nominally) identical conditions.

### 2.1.2 The Tip–Sample Interaction

For the description of the tip sample interaction, the cantilever is usually modeled as flexible beam, clamped at one end. The dimensions of the beam are the width,  $w$ , its thickness,  $d$  and its length,  $l$ . Such a beam has several oscillation modes, each with its own resonance frequency. However, it is usually sufficient to model the cantilever oscillations in the neighborhood of one resonance frequency. In the neighborhood of the first resonance, the cantilever behaves as a mass–spring oscillator. The spring constant,  $c_L$  of the spring can be calculated using [12]:

$$c_L = \frac{E w d^3}{4 l^3} \quad , \quad (2.1)$$

with  $E$  the Young modulus of the beam material (for Si,  $E = 1.25 \cdot 10^{11}$  [N/m<sup>2</sup>]). The free resonance frequency of the cantilever,  $f_0$  is computed using:

$$f_0 = \frac{1.873104^2 d}{4\sqrt{3}\pi l^2} \sqrt{\frac{E}{\rho}} \quad (2.2)$$

$$= \frac{1.873104^2}{4\sqrt{3}\pi} \sqrt{\frac{c_L}{m}} \quad (2.3)$$

with  $\rho$  the specific density of the beam material (for Si,  $\rho = 2.33 \cdot 10^3$  [kg/m<sup>3</sup>]), and  $m$  the mass of the beam ( $= w l d \rho$ ). Using these equations, one can determine the spring

constant of the cantilever from measurements of its free resonance frequency if the thickness of the cantilever is not known:

$$c_L = 59.305 \sqrt{\frac{\rho^3}{E}} f_0^3 l^3 w \quad . \quad (2.4)$$

The frequency response of the deflection  $d_n$  in the direction of the lever normal vector  $\mathbf{n}$  to the normal component of the force  $F_n$  as a function of frequency  $f$  is given by:

$$d_n(f) = \frac{1/c_L}{1 + if/(f_0 Q) - (f/f_0)^2} F_n(f) \quad , \quad (2.5)$$

with  $Q$  the quality-factor of the oscillator, which is determined by the damping of the cantilever. If a (constant) force derivative acts on the tip, the resonance frequency,  $f_{res}$ , is shifted in frequency:

$$\begin{aligned} \frac{f_{res}}{f_0} &= \sqrt{1 - \frac{1}{c_L} \frac{dF_n}{dn}} \\ &\approx 1 - \frac{1}{2c_L} \frac{dF_n}{dn} \end{aligned} \quad (2.6)$$

The error made by the approximation of the square root is usually negligible. In an MFM experiment, the change in resonance frequency is seldom more than 1% of the resonance frequency in which case the error in the derivative is  $1 \cdot 10^{-4}$  times the force constant. However, if the frequency shift is this large, it is likely that the force derivative varies over the oscillation amplitude. In this case, the relation between force derivative and frequency shift becomes much more complicated, as is the case in most true-atomic-resolution experiments [13].

The accuracy of the measured interaction is limited by the accuracy of the deflection detection and by the noise caused by thermal excitation of cantilever. Of these sources, the thermal noise presents the more fundamental limit to the sensitivity of the measurement. The spectral power density of the thermal noise in the displacement,  $S_{dd}(f)$ , can be found using equation 2.5 and the equipartition theorem [14]:

$$S_{dd}(f) = \frac{4\pi k_B T}{Q f_0 c_L} \frac{1}{(1 - (f/f_0)^2)^2 + (f/(f_0 Q))^2} \quad [\text{m}^2/\text{Hz}] \quad , \quad (2.7)$$

with  $k_B$  the Boltzmann constant, and  $T$  the absolute temperature. The relation between the displacement noise and the measurement noise is given in section 2.2.

## 2.2 Measurement Modes

There are several modes of operation of the instrument for detecting the tip-sample interaction. These measurement modes can roughly be divided into static and dynamic operating modes. In the static modes, the force acting on the tip is measured through the static deflection of the cantilever, in the dynamic modes, the force derivative acting on the tip is measured through the change in the dynamic behavior of the cantilever, as described by equation 2.5. Both modes can further be subdivided into the constant

interaction modes and the variable interaction modes. In the variable interaction modes, the interaction is simply measured as a function of position, whereas in the constant interaction modes, a feedback loop to the z-position of the tip keeps the interaction at a preset value. Initially, the constant interaction modes were also used in MFM measurements. However, these measurements are difficult to interpret, and therefore most MFM measurements made nowadays do not use z-feedback.<sup>2</sup>

### 2.2.1 Static Modes

In the static mode, the measured deflection of the cantilever is proportional to the force on the tip. In the used instrument, the deflection is measured using a fiber-optical interferometer [15]. The fiber-optic interferometer allows two methods for measuring the cantilever deflection. The first method is the direct measurement of interferometer signal. However, the relation between signal and deflection is non-linear because the signal varies sinusoidally with the cantilever-deflection. Moreover, the relation between the signal and the deflection becomes ambiguous for a deflection larger than one eighth of the wavelength of the interferometer light, due to the sinusoidal variation. The second method circumvents these problems by the use of a feedback loop. This feedback loop keeps the distance between the reference mirror and the cantilever constant. In the fiber-optic interferometer, the reference mirror is the fiber end, which can be moved by a piezo. Thus, the feedback signal to the fiber-piezo is proportional to the cantilever deflection. This method was used to perform the static measurements in this thesis.

The force sensitivity of the static mode,  $F_{min,static}$ , determined by the thermal vibrations of the cantilever can be calculated using equation 2.7. The low-frequency rms amplitude noise is found by inserting  $f = 0$ , multiplying the noise density with the measurement bandwidth,  $B$ , and taking the square root. The force noise is then equal to:

$$F_{min,static} = \sqrt{\frac{4k_B T c_L B}{2\pi Q f_0}} . \quad (2.8)$$

An example of a static measurement is shown in figure 2.3 c). It was made in air using the prototype instrument on the second MFM reference sample produced for the Concerted Action on Magnetic Storage Technology (CAMST) project [16] using a cantilever with a tip produced by electron beam induced deposition of carbon at the University of Twente (see section 2.3 for a full description of the cantilever ).

### 2.2.2 Dynamic Modes

In the dynamic modes, several methods are used to determine the force derivative from the dynamic behavior of the cantilever. The simplest method to implement is measurement of the change in the oscillation amplitude of the cantilever when it is excited by a sinusoidal signal with a constant amplitude and a frequency slightly below or above the free resonance frequency of the cantilever. However, this method is prone to measurement artifacts due to other causes for changes in the detected amplitude, such as

---

<sup>2</sup>The measurement modes are often incorrectly named by commercial manufacturers of scanning probe instruments. For example, they often use the term *contact mode* for the static modes, and *non-contact mode* or even *MFM mode* for the dynamic modes.

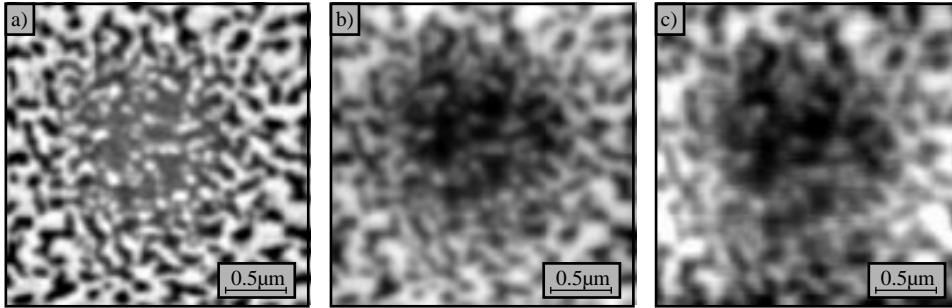


Figure 2.3: Imaging properties of the static and dynamic measurement modes.  
a) dynamic measurement in vacuum on the CAMST II sample.  
b) simulation of a static measurement using the measurement data shown in panel a).  
c) static measurement made in air on almost the same position as the measurement in panel a)

drift in the deflection detection system and changes in damping of the oscillation. Furthermore, the maximum measurement speed is inversely proportional to the Q-factor of the cantilever. Thus, it is not possible to perform high-sensitivity measurements at a reasonable speed. A faster and more robust method detects the phase shift between the excitation signal and the cantilever deflection, when the cantilever is excited at the free resonance frequency of the cantilever. This method has the disadvantage that the range in which the phase shift is proportional to the frequency shift becomes very small for cantilevers with a high Q-factor. These problems are circumvented in the third method, that uses FM-detection. This method employs a feedback of the cantilever deflection to the cantilever excitation to create an oscillator with a stable oscillation amplitude. If the phase shift of the feedback is approximately  $90^\circ$ , the oscillation frequency is equal to the resonance frequency of the cantilever. In addition to the resonance frequency, changes in the second dynamic property of the cantilever, the Q-factor, can also be detected in the FM-dynamic mode. This is realized by measuring the amplitude of the excitation signal that is needed to keep the oscillation amplitude at a preset value. This excitation amplitude signal can be used to detect non-reversible interactions between the tip and the sample.

Albrecht et al. found the minimal detectable force derivative in the FM-dynamic mode using equation 2.7 [17]:

$$\frac{dF_n}{dn}|_{min} = \frac{1}{A_{rms}} \cdot \sqrt{\frac{4k_B T c_L B}{2\pi Q f_0}}, \quad (2.9)$$

with  $A_{rms}$  the root-mean-squared vibration amplitude of the lever. An example of an FM-detection measurement is shown in figure 2.3a. It was made with the same tip on approximately the same position as the static measurement, but now in vacuum, with  $A_{rms} = 7$  nm and a measurement bandwidth of approximately 100 Hz.

From equation 2.9, one could conclude that the vibration amplitude should be made as large as possible, to obtain a small signal to noise ratio. However, this equation only holds as long as the force derivative acting on the tip is approximately constant. The



error made by this approximation will increase with increasing vibration amplitude, because the force derivative acting on the tip generally decreases with the tip–sample distance. If one wishes to apply the quantitative interpretation method of the MFM measurements presented in this thesis, the vibration amplitude must be chosen so, that the error caused by the constant derivative approximation is insignificant. If this is not the case, the quantitative interpretation of dynamic measurements becomes more difficult [13]. To demonstrate the effect of increasing the vibration amplitude, a series of measurements were made at a constant average distance to the sample with increasing vibration amplitude (figure 2.4). As the vibration amplitude increases from the 2 nm to 10 nm, the noise decreases, but the signal remains the same. For larger vibration amplitudes, the signal starts to increase, and the resolution of the image improves. For vibration amplitudes larger than 40 nm, topography artifacts occur in the image. Although the image resolution improves for larger vibration amplitudes, increasing the vibration amplitude is not a good approach if one wishes to obtain a better resolution. A more suitable method for obtaining a better resolution is to decrease the vibration amplitude and the tip–sample distance, until topography artifacts occur (figure 2.4e). Nevertheless, the signal-to-noise ratio of the large vibration amplitude remains higher for long wavelengths, which may be useful in some cases. A more quantitative evaluation of the advantages of large amplitude MFM measurements is given in [18].

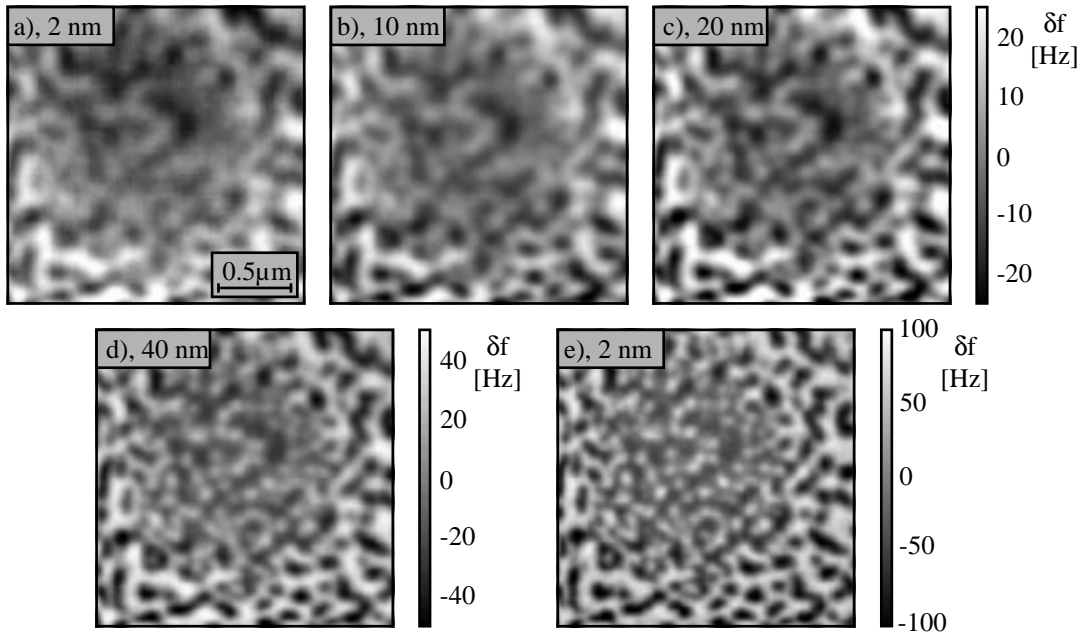


Figure 2.4: The effect of a increase of vibration amplitude on the image. As the amplitude is increased from 2 to 40 nm (panel a-d), the image contrast changes and the noise decreases. A better resolution can be obtained by decreasing the vibration amplitude to 2 nm and then decreasing the tip–sample distance (panel e). The measurements were made on the CAMST II sample using a cantilever with a Twente–type EBID tip.

### 2.2.3 Comparing the Static and Dynamic Modes

When comparing the images of measurements obtained in the static and the dynamic mode in figure 2.3, the first “advantage” of the dynamic mode becomes apparent: the images of the measurements obtained in the dynamic mode have a sharper contrast to the human eye, because the responsivity maximum lies at a higher frequency. To demonstrate that measurements made in the static mode and measurements made in the dynamic mode basically contain the same information, the relation derived in section 3.2.4 can be used. There it is shown that in magnetic force microscopy, the force can (approximately) be calculated from the force derivative in Fourier space. The Fourier components of the static image are calculated from those of the dynamic image by dividing them by  $2\pi/\lambda$ , with  $\lambda$  the wavelength of the field variation. This procedure was applied to create figure 2.3b.

Since both measurements contain the same information, the advantage of one mode, compared to the other must lie in the sensitivity of these modes. Using equations 2.8 and 2.9, one finds that the ultimate sensitivity of the dynamic mode is superior to the static mode for  $\lambda < 2\pi A_{rms}$  [16]. Thus, for an  $A_{rms}$  of 7 nm, the sensitivity of the static mode should be superior for stray field variations of a wavelength down to 40 nm. Of course, this comparison can not be made for the shown measurements, because the noise is a factor 3 to 5 lower for measurements made in vacuum due to an increase of the Q-factor. One might expect, that a static measurement made in vacuum would have a factor 3 to 5 lower noise than the shown static measurement. In practice however, the thermal noise limit is not reached in the static mode. One reason for this is that the noise of the detection system is large at low frequencies. This is due to laser noise with a  $1/f$ -like behavior of the power spectrum and to drift. Moreover, the noise in the detected deflection actually increases in vacuum. It is assumed that this additional noise is due a decreased damping of low-frequency mechanical vibrations of the instrument. Because this increase does not occur at high frequencies, the dynamic operation modes are the most suitable for MFM measurements in vacuum and for displacement sensors with high low-frequency noise.

## 2.3 Levers and Tips for Magnetic Force Microscopy

As in any type of scanning probe microscopy, the probe plays an essential role in the quality of the MFM measurements. In the MFM, this probe consists of a magnetic tip, mounted on a cantilever. In the following, the properties of the probes are discussed, separated in properties of the lever, non-magnetic properties of the tip and magnetic properties of the tip.

### 2.3.1 Cantilever Properties

The cantilever must have a high force sensitivity, well defined mechanical constants and an as small as possible coupling between vibrational and torsional oscillation modes. As was discussed in section 2.2, the measurement sensitivity is proportional to  $\sqrt{c_L/Qf_0}$ . Inserting equations 2.1 and 2.3, and assuming Q is independent of the cantilever geom-

etry, the sensitivity,  $S$  is given by:

$$S \propto \sqrt[4]{\frac{6.06675 \cdot 10^2 \rho E w^2 d^4}{l^2}} . \quad (2.10)$$

Thus, a long thin wire is ideal for obtaining a high sensitivity. However, wires have a strong coupling between vibrational and torsional vibration modes, low Q-factors, irreproducible mechanical characteristics, and are hard to use in a fiber-optic interferometer [19]. Therefore, it is more attractive to make the thickness of the cantilever as small as possible, and leave its width relatively large. To produce such cantilevers, one must resort to microfabrication techniques. The measurements presented in this thesis were made using commercial triangular SiN<sub>x</sub> cantilevers produced by Park Scientific Instruments (now Thermomicroscopes) [20] and Si Pointprobe cantilevers produced by Nanosensors [21]. The backsides of the SiN<sub>x</sub> cantilevers were coated with 20 nm of aluminum at the end of the cantilever, to obtain sufficient reflection for the interferometric displacement detection. In general, commercially available SiN<sub>x</sub> cantilevers have a better ratio of  $c_L/f_0$ , whereas the Si levers have a higher Q-factor. However, in the experiments described here, the high Q-factor of the Si cantilevers could not be exploited due to damping in the magnetic coating of the cantilever. This gives the SiN<sub>x</sub> cantilevers a slightly better sensitivity at room temperature (Table 2.1). However, this problem can be solved in future experiments by using masks during the evaporation of the different layers. More importantly, SiN<sub>x</sub> cantilevers are unsuitable for low-temperature experiments because their deflection was observed to be too sensitive to changes in temperature. This temperature sensitivity may be due to the strain in the cantilever caused by the different thermal expansion coefficients of the SiN<sub>x</sub> layer and the pyrex substrate. Another disadvantage of the SiN<sub>x</sub> cantilevers is their less well-defined spring constant, which is due to variations of the thickness of the cantilever. Moreover, the spring constant is more difficult to determine from measurements of the resonance frequency, because the SiN<sub>x</sub> cantilever have a triangular geometry, which can only approximately be described as two parallel beams.

### 2.3.2 Geometrical Tip Properties

The tip apex should be as small as possible, to make it less sensitive to forces of non-magnetic origin (eg. electrostatic forces, van-der-Waals forces). However, because magnetic tips can not be microfabricated at the moment, a non-magnetic microfabricated tip must be coated with a magnetic material. A further requirement of the tip is that it must be as long as possible and have a constant diameter. Thus, the requirements for MFM tips are actually much the same as for tips used in true-atomic-resolution experiments, where one would like to have a single atom at the end of the tip, and as little material as possible to support it [13]. In general, the microfabricated Si-tips approach this ideal much better than the SiN<sub>x</sub> tips. To improve the SiN<sub>x</sub> tips, a super-tip is grown on top of the microfabricated tip by electron beam induced deposition (EBID) of carbon or hydrocarbons [22, 23]. The two types of tips are shown in figure 2.5.

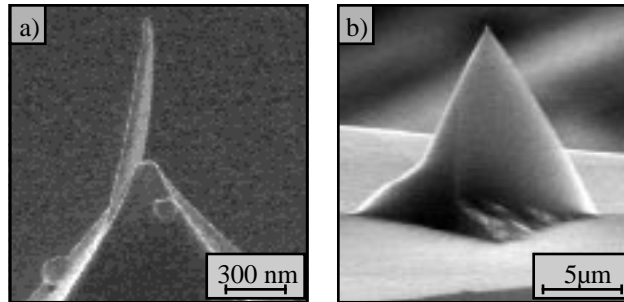


Figure 2.5: a) An electron beam induced deposition (EBID) tip, grown on top of a pyramid tip on a  $\text{SiN}_x$  cantilever, coated from the side with 10.7 nm Fe and 15 nm Au. b) Microfabricated Si tip, coated from the side with 7.3 nm Fe and 12 nm Au.

### 2.3.3 Magnetic Tip Properties

As will be explained in more detail in chapter 3, the magnetization of the ideal MFM tip is fixed, and the magnetic flux emanating from the tip should be small enough to prevent modification of the sample. On the other hand, the flux density should be large in a small area close to the end of the tip, to obtain high resolution and sensitivity. The maximum obtainable flux density is limited by the magnetic material of the coating, therefore a compromise must be found to obtain a high flux density in a relatively small area, and a low large area flux. The optimum balance between flux density and total flux must be determined for each sample. Three parameters can be varied in this optimization: the shape of the non-magnetic tip, the material of the magnetic coating and its thickness. The optimum shape for the non-magnetic tip is clearly has a small size in the  $x$ - and  $y$ -direction. Furthermore, the tip radius should not vary with  $z$ , because this will give rise to “useless” flux (flux that is spread over a large area) [19, 24]. Such tips have the additional advantage that it is hard to modify their magnetization state due to a combination of their magnetic shape anisotropy (see section 4.1.1) and the apparent difficulty to nucleate a domain wall in the tip. It is to be expected that the EBID-tips better approximate this ideal than the microfabricated Si tips, which will be demonstrated in section 3.4. To limit the amount of “useless” flux, only one side of the tip is coated with magnetic material by oblique evaporation in a high vacuum environment (base pressure in the  $10^{-7}$  mBar range). Furthermore, iron was used as magnetic material, to obtain a high magnetic moment per volume. A disadvantage of using iron is that it must be protected against oxidation by a protective coating if the tip is not prepared and used in a UHV environment. This increases the size of the tip and the distance between the magnetic part of the tip and the sample is increased by a few nanometers.<sup>3</sup> The use of cobalt as the magnetic coating material might circumvent these slight problems. Another problem of the use of iron is that the optimal coating thickness for some samples is so thin ( $< 4$  nm), that it becomes difficult to fabricate reproducible magnetic layers in high-vacuum. In such a case, the use of nickel for the magnetic layer may be a solution, because nickel has an approximately 3.5 times lower saturation magnetization than iron, and therefore the magnetically equivalent nickel

<sup>3</sup>As will be shown in section 3.2, this will reduce the image resolution, as it decreases with distance.

layer is 3.5 times thicker than the magnetically equivalent iron layer.

The properties of the probes used in this thesis are summarized in table 2.1. The first experiments with EBID tips were made with tips produced at the University of Twente by Leon Abelmann. Later, it was possible to produce EBID tips in Basel with the help of Daniel Mathys of professor Guggenheim's group. All tips were coated at an angle of 30 degrees to the cantilever normal,  $\mathbf{n}$ , using thermal evaporation. Coating thicknesses were measured in the evaporation direction. The actual thickness of the coating on the tip is approximately as little as half the measured thickness, due to the canted orientation of the cantilever, and the canted orientation of the tip surfaces. For the iron coated tips, a gold layer was evaporated over the iron, to prevent its oxidation. The force derivative sensitivity in the dynamic mode,  $dF_{n,min}/dn$ , was estimated by measuring an "empty" image, as was suggested in [25]. For all MFM data presented in this thesis, the measurement bandwidth was 100 Hz and the rms oscillation amplitude of the cantilever was 7 nm, unless explicitly stated otherwise.

cantilever type	magnetic coating material	magnetic coating [nm]	Au coating [nm]	$c_L$ [N/m]	$f_0$ [kHz]	$dF_{n,min}/dn$ [ $\mu\text{N}/\text{m}$ ]
Twente EBID	Co	20.0	-	0.03	16.3	1.5
Basel EBID	Fe	10.7	15	0.03	16.5	1.5
Si	Fe	7.3	12	0.2	12.3	3.0

Table 2.1: Properties of the cantilevers used in this thesis



## Chapter 3

# Contrast Formation in Magnetic Force Microscopy

The possible contrast mechanisms in magnetic force microscopy are generally well understood qualitatively (see section 3.1). However, the magnitude of the contrast is seldom evaluated in the literature, and when it is evaluated, there is rarely a good agreement between theoretical predictions of the magnitude of the contrast and the contrast in the measurements. However, quantitative predictions of the magnitude of the contrast are desirable for several purposes:

- to predict whether certain experiments can be performed
- to be able to interpret the image, if several contrast mechanisms occur simultaneously
- to analyze the micromagnetic magnetization state of the sample, in addition to its domain structure

Most of the present proposed procedures for the computation of the contrast are rather complex and/or time consuming [26, 27]. To save calculation time, the evaluation of the contrast is often limited to a “typical” scan-line of the measured image. In this case, the domain structure should neither change too much in the direction perpendicular to the direction of the scan-line, nor should it change too much close to the end of the scan line. This approximation is not always applicable, because domain boundaries often twist and turn (as is the case for most measurements presented in this thesis), and because the magnetic interactions have a long range, and deviations at a considerable distance from the scan-line may influence the signal. Therefore, if one is interested in evaluating more complicated domain structures, a fast method is needed that can calculate the contrast of the whole measurement.

A simple method for the quantitative evaluation of whole MFM images was proposed by Mansuripur and Giles [28], and demonstrated by Schönenberger and Alvarado [29]. It was shown that in many cases, the image contrast can be elegantly computed in Fourier space. The methods described in section 3.2 expand the applicability of this method. One of the main improvements is a more practical, and probably more accurate, procedure for the calibration of the measured signal and the stray field of the tip.

This procedure is presented section 3.3. To demonstrate the necessity of using such a calibration procedure, the contrast of the calibrated tips is compared to some simple models of the contrast mechanism in section 3.4. Finally, the calibration of the MFM is used to compare the stray-field sensitivity of the MFM to that of other scanning stray-field measurement methods in section 3.5.

### 3.1 Contrast mechanisms

The image contrast is determined by the change in the force or force derivative exerted on the tip, when it is scanned over the sample. The magnitude of the measured interaction depends on the distributions of the sample stray field and the tip magnetization distribution. When the magnetization distribution of the tip, and the stray field of the sample are modified by one another, the measured interaction may depend on the tip-sample position and on the history of the tip-sample position. Depending on the extent of modification of the tip magnetization and the sample stray field, the contrast formation processes in magnetic force microscopy can be divided in three categories [9]:

**Negligible modification** As long as the magnetization of the tip, and the distribution of the stray field of the sample do not change with the tip-sample position, the measured contrast can be described as a linear operation on the stray field of the sample.

**Reversible modification** The distribution of the stray field of the sample or the magnetization of the tip can change with the tip-sample position. As long as all changes in the system are reversible, the measured contrast is a function of the tip-sample position only.

**Hysteretic, or Irreversible modification** The distribution of the stray field of the sample, or the magnetization of the tip are changed irreversibly during the scan. The observed contrast does not only depend on the actual tip-sample position, but on the history of the tip-sample position.

To simplify the prediction of the contrast, the discussion of the contrast mechanisms is limited to those cases in which there is negligible modification of the tip. One reason for doing this, is that this approach appears to be a valid approximation for explaining the measurements presented in this thesis, as is demonstrated in paragraph 3.2.5. Furthermore, the practical use of the mechanisms that allow modification of the tip is very limited, although it can not always be avoided. It has been argued that an ideally soft magnetic tip, i.e. a tip with a magnetization proportional to the stray field, would be more suitable for imaging soft magnetic samples, because it would modify the sample magnetization to a lesser extent. However, such a tip is difficult to produce in practice, due to the inherent shape anisotropy of the tip, which causes it to have a preferential magnetization direction. The contrast due to reversible changes in the tip magnetization is then due to a small deviation from the preferential direction, which is added to the contrast due to the average tip magnetization. Understandably, this makes quantitative analysis of the contrast more complicated. Another possibility to obtain a tip magnetization that is proportional to the stray field of the sample, is the



use of superparamagnetic tips. Such a tip is so small, that thermal excitations of the tip magnetization are strong enough to reverse the tip magnetization, and the time average of its magnetization is proportional to the applied field. However, such tips have not been demonstrated in practice. Finally, the case of hysteretic tip modifications is quite useless for magnetic force microscopy.

If one now considers the modification of the sample stray field, each of the modification cases can be applied to obtain information on different properties of the sample. In the following, some of the properties that can be obtained are discussed for several sample types.

### 3.1.1 Negligible Sample Modification

To determine whether the sample modification is negligible, one can use the test given in section 3.2.5. When imaging ferromagnetic samples, the modification of the sample is generally negligible for samples with a sufficiently large coercive field. How high this coercive field must be is unclear, because it is a measure for how sensitive the sample is to a homogeneous field, whereas the field of the tip is very inhomogeneous. It is reasonable to expect that the modification of the sample is still small when the maximum tip field is of comparable size to the coercive field of the sample. As will be shown in chapter 4.2.1, the field measurements can, using certain assumptions, be used to reconstruct the magnetization of the sample. In addition to determining the domain pattern, the reconstruction can be applied to determine the magnetization structure within the domains, or inside the domain walls.

When imaging type-II superconductors, the imaging of the field of strongly pinned vortices is an example of the negligible modification case, as long as the vortices are not moved too much. It should be possible to determine the local penetration depth and perhaps the correlation length of the superconductor from the magnetic field measurements. An evaluation of the vortex contrast in (type-II) high- $T_c$  superconductors is presented in section 5.1.2.

The imaging of current patterns in “normal” conductors may also be modification free, as long as the Hall effect caused by the tip is small. This is the case in conductors with a small width, or in Hall sensors in the presence of a relatively large external field. The Fourier-space computation of the contrast of a current pattern limited to the sample plane was described for the purpose of analyzing scanning SQUID<sup>1</sup> measurements [30] of infinitely thin samples. The description was later extended to thick films for the evaluation of magneto-optical measurements on superconductors [31, 32]

### 3.1.2 Reversible Sample Modification

When imaging magnetic samples, the modification of the sample produces an additional signal that depends on the magnetic anisotropy and exchange strength of the sample. For small changes of the sample magnetization, the contrast can be calculated using the model of Abraham and McDonald[33], which is a variant of the well known  $\mu^*$  method [34]. However, if the perturbation of the magnetization becomes large, or the magnetic exchange energy of the sample can not be neglected, the response of the

---

<sup>1</sup>Superconducting QUantum-Interference Device

sample becomes non-linear. Then this model can not be used anymore, and evaluation of the image contrast must be performed using much more complicated micromagnetic calculations.

When imaging superconductors, the Meissner repulsion in the London limit is a linear, reversible interaction. Thus, the MFM signal over a superconductor may vary as the Meissner repulsion varies. The penetration depth of the superconductor can be determined from the distance dependence of the Meissner force. This was demonstrated for the simple case where the Meissner force does not depend on the lateral position of the tip as described in [35] and section 5.1.1.

### 3.1.3 Irreversible Sample Modification

The subject of irreversible modification using MFMs is largely unexplored. On magnetic samples, nucleation of magnetic domains has been reported [36], but no evaluation of the involved forces was made. A change in the damping of the tip vibration close to domain boundaries was reported by Grütter et al. [37], but the explanation of the contrast [38] is doubtful because the measurements were made in the constant force gradient mode. In this mode, the distance between the tip and sample is varied during the measurement to keep the magnetic signal constant. Because this distance change typically occurs near the domain boundaries, the change in damping may well be due to the distance change. In superconductors, the nucleation of vortex bundles was demonstrated [39, 40], but the interaction forces involved were not measured. In principle, it should also be possible to study the nucleation of superconducting domains in the neighborhood of the critical field.

## 3.2 Calculation of the Contrast for the Negligible Modification Case

In this section the calculation of the measured contrast from the magnetic stray field of the sample is discussed. The computation of the stray field for various sample types is left to chapters 4 and 5. As long as the magnetization of the tip is not modified by the stray field of the sample, the magnetic force on the tip,  $\mathbf{F}$ , can in principle be calculated in direct space using:

$$\begin{aligned} \mathbf{F}(t) &= \mu_0 \int_{-\infty}^{\infty} \mathbf{H}_{sample}(x', y', z', t) \\ &\times \nabla' \cdot -\mathbf{M}_{tip}(x' - x(t), y' - y(t), z' - z(t)) dx' dy' dz' \end{aligned} \quad (3.1)$$

Here, the vector  $(x, y, z)$  represents the position of the tip relative to the sample,  $\nabla \equiv (\partial/\partial x, \partial/\partial y, \partial/\partial z)$  is the nabla operator,  $\mathbf{M}_{tip}(x', y', z')$  is a function that describes the magnetization of the tip, with the origin of the  $(x', y', z')$  coordinates at the tip apex, and  $\mathbf{H}_{sample}$  the magnetic stray field of the sample, with its origin at the sample surface. In the case of reversible modification, the  $t$ -dependence of the field of the sample can be replaced by a dependence on the position of the tip,  $(x, y, z)$ . In the case of negligible modification of the sample, the dependence of the sample stray field on the coordinate

of the tip can be left out as well, and the force is given by a 3-dimensional correlation integral:

$$\begin{aligned} \mathbf{F}(x, y, z) &= \mu_0 \int_{-\infty}^{\infty} \mathbf{H}_{sample}(x', y', z') \\ &\times \nabla' \cdot -\mathbf{M}_{tip}(x' - x, y' - y, z' - z) dx' dy' dz' \end{aligned} \quad (3.2)$$

In the remainder of this section, only this type of contrast formation is discussed. It will be shown, that in this case, 2-Dimensional Fourier analysis is an efficient tool for the calculation of the tip-sample interaction.

### 3.2.1 Magnetostatic Fields in Fourier Space

Before deriving the force experienced by the tip in Fourier space, it is useful to discuss the Fourier transform itself, and derive some properties of magnetostatic fields in Fourier space. First, the definition of the Fourier transform used in this thesis must be given, as many, slightly different definitions of the Fourier transform exist (see [41, 42]). Here, the Fourier transform pair is defined as:

$$G(\mathbf{k}) = \int_{-\infty}^{\infty} g(\mathbf{r}) e^{-i\mathbf{k}\cdot\mathbf{r}} dx dy \quad (3.3)$$

$$g(\mathbf{r}) = \frac{1}{4\pi^2} \int_{-\infty}^{\infty} G(\mathbf{k}) e^{i\mathbf{k}\cdot\mathbf{r}} dk_x dk_y, \quad (3.4)$$

with  $\mathbf{r} = (x, y)$  and  $\mathbf{k} = (k_x, k_y)$ . The function  $G$  in Fourier space has the units of the spectral density of  $g$ . In accordance to general practice, the same name and symbol will be used for quantities in direct space and in Fourier space in spite of the different units. To distinguish between the two, the coordinates  $(x, y)$  are used for dimensions in direct space, whereas  $(k_x, k_y)$  are used for dimensions in fourier space.

In practice, the continuous Fourier transforms can only be approximated, because the integral of the Fourier transform is taken over infinite, continuous space, whereas the measurements, are made at a discrete number of points,  $N_x \times N_y$  in a finite space with an area  $l_x \times l_y$ . For the actual calculations, one must approximate the continuous transform by the discrete transform pair:

$$G(m, n) = l_x l_y \frac{1}{N_x N_y} \sum_{o,p} g(o, p) \exp\left(-\frac{2\pi i(mo + np)}{N_x N_y}\right) \quad (3.5)$$

$$g(o, p) = \frac{1}{l_x l_y} \sum_{m,n} G(m, n) \exp\left(-\frac{2\pi i(mo + np)}{N_x N_y}\right) \quad (3.6)$$

Details on the implementation of the discrete Fourier transform can be found in [42, 43].

It is useful for the calculation of the force on the tip to derive some properties of the magnetic field of the sample in Fourier space:

- The area above the sample is current free and does not contain time-varying electrical fields, therefore the rotation of the stray field is zero ( $\nabla \times \mathbf{H} = \mathbf{0}$ ). The stray field can then be expressed as the gradient of a magnetic scalar potential,  $\phi_M$ :  $\mathbf{H} = -\nabla\phi_M$ . To calculate the magnetic scalar potential, it is useful to define magnetic charges, in correspondence to electrostatics. The magnetic volume charge density,  $\rho_M$  and the magnetic surface charge density,  $\sigma_M$ , are defined as:

$$\rho_M \equiv -\nabla\mathbf{M} \quad (3.7)$$

$$\sigma_M \equiv (\mathbf{M}_i - \mathbf{M}_o) \cdot \mathbf{n} \quad (3.8)$$

The magnetic scalar potential can then be calculated using the the Laplacian of the scalar potential, given by  $\nabla^2\phi_M = -\rho_M$ , and  $\frac{\partial\phi_{M,i}}{\partial n} - \frac{\partial\phi_{M,o}}{\partial n} = \sigma_M$ .

- There is no magnetization outside the sample, therefore the Laplacian of the scalar potential is equal to zero.
- The nabla operator is described in 2D-Fourier space as:  $\nabla = (ik_x, ik_y, \partial/\partial z)$ .

Combining the last two properties, one easily derives that a sinusoidal potential decays exponentially with the product of the magnitude of the k-vector,  $k = \sqrt{k_x^2 + k_y^2}$ , and the distance from the sample:

$$\phi_M(\mathbf{k}, z) = \phi_M(\mathbf{k}, 0)e^{-kz} \quad (3.9)$$

From the relation between scalar potential and stray field, it is clear that all stray field components will also decay exponentially. The last, and most important property can easily be derived from the previous relation: if the nabla operator is applied to source free fields, it can also be written as  $\nabla = (ik_x, ik_y, -k)$ . Therefore, the magnetic scalar potential, and thereby all stray-field components in the x-y-plane, can be determined from a measurement of the stray field in the z-direction,  $H_z$ , except for their average value,  $H(k_x = 0, k_y = 0)$ , using the relations:

$$\phi_M(\mathbf{k}, z) = -\frac{1}{k} H_z(\mathbf{k}, z) \quad (3.10)$$

$$\mathbf{H}(\mathbf{k}, z) = -\frac{\nabla}{k} H_z(\mathbf{k}, z) \quad (3.11)$$

The same reconstruction can not be performed using only the x- or y-component of the stray field, therefore, measuring these components independently, as proposed in [44], makes little sense.

### 3.2.2 Computation of the Force on the Tip

If one now calculates the force in Fourier space, the x-y-part of the correlation integral in equation 3.2 is replaced by a multiplication:<sup>2</sup>

$$\mathbf{F}(\mathbf{k}, z) = \mu_0 \int_{-\infty}^{\infty} \mathbf{H}_{sample}(\mathbf{k}, z') \nabla' \cdot -\mathbf{M}_{tip}^*(\mathbf{k}, z' - z) dz'$$

---

<sup>2</sup>one should not make the mistake to use the relation  $\nabla = (ik_x, ik_y, -k)$ , because this relation is only valid for the stray field outside the sample.

$$= \mu_0 \int_{-\infty}^{\infty} \mathbf{H}_{sample}(\mathbf{k}, z' + z) \nabla' \cdot -\mathbf{M}_{tip}^*(\mathbf{k}, z') dz' ,$$

with \* denoting the complex conjugate. Using equation 3.9, one gets:

$$\mathbf{F}(\mathbf{k}, z) = \mu_0 \mathbf{H}_{sample}(\mathbf{k}, z) \int_{-\infty}^{\infty} e^{-kz'} \nabla' \cdot -\mathbf{M}_{tip}^*(\mathbf{k}, z') dz' \quad (3.12)$$

$$\equiv \mu_0 \mathbf{H}_{sample}(\mathbf{k}, z) \sigma_{tip}^*(\mathbf{k}) , \quad (3.13)$$

with  $\sigma_{tip}(\mathbf{k})$  the Fourier transform of a tip-equivalent surface charge pattern, with the surface charges located in a plane at the apex of the MFM tip, parallel to the sample. The stray field of the tip below the plane containing equivalent charge distribution can be calculated from  $\sigma_{tip}(\mathbf{k})$  using the expression:

$$\mathbf{H}_{tip} = \frac{1}{2} \begin{pmatrix} -ik_x/k \\ -ik_y/k \\ 1 \end{pmatrix} \exp(k(z' - z)) \sigma_{tip}(\mathbf{k}) , \quad (3.14)$$

with  $z$  the distance of the tip to the sample, and  $z' < z$  the distance of the field to the sample. Clearly, if one wishes to calculate the force on the tip from the field of the sample, one needs to know the behavior of  $\sigma_{tip}$ . A procedure for determining  $\sigma_{tip}$  is given in section 3.3.

### 3.2.3 The Relation between the Force and the Measured Contrast

The measured quantity in the MFM experiment must be derived from the force-vector. This quantity is either the force  $F_n(\mathbf{k})$ , or its derivative  $\frac{d}{dn} F_n(\mathbf{k})$ , in the direction of the normal of the cantilever surface (see section 2.2). This direction is characterized by the vector  $\mathbf{n} = (0, \sin(\theta), \cos(\theta))$ , with  $\theta$  the canting angle between the normal of the cantilever and the normal of the sample surface (figure 2.1):

$$\frac{d}{dn} F_n = \mathbf{n} \cdot \nabla F_n = \mathbf{n} \cdot \nabla(\mathbf{n} \cdot \mathbf{F}) . \quad (3.15)$$

Inserting equations 3.13 and 3.11 into equation 3.15, one finds:

$$\begin{aligned} F_n(\mathbf{k}) &= -\mathbf{n} \cdot \left( \mu_0 \sigma_{tip}^*(\mathbf{k}) \frac{\nabla}{k} H_z(\mathbf{k}) \right) \\ &\equiv \mu_0 \sigma_{tip}^*(\mathbf{k}) LCF(\mathbf{k}, \theta) H_z(\mathbf{k}) , \end{aligned} \quad (3.16)$$

and

$$\begin{aligned} \frac{d}{dn} F_n(\mathbf{k}) &= (\mathbf{n} \cdot \nabla) F_n(\mathbf{k}) \\ &= -k \mu_0 \sigma_{tip}^*(\mathbf{k}) [LCF(\mathbf{k}, \theta)]^2 H_z(\mathbf{k}) , \end{aligned} \quad (3.17)$$

with  $LCF(\mathbf{k}, \theta)$  the lever canting function that describes the effect of the canting angle of the cantilever on the measurement. The main effect of the canted orientation of

the cantilever is a direction dependent phase shift in the  $k_y$ -direction, if the image is interpreted to represent the  $H_z$  field. A canting angle  $\theta$  results in a phase-shift  $\theta$  in the static modes, and  $2\theta$  in the dynamic modes. This  $k_y$ -independent phase-shift causes a slight distortion of the image in the  $y$ -direction. In the images made with the instruments used in this thesis, this is visible as a distortion in the up-down direction, whereas in images made with a Nanoscope III, this is visible as a distortion in the left-right direction. The distortion can easily be corrected by dividing the measurement by the LCF, or the squared LCF in Fourier space, depending on what measurement mode was used. In figure 3.1, this is shown for a measurement on a Cu/7 nm Ni/Cu sandwich. Although the difference is not immediately obvious in the image (panels a,b), it becomes clear when taking a line-section in the  $y$ -direction (panel c). In the measured image (dotted line), there is a clear asymmetry in the  $y$ -direction, which is much reduced after correcting for cantilever canting (solid line).

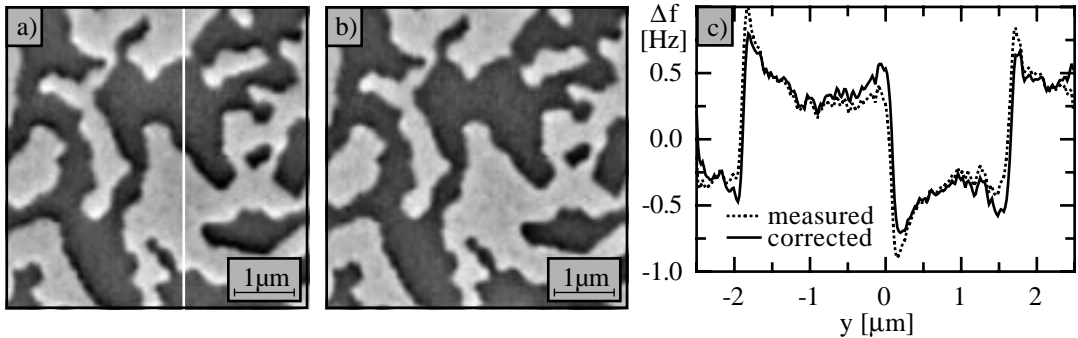


Figure 3.1: The canted orientation of the cantilever causes a distortion in the domain transitions, that can be easily removed in Fourier space.

a) measurement with a Si-tip on a Cu/70 nm Ni/Cu/Si(001)-film at a tip-to-sample distance  $z_1 = 53$  nm.

b) image corrected for cantilever canting using the LCF.

c) Line-sections of the measured and the corrected image, on the position indicated by the white line in panel a. The asymmetry in the domain transition is strongly reduced. Wavelengths below 80 nm were filtered out in the line-sections to remove noise.

### 3.2.4 The Instrument Calibration Function

It is useful to define an *Instrument Calibration Function*  $ICF(\mathbf{k})$  in addition to  $\sigma_{tip}(\mathbf{k})$  to describe the imaging properties of the instrument. The ICF gives the relation between sample stray field (derivative) and measured quantity, and can directly be determined from calibration measurements (see section 3.3). On the other hand,  $\sigma_{tip}(\mathbf{k})$  can only be determined from the calibration measurements if one knows the canting angle and the mechanical properties of the cantilever. Therefore, the use of the ICF to describe the instrument is especially advantageous if one wishes to use cantilevers with poorly defined spring constants, such as SiN<sub>x</sub> cantilevers (see section 2.3).

Several calibration functions can be defined, at least one for each measurement mode. To avoid confusion between the different calibration functions, one should always

explicitly state for what pair of variables the instrument calibration was determined. As an example, the relation between instrument calibration and tip calibration is given for the instrument calibration functions:  $ICF_{H_z}^z$  from stray field to cantilever deflection,  $ICF_{dH_z}^{\Delta f}$  from stray field *derivative* to resonance frequency shift,  $ICF_{H_z}^{\Delta f}$  from stray field to resonance frequency shift and  $ICF_{H_z}^{\Delta \phi}$  from stray field to phase shift. Using equations 2.5, 2.6, 3.16 and 3.17, one finds:

$$ICF_{H_z}^z(\mathbf{k}) = \frac{1}{c_L} \mu_0 \sigma_{tip}^*(\mathbf{k}) LCF(\mathbf{k}, \theta) \quad (3.18)$$

$$ICF_{dH_z}^{\Delta f}(\mathbf{k}) = -\frac{f_0}{2c_L} \mu_0 \sigma_{tip}^*(\mathbf{k}) [LCF(\mathbf{k}, \theta)]^2 \quad (3.19)$$

$$ICF_{H_z}^{\Delta f}(\mathbf{k}) = \frac{f_0}{2c_L} k \mu_0 \sigma_{tip}^*(\mathbf{k}) [LCF(\mathbf{k}, \theta)]^2 \quad (3.20)$$

$$ICF_{H_z}^{\Delta \phi}(\mathbf{k}) = \frac{Q}{c_L} k \mu_0 \sigma_{tip}^*(\mathbf{k}) [LCF(\mathbf{k}, \theta)]^2 \quad , \quad (3.21)$$

where  $f_0$  is the resonance frequency,  $c_L$  the force constant and  $Q$  the quality-factor of the free cantilever (see sec. 2.1). By combining equations 3.18 and 3.20, it becomes clear that a static image can be computed from a dynamic image in Fourier space by dividing the dynamic measurement by  $1/2 f_0 k LCF(\mathbf{k}, \theta)$ , as was demonstrated in figure 2.3.

### 3.2.5 Testing for Negligible Modification

In the following, three methods are discussed for testing whether the modification of the tip and sample during the imaging is negligible.

The simplest, and most imprecise way to check whether the tip modifies the sample, is to invert the contrast of the image, and to see whether the image “looks the same”.

A more complicated, but also more exact method is to reverse the magnetization of the tip between two measurements on the same sample position [45]. In this case, the sum of the two measurements should be zero in the non-modification case (assuming the magnetization of the tip has exactly been reversed).

The third method is useful if one does not wish to remove the tip from the instrument, or one can not measure one the same location after removing the tip. In this case, one can also test whether equation 3.9 holds for measurements made at the same lateral position, but at different distances: The sample field decays exponentially, therefore the measured signal must also decay exponentially when the tip and sample do not modify one another.

Of the ferromagnetic samples used in this thesis, the Cu/Ni/Cu sample containing 200 nm of Ni is most suitable for this test, because vibrating sample magnetometry measurements have shown that its magnetization state is the most sensitive to applied magnetic fields (see section 4.1). Thus, if this sample is not modified by the tip field, the other samples are unlikely to be modified. The test measurements were made on the same location as in section 2.1, with tip-to-sample distances of 52 and 74 nm (figure 3.2a,b). The effect of a distance increase of 22 nm was calculated from the measurement data shown in panel a, using equation 3.9. The difference between the measurement and the simulation is shown in panel c. After subtracting the errors due to noise and position accuracy, the root-mean-squared (rms) error is 0.07 Hz. There seems to be no

systematic error in the image, except for the area marked by the circle. Here, a slight change in the sample magnetization is detected. Note though, that topography artifacts will also give rise to a difference, as well as errors related to Fourier-transforming an image of finite size. Nevertheless, equation 3.9 clearly holds for almost the whole MFM measurements acquired at two different tip-to-sample distances. This strongly indicates, but does not prove that the influence of the MFM tip on the sample (and vice versa) can be neglected in this case. For other samples and tips, this may not be the case: From MFM data acquired on Au/Co/Au thin films, Belliard et al.[46] have concluded that equation 3.9 did not explain the observed distance dependence of the contrast.

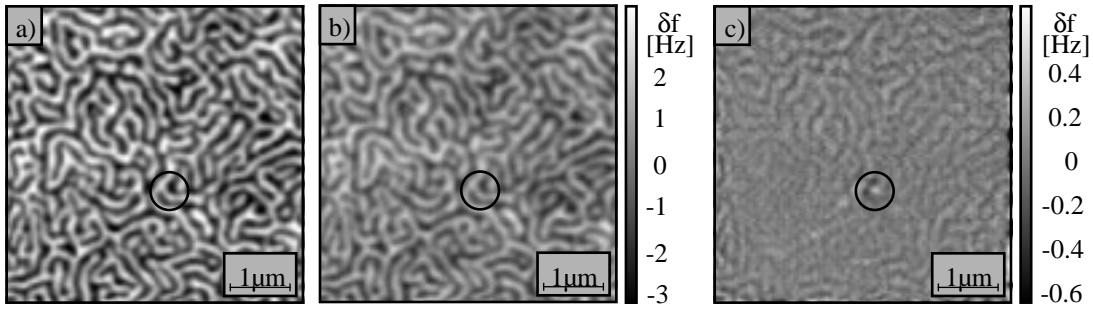


Figure 3.2: Test measurements of the exponential decay of the spectral components of the image with distance.

- a) MFM data acquired on a Cu/200 nm Ni/Cu/Si(001)-film at a tip-to-sample distance of 52 nm.
- b) MFM data acquired at a tip-to-sample distance of 74 nm.
- c) Difference image of a simulated measurement and the measurement shown in panel b. The simulated measurement was computed from the data shown in panel a) using equation 3.9.

### 3.2.6 Calculation of the Field from the Measured Signal

Until now, only the relations were given for simulating a measurement using a given stray field distribution. Of course, it is more interesting to compute the stray field for a given MFM measurement. This can generally be done by inverting the given relations. However, the accuracy of the results obtained using these inverse relations is limited by three factors. First, the MFM can not sense homogeneous magnetic fields ( $\sigma_{tip}(\mathbf{k} = \mathbf{0}) \equiv 0$ ). Second, for the derived equations to be valid, the measurement must have an infinite extent. The third limit is mainly an instrumental problem; the combination of limited signal-to-noise ratio of the measurement and the finite volume of the tip leads to an information loss, especially at high spatial frequencies. However, this loss can be minimized by an improvement of the instrumentation, i.e. measurement at low temperatures [11] and the use of tips with a better resolution [18].



### 3.3 Calibration of the Instrument

From the previous section, it is clear that if one wishes to quantitatively evaluate MFM measurements, one must calibrate the MFM. Several authors performed a calibration over the whole  $k$ -space, instead of using a tip model such as the one given in equation 3.24:

Schönenberger et al. [29] first used transfer functions to analyze the imaging properties of various ferromagnetic tips. For the calibration process, they used several magnetic hard-disc samples containing bits of different periods, and assumed that only the fundamental frequency of the tracks was imaged.

Madabhushi et al. [47] described the imaging process from magnetization to force gradient by two dipole response functions,  $D_x(x, y)$  and  $D_y(x, y)$ . These functions are defined as the MFM image of a magnetic point dipole along the  $x$  and  $y$  direction, respectively. In the experiment, an MFM measurement of a magnetic nanoparticle was used as an approximation for both dipolar transfer functions. The obtained response functions were used to deconvolve a measurement of a hard disc track to obtain the rotation free part of its in-plane magnetization structure.

Chang et al. [48] and Zhu et al.[49] used an impulse response function, which is defined as the MFM response to a magnetic point charge at the sample surface. They used a nanostructured film and partially erased bit transition in an in plane hard disc track respectively, as an approximation for this point charge. The measured response of the MFM tip to this point-like field source was used to reconstruct a magnetic surface charge pattern of a recorded track in a hard-disc.

In contrast to the definition of the tip calibration function, the dipolar transfer functions defined by Madabhushi et al.[47] and the impulse response function defined by Chang et al. [48] contain both the stray field imaging properties of the MFM tip and the geometrical and magnetic properties of the sample that generates the stray field. As an example the Fourier transform of the dipole transfer functions,  $D_{x,y}(\mathbf{k})$ , as defined by Madabhushi et al., relate to  $\sigma_{tip}(\mathbf{k})$  as

$$D_{x,y}(\mathbf{k}) = ik_{x,y} \frac{c_L (1 - e^{-k d_0}) e^{-k z_0}}{f_0} \times [LCF(\mathbf{k}, \theta)]^2 \mu_0 \sigma_{tip}^*(\mathbf{k}) \quad . \quad (3.22)$$

The dependence of these transfer functions on various experimental parameters, such as tip-to-sample distance,  $z_0$ , the thickness of the calibration sample,  $d_0$ , the strength of the dipole/monopole and the measurement mode, makes these functions unsuitable for comparing tips calibrated under different circumstances. Moreover they can not (directly) be used to compare measurements made with one tip at different distances.

Besides the fact that the transfer functions are difficult to use, the procedure to determine them from measuring an isolated magnetic monopole or ideal dipole is problematic, since these are difficult to realize in an experimental situation. In addition, the signal-to-noise ratio of an MFM measurement of such a calibration structure decreases with its magnetic volume, i.e. the idealness of the mono-/dipole. Finally, it is difficult to estimate the magnitude of the mono-/dipole, making an absolute calibration more complicated.

### 3.3.1 Calibration Procedure

To circumvent the problems of the existing calibration procedures, a procedure was developed that allows the calibration of the instrument using easily obtainable samples. This procedure consists of several steps, which are shown schematically in figure 3.3. As an example, the intermediate results of the consecutive steps are shown for one measurement in figure 3.4. The measurement in panel a was made using a microfabricated Si cantilever, coated with 7.3 nm of Fe on a Cu/Ni/Cu sample containing 10 nm of Ni, at a measurement distance of 45 nm. For more information on the sample, see chapter 4.

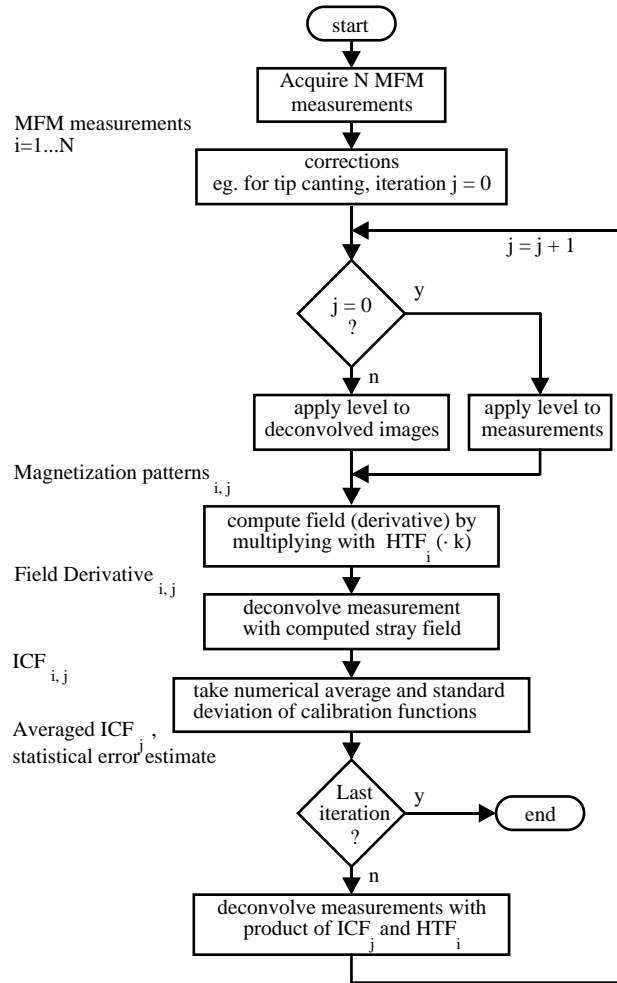


Figure 3.3: Flow chart of the calibration process.

The calibration procedure starts with making several measurements of different magnetization patterns. This can be achieved by changing the measurement position on one sample and/or by measuring on different samples.

Next, the magnetization pattern of the sample is estimated for each measurement. To do this, the distorting effect of the cantilever canting angle is first compensated by multiplying the measurement with the square of the inverse of the  $LCF(\mathbf{k}, \theta)$ . The

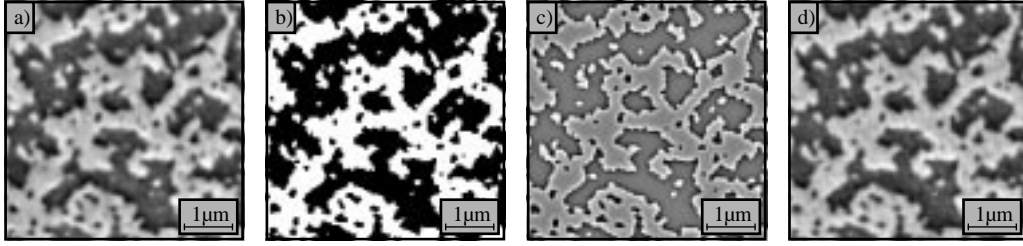


Figure 3.4: Example of the calibration process.

a) MFM measurement of a Cu/Ni(10 nm)/Cu/Si(001)-film.

b) Magnetization pattern, determined by applying a discrimination level to the measured signal.

c)  $z$ -derivative of the  $z$ -component of the stray field, calculated using the magnetization pattern.

d) Simulation of the MFM measurement using the instrument calibration function,  $ICF_{dH_z}^{\Delta f}(\mathbf{k})$ .

magnetization of the calibration sample is perpendicular to the sample plane, as will be discussed in section 4.1. Therefore, the areas magnetized in the  $+z$ -direction can therefore be separated those magnetized in the  $-z$ -direction using a discrimination level for the frequency shift (figure 3.4b). A histogram of the frequency shift values is made to determine the discrimination level, . This histogram will typically have two peaks. The frequency-shift at which the minimum between these peaks occurs is used as the value for the discrimination level.

From the magnetization pattern, the sample stray field or field  $z$ -derivative is calculated in a plane parallel to the sample, located at the tip end, using equation 4.16. In the example, the field derivative is calculated (figure 3.4c) in order to determine the instrument calibration function that relates the measured frequency shift to the stray field derivative,  $ICF_{dH_z}^{\Delta f}(\mathbf{k})$ .

The instrument calibration function can now be determined by dividing the Fourier components of the measurement by those of the stray field derivative. This calibration contains errors caused by small contributions of sample topography, small local modifications of the sample magnetization, image boundary effects, errors in the magnetization estimate, noise etc.

The errors in the calibration function are reduced by averaging over several calibration functions obtained from different MFM measurements. The statistical error in the averaged calibration function can be estimated from the deviations of the individual calibration functions from this average. Assuming the errors to be independent of one another, their standard deviation,  $\sigma_{ICF}(\mathbf{k})$ , can be estimated:

$$\sigma_{ICF}(\mathbf{k}) = \sqrt{\frac{1}{n(n-1)} \sum_{i=1}^n (ICF_i(\mathbf{k}) - \langle ICF(\mathbf{k}) \rangle)^2} \quad , \quad (3.23)$$

This standard deviation is a lower estimate of the error, since it does not include systematic errors, caused for example by the nonzero (although very small) width of the domain wall or by an error in the piezo calibration. The Fourier amplitude of the

$ICF_{dH_z}^{\Delta f}(\mathbf{k})$  is averaged over circles with a constant size of  $\mathbf{k}$  to plot the sensitivity and the sensitivity error of the MFM as a function of  $k$  (figure 3.5).<sup>3</sup>

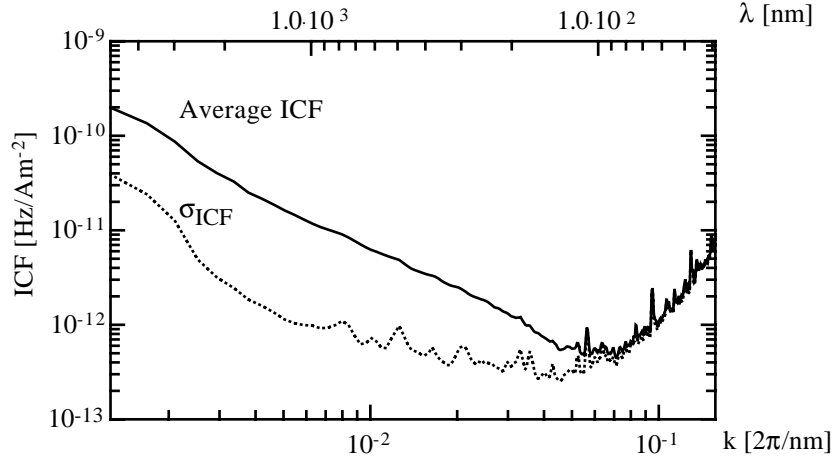


Figure 3.5: Circular average of the average instrument calibration function and its standard deviation as a function of  $k$  and  $\lambda$ . The Instrument calibration function is undetermined for  $\lambda$ -values smaller than 100 nm.

The error in the estimated magnetization pattern can now be reduced by an iterative process (figure 3.3); a better estimate is obtained by deconvolving the measurement with the averaged transfer function. The iteration is stopped when the statistical error in the instrument calibration function stops decreasing.

To test the calibration function, one can use it to simulate a measurement, as is shown in figure 3.4d. The simulated image is computed by multiplying the stray field calculated from the assumed magnetization pattern with the instrument calibration. The rms error between the example measurement and the corresponding simulation is 0.22 Hz, compared to the 3.0 Hz total frequency variation in the images. This error can be attributed to three sources: noise in the measurement, errors in the instrument calibration and errors in the assumed magnetization pattern. The error due to the statistical error in the instrument calibration function can be estimated by multiplying the Fourier components of the calculated stray field derivative with  $\sigma_{ICF}(\mathbf{k})$ . This gives an expected error of 0.14 Hz. The error due to inaccuracies in the magnetization pattern is approximately 0.14 Hz. It is found by subtracting the error due to the calibration error and the measurement noise from the total error.

### 3.3.2 Stray Field of the Tip

The flux density distributions of a Basel type EBID-tip and a microfabricated Si type tip (see section 2.3) were calculated from their corresponding Instrument calibration functions using equations 3.19 and 3.14 (see figure 3.6). Assuming the tip stray field vanishes at the boundaries of the image, the maximum flux density at the tip end is 11 mT for the Si-tip, and 10 mT for the EBID tip. The field of the EBID-tip decreases

<sup>3</sup>This does not imply that the stray field of the tip has cylindrical symmetry, it only implies that the deviation from the cylindrical symmetry has not yet been evaluated.

much faster away from the center of the tip, which results in a better measurement resolution. Moreover, the combination of the lower peak field, and the faster decay of the field reduces the influence of the tip on the sample magnetization.

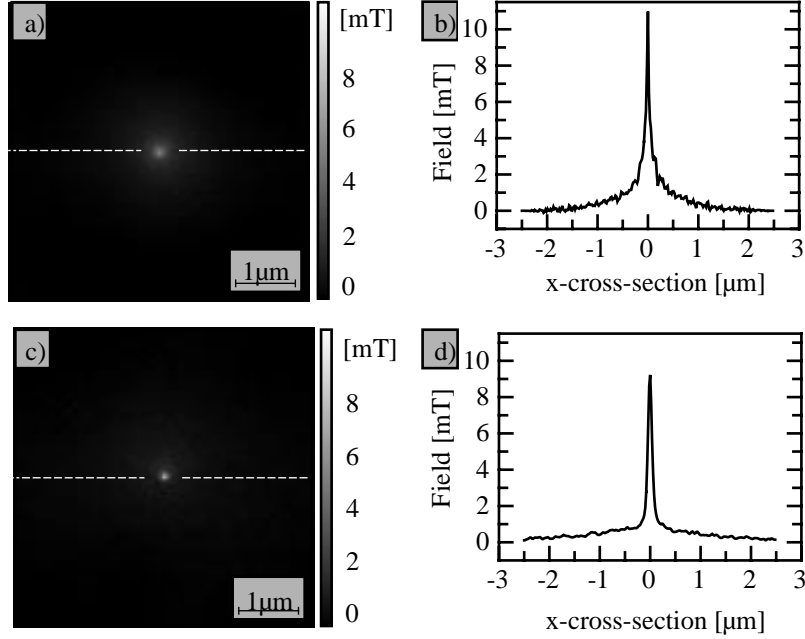


Figure 3.6:  $z$ -component of the magnetic flux density of different tips. a) magnetic flux density of the Si-tip in a plane located at the geometrical end of the tip. b)  $x$ -cross-section of the distribution shown in a). c) magnetic flux density of the EBID-tip in a plane located at the geometrical end of the tip. d)  $x$ -cross-section of the distribution shown in c).

The obtained field distribution can be compared to the results of studies made with electron microscopy. In the work by Streblechenko et al.,[50] the stray field of MFM tips was quantitatively measured using electron holography. The maximum field was found to be 62 mT at the tip surface. Unfortunately, no specifications were given for the thickness and material of the magnetic coating. In the work of Ferrier et al. [51], the magnetic field distribution was measured using electron tomography. No absolute field measurements were made, but the distribution of the tip field agrees well with the measurements presented in this thesis, although the plane of measurement was not canted with respect with the cantilever surface. Again no tip specifications were given.

### 3.4 Evaluation of the Experimental Image Contrast

In the following, the contrast formation of experimentally determined tip equivalent charge ( $\sigma_{tip}^{Si}(\mathbf{k})$  for the Si-tip and  $\sigma_{tip}^{EBID}(\mathbf{k})$  for the EBID-tip) is compared to the contrast formation of some simple tip models such as a magnetic point dipole, a magnetic point charge, and a model based on the geometry of the Si-tip. In figure 3.7 the average

amplitudes of the Fourier components of the experimental and model tip-calibration function are plotted as a function of  $k$ . To make a direct-space comparison between the measured calibration and the different tip models (figure 3.8), a measurement was made with the Si-tip on the Cu/Ni/Cu sample containing 7 nm of Ni at a measurement distance of 53 nm (figure 3.8a). To simulate the MFM measurement shown in figure 3.8a, a magnetization pattern was generated, using the procedure of section 3.3 (figure 3.8b). The  $z$ -derivative of the stray field was then calculated using equation 4.15 and frequency shift images were calculated using the instrument calibration function.

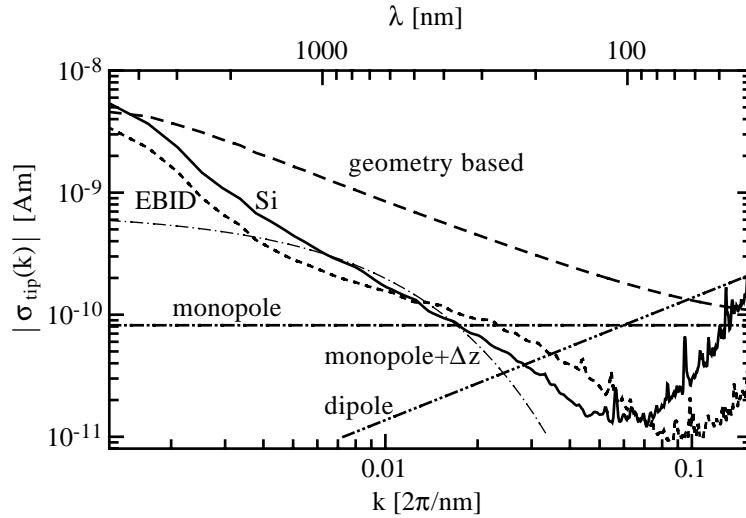


Figure 3.7: Average amplitude of the Fourier components of several tip calibration functions as a function of  $k$ .

### 3.4.1 Results Obtained with Calibrated Tips

The best agreement between simulation and experiment is obtained if the experimentally determined tip equivalent charge distribution is used. figure 3.8c and figure 3.8d have been calculated from the magnetization pattern of figure 3.8b using  $\sigma_{tip}^{Si}$  and  $\sigma_{tip}^{EBID}$ , respectively. It is noteworthy that this agreement between measurement and simulation was obtained without any free parameters. The location of the cross-section along the  $x$ -direction was chosen to run across many domain boundaries, whereas the one along the  $y$ -direction intersects only a few domain boundaries. Comparing the cross-sections in figure 3.8c to those in figure 3.8a, it is found that they match well, including the behavior in the center of large domains and the asymmetry of certain domain boundaries.

The experimentally determined tip equivalent charge distributions are plotted as a function of  $k$  in figure 3.7, ( $\sigma_{tip}^{Si}$ , solid line, and  $\sigma_{tip}^{EBID}$  dotted line). The calibration function of the Si-tip decays approximately with  $k^{-1.5}$ , whereas the one of the EBID-tip decays slower with  $k^{-1.3}$ . This gives the EBID-tip slightly better imaging properties.<sup>4</sup>

<sup>4</sup>The increase of  $\sigma_{tip}$  at small wavelength is due to noise in the calibration.

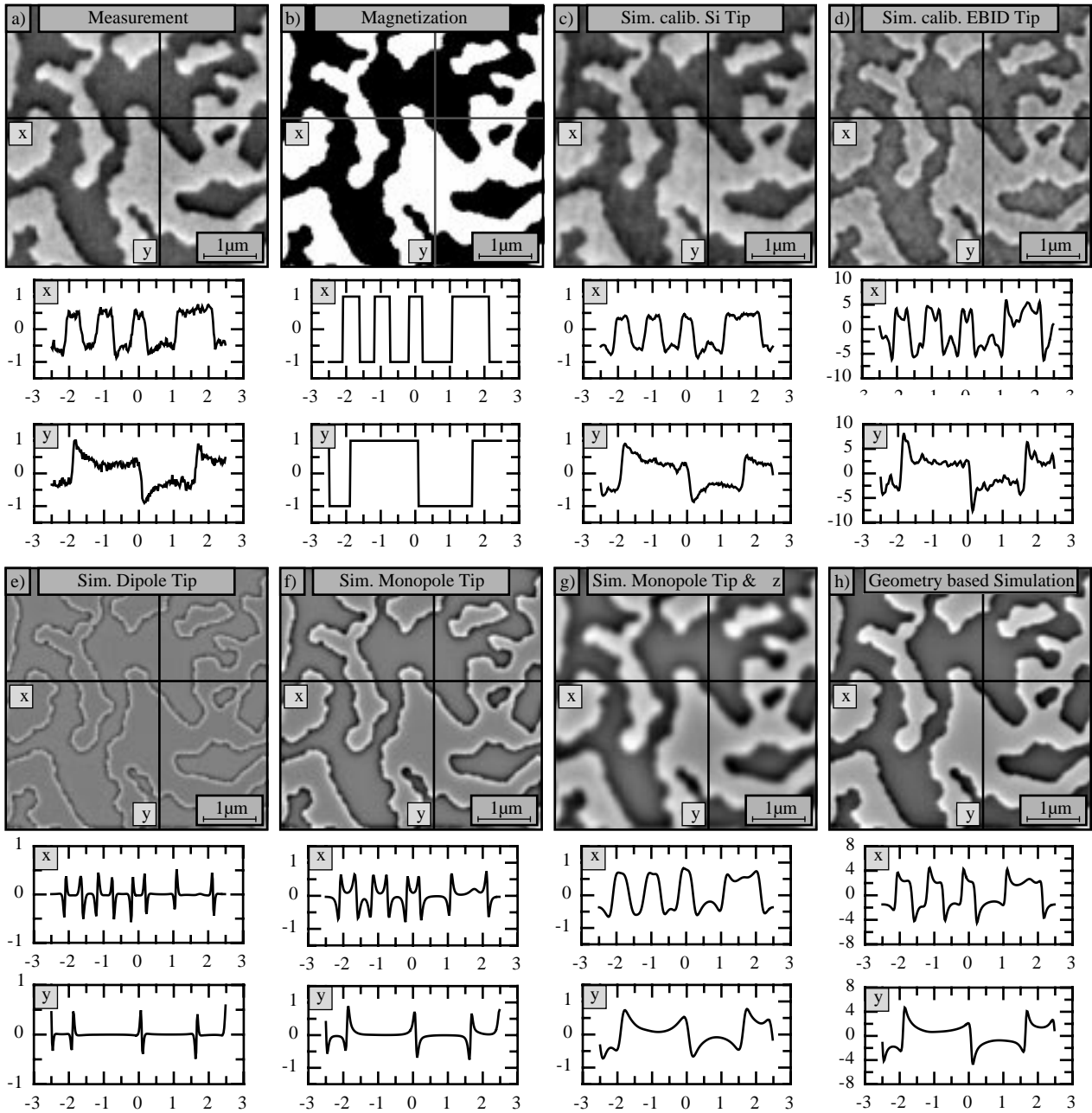


Figure 3.8: Effect of the calibration on the measurement contrast in direct space. a) measurement, b) magnetization pattern, c) simulation using Si-tip calibration, d) simulation using EBID tip calibration, e) point dipole, f) point monopole, g) point monopole with additional distance, h) Si-tip geometry based model.

### 3.4.2 Point-pole Tip Models

The most commonly used tip model, first proposed by Mamin et al.[52], describes the tip as the sum of an ideal monopole,  $q_0$ , and a point dipole,  $\mathbf{m} = (m_x, m_y, m_z)$ . One can easily show that this model is equivalent to using the tip-equivalent charge:

$$\sigma_{tip}(\mathbf{k}) = q_0 + \mathbf{m} \cdot \nabla^* \quad , \quad (3.24)$$

with  $\nabla^* = (-ik_x, -ik_y, -k)$ . Usually, this model is further simplified to a magnetic point dipole, oriented along the z-axis. The tip-calibration function,  $\sigma_{tip}^{dipole}(\mathbf{k})$  for this simplified model (equation 3.24 with  $q_0 = 0$ ) is represented by the dashed-double-dotted line in figure 3.7. In contrast to the experimentally determined tip equivalent charge distributions (Si-tip: solid line, EBID-tip: dotted line),  $\sigma_{tip}^{dipole}$ , increases with decreasing wavelength. A measurement was simulated, using zero canting angle of the cantilever (figure 3.8e). The magnetic dipole strength ( $\mathbf{m}$  in equation 3.24) was adjusted to achieve the best fit between the dipole tip simulation and the Si-tip measurement. A dipole moment,  $|\mathbf{m}|$  of  $13.7 \cdot 10^{-19} \text{ Am}^2$  was found to give the best fit. As is to be expected, the image contrast is much too sharp, and the signal in the middle of the domains is too small. Besides this, the asymmetry visible in the y-cross-sections of the measurement does not occur in the simulation.

In a previous paper [24], a magnetic point charge (monopole) was used as a model for an EBID tip, coated with a thin cobalt layer. This tip was used to measure the stray field of a perpendicular magnetization pattern. The size of the magnetic point charge was fitted by comparing the magnitudes of the simulated stray field and the measurement. With this point charge approximation an excellent agreement between the measured and simulated data was obtained. However, the agreement required a much larger distance between the magnetic point charge and the sample than the typical tip-to-sample distances used in the experiment. Similar observations have been reported by Belliard et al. for a monopole model [46] of the tip, and by Mamin et al. for the dipole model of the tip [52].

Here, a monopole model is first considered, with  $\sigma_{tip}^{monopole}(\mathbf{k}) = q_0$ , located at the experimentally determined tip-to-sample distance. This model is represented in figure 3.7 by the (thick) dashed-single-dotted line. It is clear that the monopole model without additional distance does not correspond well to the measured tip calibration, although the correspondence is better than in the case of the dipole model. Again, a measurement was simulated, using zero canting angle of the cantilever (figure 3.8f). The charge of the monopole was adjusted to get the best fit between the Si-tip measurement and the dipole tip simulation, giving a monopole size of  $8.2 \cdot 10^{-11} \text{ Am}$ . Again, the image contrast is too sharp, there is not enough signal in the middle of the domains and the y-asymmetry does not occur in the simulation.

To improve the agreement between simulation and measurement, the canting of the cantilever can be taken into account, and the effect of the spatial extent of the tip can be modeled by placing the magnetic point charge a distance,  $\Delta z$ , away from the geometrical end of the tip. This tip equivalent charge distribution is plotted in figure 3.7 as a thin dashed-single-dotted line. In a limited wavelength range, this model corresponds well with the experimental tip calibration functions (solid and dotted lines). The best fit of the simulation (figure 3.8g) to the measurement (figure 3.8a) is obtained with a



monopole charge of  $6.9 \cdot 10^{-10}$  Am, and an additional distance,  $\Delta z = 125$  nm (total distance: 178 nm). Interestingly, both, the value of the magnetic charge on the tip and the total tip-to-sample distance is close to the values found for the EBID-tip used in [24] ( $q_0 = 2.72 \cdot 10^{-9}$  Am and a tip-to-sample distance of 176 nm). It should be noted that the EBID tip was coated by a Co layer with a thickness of 25 nm, whereas the Si-tip used here was coated by an Fe layer with a thickness of only 7.3 nm. The asymmetry of the contrast at the domain boundaries in the y-cross-section is now reproduced by taking the canted orientation of the cantilever into account. Furthermore, the contrast of the image is in quite good agreement with the experimental observation. However, the improved monopole model performs well only in a limited range of wavelengths, because the optimum additional distance,  $\Delta z$ , depends on the domain size. This also becomes obvious from a closer inspection of the line sections in direct space. There is a good agreement between the simulated and experimental x-cross-section, indicating a good fit for the smaller domain size. However, the signal in the middle of the large domains visible in the y-cross-section is smaller than that of the measurement. Thus, if the monopole strength and distance are fit on a sample with a different domain size, different values are found for each sample, as was described in the Master's thesis of Viola Barwich [53]. This makes this model unsuitable for calibrating the imaging properties of the MFM.

### 3.4.3 Tip Model Based on Tip Geometry

As an alternative for the direct experimental determination of the tip calibration function, the imaging properties of the tip can be calculated from the magnetization structure of the tip. Assuming the magnetization structure of the tip were known, the calibration function of the tip can be calculated using the integral in equation 3.13.

Whereas the geometry of the tip can be derived from scanning electron microscopy images (SEM) with high precision (see figure 2.5b), the experimental determination of the micromagnetic structure of the tip remains a challenge. After the tip preparation, the tips are magnetized along the cantilever normal,  $\mathbf{n}$ , in a field of approximately 0.4 T. Based on the knowledge of the magnetization of the geometry of MFM tips determined by SEM, the following assumptions of the tip magnetization are made:

1. The coated tip-faces are assumed to have a triangular shape.
2. The ferromagnetic Fe coating has the saturation magnetization of iron, a uniform thickness, and a geometry exactly equal to the one of the tip-faces.
3. After the tip is magnetized parallel to the cantilever normal, the magnetization is assumed to relax in the plane of the ferromagnetic coating. It is assumed that the magnetization vector in a tip-face runs parallel to the projection of the cantilever normal on the surface of the triangle. This leads to the formation of magnetic surface charges at the edges of the tip-faces.

With these assumptions, the volume charge distribution vanishes ( $\rho_M = 0$ ), and the surface charge distribution,  $\sigma_M$  are known. Numerical evaluation of the integral in equation 3.13 can be used to calculate the tip-calibration function,  $\sigma_{tip}^{SEM}(\mathbf{k})$ .

For comparison with the experimentally determined transfer function, the SEM-model transfer function,  $\sigma_{tip}^{SEM}$  is plotted as a function of  $k$  in figure 3.7 (dashed line). In contrast to the monopole and dipole models the SEM-model gives a  $\sigma_{tip}^{SEM}$  that decays with decreasing wavelengths. Using the numerically determined tip calibration function and equation 3.19, a good qualitative agreement between the simulation (figure 3.8h) and the measured data (figure 3.8a) is obtained. However, the domain boundaries still appear too sharp in the simulated image and the asymmetry of the domain boundaries in the x-direction is not visible in the experimental data. Furthermore the total frequency variation in the image is about a factor of 5 larger than that of the measurement. These deficiencies arise from the rather strict and simple assumptions on which the SEM-model is based:

1. The magnetization of the Fe-film of the tip has been assumed to be equal to the saturation magnetization of single crystalline iron. However, in reality the iron film may be partially oxidized, because it was deposited in a moderate vacuum in the high  $10^{-7}$  mBar-range. In addition, the granular, polycrystalline structure of the iron film may further decrease the average magnetization of the iron thin film. These effects are expected to be especially strong at the tip apex.
2. The magnetization vector of the tip was assumed to be parallel to the projection of  $\mathbf{n}$  on the surface of the triangle. This leads to the formation of magnetic surface charges at the geometrical edges of the tip-faces. In reality the magnetization distribution of a the triangular tip face may slightly re-adjust to minimize the total energy. It can be expected that the re-orientation of the magnetization vector reduces the magnetic charge on the side faces of the ferromagnetic coating.

Generally it can be expected that the magnetic charge is distributed over a larger volume and that the magnetization direction is more parallel to the side face of the ferromagnetic coating. This minimizes the total magnetic energy of the MFM tip, and lowers the image contrast.

In spite of the deficiencies of the SEM model, it explains some important experimental facts of magnetic force microscopy:

1. The signal in the middle of the micron-sized domains is of the same order of magnitude as the signal close to the domain boundaries.
2. Simulations using simple point-pole models require a tip-to-sample distance much larger than the experimental one in order to obtain a reasonable agreement with the experimental data.

Both observations can be explained by the extended magnetic charge distribution of the tip. There is no need to invoke a perturbation of the magnetization of the sample by the tip as an explanation of the MFM-contrast, as suggested by Belliard et al. [46].

### 3.5 Comparison of MFM to Other Methods

The calibration of the MFM is used to compare the stray-field sensitivity of the MFM to that of other scanning stray-field measurement methods in section 3.5. Here, the

discussion is limited to two of those: Scanning Hall Microscopy and Scanning SQUID Microscopy.

The stray field sensitivity of the MFM can be calculated as a function of  $k$  by dividing the measurement noise (see section 2.3) by the instrument calibration function. If it is assumed that the noise, given in section 2.3, is uniformly distributed over the measurement bandwidth, the frequency noise density is  $9 \text{ mHz}/\sqrt{\text{Hz}}$  at room temperature, and  $1.4 \text{ mHz}/\sqrt{\text{Hz}}$  at 6 K. To allow for a better comparison with other magnetic imaging methods, the magnetic flux density noise was computed instead of the field gradient noise. To do this, the ICF from B-field to frequency shift is calculated from the ICF from H-field derivative to frequency shift by multiplying it with  $k/\mu_0$  (See equations 3.18, 3.19). The obtained magnetic flux density noise at room temperature and close to LHe temperature is plotted as a function of  $k$  and  $\lambda$  in figure 3.9 .

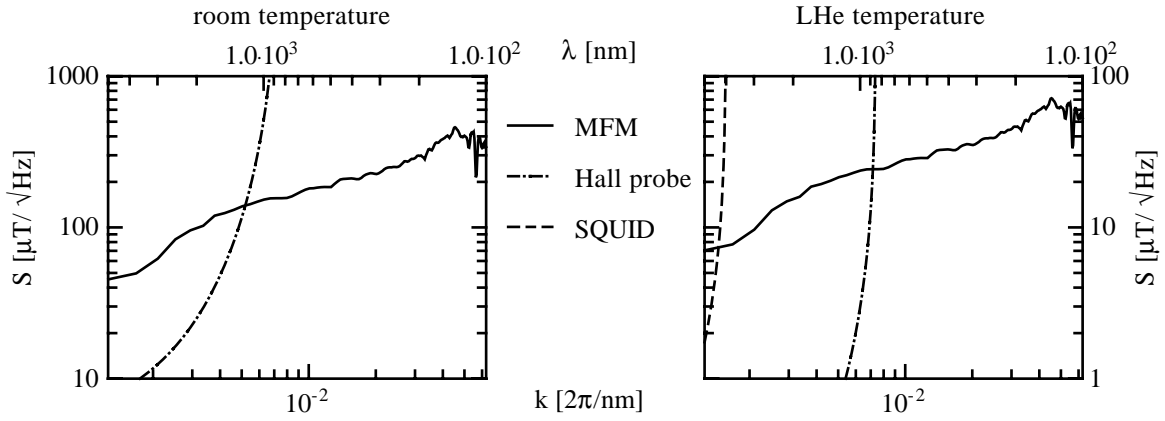


Figure 3.9: Smallest measurable magnetic flux–density as a function of  $k$  and  $\lambda$  for MFM (measured), scanning Hall probe Microscopy and Scanning SQUID microscopy (simulated).

To estimate the sensitivity of the Scanning Hall Probe and Scanning SQUID microscopes, it is assumed that they have a constant sensitivity over a square of the sensor size, and that the sides of the square are parallel to the x– and y–directions. Ignoring the slightly canted orientation of the probes, the sensitivity of these instruments to the stray field at the MFM measurement distance is given by:

$$S(\mathbf{k}) = S_0 \frac{k_x k_y l^2}{4 \sin(k_x l/2) \sin(k_y l/2) \exp(k \Delta z)} \quad , \quad (3.25)$$

with  $S_0$  the sensitivity of the probe for homogeneous fields, and  $l$  the length of the sides of the square probe. Literature values for  $S_0$ ,  $l$  and the distance increase  $\Delta z$  are given in table 3.1. The sensitivity plots of the Scanning Hall Probe microscopes and scanning SQUID microscope in figure 3.9 were calculated using these values and equation 3.25. Unsurprisingly, the sensitivity of these instrument rapidly worsens (increases) for magnetization wavelengths of the order of the sensor size. Probably, the sensitivity functions of these instruments have a more smooth sensitivity profile than the square, which would result in a less drastic sensitivity cut–off at these frequencies. However,

this may not only lead to a slightly better sensitivity at small wavelengths, but also to a worse sensitivity at longer wavelengths.

Sensor	$l[\mu\text{m}]$	$\Delta z[\mu\text{m}]$	$S[\mu\text{T}/\sqrt{\text{Hz}}]$
Hall Probe [54] at 300 K	0.85	0.5	3.8
Hall Probe at $\approx 4.2$ K	0.85	0.5	0.022
SQUID [55] at $\approx 4.2$ K	4.0	2.0	0.033

Table 3.1: Literature values for the sensitivity, probe size and measurement distance of Scanning Hall and Scanning SQUID microscopes.

## Chapter 4

# MFM on Ferromagnetic Layers, Applied to Cu/Ni/Cu Sandwiches

The description of magnetic materials is generally divided in five level (see figure 4.1). The lowest level is the description of the material on the atomic level, the highest level describes the hysteresis loop of a macroscopic sample. Ideally, the theoretical

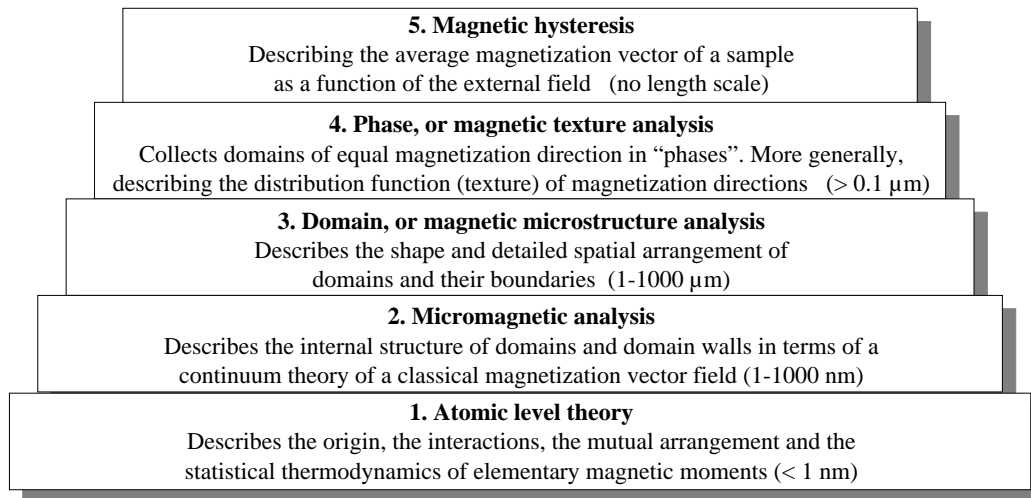


Figure 4.1: The hierarchy of descriptive levels of magnetic materials (from [9]).

understanding of the higher level phenomena is built upon lower level models. On the other hand, the experimental investigation of the higher level behavior can give insight in the behavior of the material on a lower description model. For example, measurement of magnetization as a function of temperature can be used to understand the mechanism that is responsible for the magnetic ordering of the atomic magnetic moments.

In this chapter, it will be shown that Magnetic Force Microscopy can be used for both the study of magnetic domains and their micromagnetic structure. It was pointed out in section 3.1, that the interpretation of MFM data of ferromagnetic samples is

most straightforward for measurements on magnetically hard samples, with a large lateral variation of their magnetic stray field. This is the case for thin-film samples with a magnetic anisotropy that prefers an orientation of the magnetization perpendicular to the sample surface. It is therefore expected that MFM can contribute to the understanding of the behavior of such samples, and in particular to the understanding of the cause of this perpendicular anisotropy. In this chapter, measurements are presented that were performed on epitaxially grown 5 nm Cu/Ni/200 nm Cu/Si(100) sandwiches, prepared at the MIT by Kin Ha [56, 57]. Samples with this structure have an exceptionally large thickness range in which the perpendicular orientation of the magnetization is preferred. This low sensitivity of the effect on the sample thickness is expected to simplify the study of the perpendicular anisotropy. The properties of these samples known from literature are discussed in more detail in section 4.1. Following this, some general properties of the domains in these samples are discussed in section 4.2. Finally, measurements of the magnetization state of these samples are presented in section 4.3.

## 4.1 Properties of Cu/Ni/Cu/Si(001)

Following the scheme in figure 4.1, the micromagnetic behavior of a sample must be understood, in order to explain the properties of the magnetic domains in these samples. In the micromagnetic approach, the free energy of the sample is expressed in terms of a continuous magnetization distribution,  $\mathbf{M}(\mathbf{r})$ . The occurrence of the individual terms in the free energy can in turn only be explained by atomic level theories. To a good approximation, the magnitude of the magnetization is independent of its direction and location. Therefore the magnetization can be written as  $\mathbf{M}(\mathbf{r}) = M_s \mathbf{m}(\mathbf{r})$ , with  $M_s = |\mathbf{M}(\mathbf{r})|$  and  $|\mathbf{m}(\mathbf{r})| = 1$ . The micromagnetic properties of the Cu/Ni/Cu/Si(001) samples are discussed in section 4.1.1. From the micromagnetic properties, one can derive the magnetization state of the Ni layer can be derived, as is described in section 4.1.2.

### 4.1.1 Micromagnetic Properties

The free energy terms considered in this thesis are the exchange energy, the magnetocrystalline energy, the magnetostrictive energy and the magnetostatic energy. Each of these terms will be described in more detail in the following. In addition, an overview of the magnitude of the parameters that determine the behavior of these free energy terms is given in table 4.1.

#### Exchange Energy

The exchange energy is the cause of the parallel alignment of the atomic magnetic moments in ferromagnetic materials, which manifests itself as a macroscopic magnetic moment. In micromagnetics, the exchange energy density,  $E_x$  is written as:

$$E_x = A(\nabla \cdot \mathbf{m})^2 \quad , \quad (4.1)$$

with  $A$  the exchange constant. From equation 4.1, it is clear that the exchange energy is isotropic for the direction of the magnetization. Thus the magnetic moment of the

property	symbol	value	units
saturation magnetization	$M_s$	$0.48 \cdot 10^6$	A/m
exchange constant	$A$	$10.3 \cdot 10^{-12}$	J/m
shape anisotropy constant	$K_d (= \frac{1}{2} \mu_0 M_s^2)$	$0.15 \cdot 10^6$	J/m <sup>3</sup>
1st cubic crystal anisotropy constant	$K_{c,1}$	$-5.5 \cdot 10^3$	J/m <sup>3</sup>
2nd cubic crystal anisotropy constant	$K_{c,2}$	$-2.5 \cdot 10^3$	J/m <sup>3</sup>
interface anisotropy constant	$K_s$	$0.71 \cdot 10^{-3}$	J/m <sup>2</sup>
linear strain anisotropy constant	$B_1 \left(1 + \frac{2c_{12}}{c_{11}}\right)$	$14.14 \cdot 10^6$	J/m <sup>3</sup>
quadratic strain anisotropy constant	$\frac{1}{4} A_{11} \left(3 + 2 \frac{2c_{12}}{c_{11}} - \left(\frac{2c_{12}}{c_{11}}\right)^2\right)$	$-1.07 \cdot 10^9$	J/m <sup>3</sup>

Table 4.1: Properties of the samples used in this thesis. Values of  $K_{c,1}$  and  $K_{c,2}$  taken from [58], other anisotropy constants taken from [56, 57]

sample could point in any direction in the absence of a magnetic field, and would always align with an applied external magnetic field. In reality however, the free energy is anisotropic for the direction of the magnetization. This anisotropy is caused by the atomic scale spin-orbit interaction, and the macroscopic self-demagnetizing field of the sample. In the following, the anisotropy terms of interest for the Cu/Ni/Cu/Si(001) samples are discussed. A more general overview of the different anisotropy contributions is given by Blügel.

### Crystal Anisotropy

The crystal anisotropy describes the tendency of the magnetization to align with certain crystallographic axes of the sample. It is caused by spin-orbit interaction. Generally, the crystalline anisotropy of a material is described in terms of the direction cosines of the magnetization direction on the crystalline axes of the material. In the samples used in this thesis, the (fcc) Nickel layer has a (001) surface and the crystal axes are aligned with the x-, y- and z-coordinate axes of the sample, with the z axis in the direction of the surface normal. In this case, the direction cosines of the magnetization along the crystal axes are identical to the cartesian components of  $\mathbf{m}$ . Therefore, the crystal anisotropy energy density  $E_c$ , limited to terms depending on up to the sixth power of

$m$ , can be described as<sup>1</sup>:

$$E_c = K_{c,1}(m_x^2 m_y^2 + m_y^2 m_z^2 + m_z^2 m_x^2) + K_{c,2} m_x^2 m_y^2 m_z^2 \quad . \quad (4.2)$$

Because both  $K_{c,1}$  and  $K_{c,2}$  are negative for nickel, the crystal anisotropy causes a preferential alignment of the magnetization with the  $\langle 111 \rangle$  directions (see for example [9]).

At the surface of a magnetic layer, or at interfaces between different layers, the symmetry is reduced, giving rise to an additional anisotropy term. For the (001) surface of the Nickel samples, the surface anisotropy energy density, limited to terms depending on up to second power of  $m$ , is given by:

$$E_s = -K_s m_z^2 \quad (4.3)$$

Based on the doubling of the range with perpendicular anisotropy, due to covering the Ni layer with the second Cu layer observed on similar samples by Bochi *et al.* [59], and on anisotropy measurements with a subsequent analysis using a second order spin-pair model performed by Ha, it was concluded that the surface anisotropy constant  $K_s$  is positive, favoring a magnetization out of the sample plane at the surface of the layer. However, a negative surface anisotropy is often assumed for this system in the literature. This assumption dates back to the first analysis of the anisotropy of this system by Jungblut *et al.*[60]. The negative value of the surface anisotropy was obtained from an analysis that used theoretical values for the strain in the layer. However, these theoretical values seem to overestimate the actual strain, which has been measured by Ha (see paragraph 4.1.1).

In general, the surface anisotropy may also depend on the roughness of the interface, as the symmetry is further changed at a step in the surface. Scanning Force Microscopy Measurements by Ha tentatively show that the surface of the Cu/Si(001) substrate on which the Ni is deposited is very flat, therefore this anisotropy contribution was not considered here.

### Strain Induced Anisotropy

The strain induced anisotropy describes the tendency of the magnetization to lie in directions that are determined by the strain tensor of the sample, and its magnetoelastic properties. Both strain induced anisotropy and magnetostriction are magnetoelastic effects, which are due to an interaction between the strain of a material and its preferential orientation of the magnetization. It is generally assumed that the same mechanisms that are responsible for crystal anisotropy, are also responsible for magnetoelastic effects.

It is to be expected that magnetoelastic effects have a considerable influence on the Cu/Ni/Cu samples, because Magnetoelastic effects in Ni are relatively strong, compared to the other magnetic elements and because the Ni layers are considerably strained. This large strain is due to the lattice mismatch between Cu and Ni. The lattice mismatch,

---

<sup>1</sup>The free energy terms that are independent of the magnetization direction are ignored. These may contribute to the temperature-dependent behavior of the sample, but this is not considered here.



$\eta$ , between the copper substrate and the Ni layer can be defined as:

$$\eta = \frac{a_{Cu} - a_{Ni}}{a_{Ni}} \quad , \quad (4.4)$$

with  $a_{Cu}$ ,  $a_{Ni}$  the (bulk) lattice constants of Cu and Ni. In this definition, the lattice mismatch is 2.6%. This mismatch causes a much larger strain than is obtainable by the application of macroscopic stresses to bulk samples. The strain in the layer is assumed constant in layers below a critical thickness,  $d_c$ . At thicknesses above the critical thickness, the strain in the layer is relaxed by the formation of dislocations. The biaxial in-plane strain<sup>2</sup>  $e_0(d)$  of the films was measured by Ha using X-Ray diffraction. In the thickness range from 3 to 12 nm, the in plane strain was found to fit the curve:

$$e_0 = \eta \left( \frac{d_c}{d} \right)^{2/3} \quad (4.5)$$

with a fitted  $d_c$  of 2.7 nm, which agrees moderately well with the value of 1.6 nm found by TEM experiments [61, 62]. This behavior of the strain is significantly different from the dependence  $e_0(d) = \eta \frac{d_c}{d}$ , with  $d_c = 4.2$  nm used by Jungblut *et al.*

Due to the biaxial in-plane strain, the crystal structure of the Ni layer is effectively changed into a centered tetragonal structure. Therefore, it is to be expected, that the strain induced anisotropy terms reflect the symmetry of this structure. If only terms up to the second order in  $m$  are taken into account, this strain-induced anisotropy energy  $E_{me}$  is given by:

$$\begin{aligned} E_{me} &= -K_{me}(e_0(d))m_z^2 \\ &= - \left[ B_1 \left( 1 + \frac{2c_{12}}{c_{11}} \right) e_0(d) + \frac{1}{4}A_{11} \left( 3 + 2\frac{2c_{12}}{c_{11}} - \left( \frac{2c_{12}}{c_{11}} \right)^2 \right) e_0^2(d) \right] m_z^2 \end{aligned} \quad (4.6)$$

with  $c_{11}$  and  $c_{12}$  two elastic constants of Ni,  $-(2c_{12}e_0(d))/c_{11}$  the out of plane strain and  $B_1$  and  $A_{11}$  two magnetoelastic constants of Ni. Whereas  $B_1$  is known to be positive from the literature, the analysis by Ha indicates that  $A_{11}$  is negative. Thus, the strain induced anisotropy favors a magnetization parallel to the sample plane for samples thinner than approximately 7.5 nm, and a perpendicular magnetization for thicker samples (see figure 4.2b).

One might expect that, analogous to the crystalline surface anisotropy, surface magnetoelastic anisotropy might play a role. This was done in a paper by Bochi *et al.* [59], where the negative anisotropy at small Ni thicknesses was explained by a negative surface magnetoelastic anisotropy. However, the analysis by Ha showed that these terms probably do not give a significant contribution to the total anisotropy.

### Shape Anisotropy

The shape anisotropy describes the tendency of homogeneously magnetized samples to align with certain directions that are determined by the (macroscopic) shape of the sample. This anisotropy is caused by the self-demagnetizing field of the sample. In a sample with an arbitrary, non homogeneous magnetization structure, the demagnetizing

---

<sup>2</sup>this is the magnitude of the strain in the plane of the layer

field tends to align the magnetization so that no magnetic poles exist. In other words, if the demagnetizing energy is the dominant energy term, the magnetization is divergence free inside the sample, and parallel to the sample surfaces. For thin magnetic films, this configuration is not possible, because the exchange interaction will force a homogeneous magnetization throughout the sample thickness. In this case, the demagnetizing energy,  $E_d$ , is given by:

$$E_d = -K_d m_z^2 \quad (4.7)$$

$$= \frac{1}{2} \mu_0 M_s^2 m_z^2 \quad (4.8)$$

Thus, the demagnetizing field favors a magnetization direction parallel to the sample surface. However, the demagnetizing energy can often be reduced by the formation of domains, in which case the expression for the demagnetizing field is not valid anymore. A fast method for calculating  $E_d$  for a domain structure in which the magnetization is constant throughout the layer thickness is given in appendix A

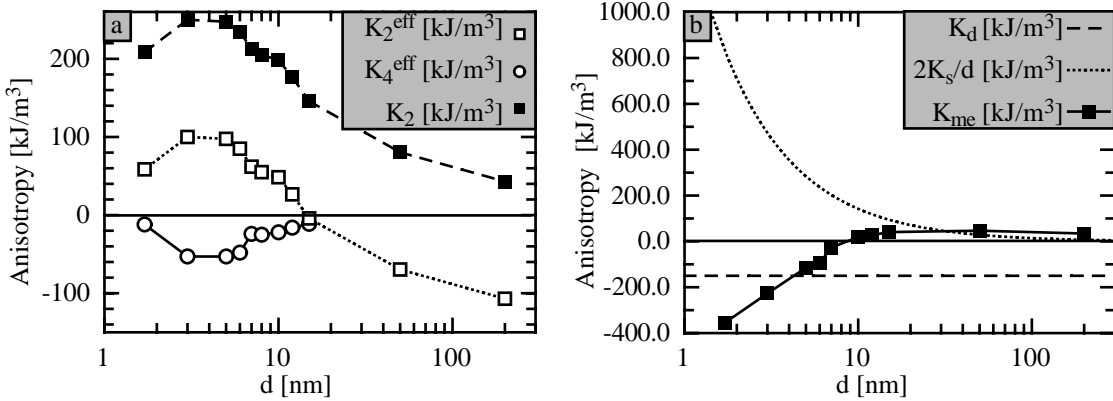


Figure 4.2: Behavior of the anisotropy as a function of Ni-layer thickness, according to Ha [56, 57].

- a) measured values of  $K_2^{eff}$ ,  $K_4^{eff}$  and calculated value of  $K_2$ .  
b) magnitude of the components of  $K_2^{eff}$ .

### 4.1.2 Orientation of the Magnetization

Using the anisotropy contributions described in the previous section, one can determine the preferential orientation of the magnetization. For this purpose, effective uniaxial anisotropy constants can be defined. Here the effective anisotropy constants  $K_2^{eff}$ ,  $K_4^{eff}$  are defined as:<sup>3</sup>

$$E_a = -K_2^{eff} \cos^2(\theta) + K_4^{eff} \sin^2(\theta) \cos^2(\theta) \quad , \quad (4.9)$$

<sup>3</sup>An alternative definition is also often used in literature, for example by Blügel [63] and Hubert [9]:  $E_a = K_{u1}^{eff} \sin^2(\theta) + K_{u2}^{eff} \sin^4(\theta)$ . It is important to note that the values of the measured anisotropy depend on the definition of the anisotropy, in this case  $K_{u1}^{eff} = K_2^{eff} + K_4^{eff}$  and  $K_{u2}^{eff} = -K_4^{eff}$ .

with  $E_a$  the total anisotropy energy and  $m_z = \cos(\theta)$ . Adding all uniaxial anisotropies to the second order in  $m_z$  from the previous section, one finds:

$$K_2^{eff} = 2K_s/d + K_{me}(e_0(d)) + K_d \quad . \quad (4.10)$$

The crystal anisotropy was not included in the effective anisotropy, because its magnitude is negligible, compared to the other anisotropy terms.  $K_2^{eff}$  and  $K_4^{eff}$  were measured using torque magnetometry, and the values of  $K_2^{eff}$  were additionally determined using vibrating sample magnetometry. Good agreement was found between the results of both methods. The values of  $K_2^{eff}$  and  $K_4^{eff}$  are plotted as open squares and open circles respectively in figure 4.2. All of the plotted values were determined using torque magnetometry, except for those of the samples containing 50 and 200 nm of Ni. The cause for the term  $K_4^{eff}$  is as yet unknown. To find it, a similar analysis as was applied to  $K_2^{eff}$  should be performed.

Using the measured values of  $K_2^{eff}$  and  $K_4^{eff}$ , one can draw a diagram of the energetically most favorable direction of the average sample magnetization (see fig.4.3).

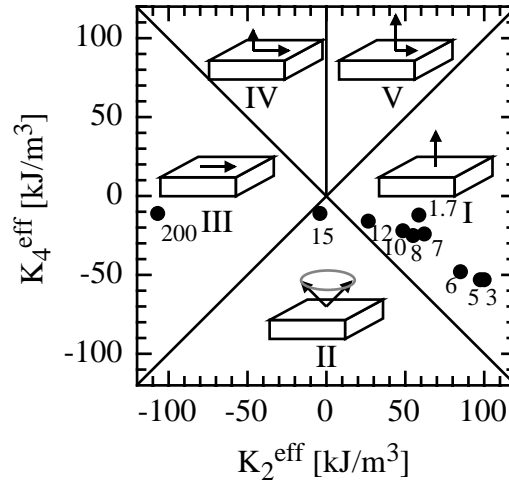


Figure 4.3: Five different phases of the preferred magnetization direction may occur, depending on the ratio of the second and fourth order anisotropy constants. The Cu/Ni/Cu samples are indicated by points, with the number indicating the Ni layer thickness  $d$  in nm. (The  $K_4^{eff}$  value for the 200 nm Ni layer was obtained by extrapolation)

This diagram contains five regions, that exhibit different behaviors of the preferential direction of the magnetization:

- I easy axis perpendicular to sample surface
- II easy directions canted with respect to surface (so called cone states)
- III easy directions parallel to the sample surface

IV easy directions parallel to the sample surface, metastable state perpendicular to the sample surface

V easy axis perpendicular to the sample surface, metastable state parallel to the sample surface

In the cone state, the energy directions lying in a cone around the surface normal are the energetically most favorable ones. The angle  $\theta_c$  between the stable magnetization direction and the surface normal is given by:

$$\cos(2\theta_c) = -\frac{K_2^{eff}}{K_4^{eff}} \quad (4.11)$$

From the marks in figure 4.3, it is clear that all the samples, except for the sample containing 15 nm of Ni, should have either an in-plane, or an out of plane remanence. For the sample containing 15 nm Ni,  $\theta_c = 56^\circ$ .

This representation of the magnetization state is too simple when the influence of the spatial distribution of the anisotropy contributions must be considered. For example, if the effective anisotropy is separated into a surface anisotropy term, and a volume anisotropy term, it can become energetically favorable for the magnetization to vary as a function of the depth in the sample,  $z$ . This would lead to a state in which the energetically most favorable direction of the average magnetization is canted with respect to the sample surface, even though no 4th order anisotropy term is present. Professor Thomas showed the occurrence of this state using stability considerations [64]. The thickness limits for a homogeneous magnetization perpendicular to the sample surface,  $d_\perp$ , and the limit for a homogeneous magnetization parallel to the sample surface,  $d_\parallel$  are given by:

$$d_\perp = 2\sqrt{\frac{A}{-(K_d + K_{me})}} \arctan\left(\frac{K_s}{\sqrt{-(K_d + K_{me})A}}\right) \quad (4.12)$$

$$d_\parallel = 2\sqrt{\frac{A}{-(K_d + K_{me})}} \text{Atanh}\left(\frac{K_s}{\sqrt{-(K_d + K_{me})A}}\right) \quad (4.13)$$

with  $\text{Atanh}$  the inverse function of the hyperbolic tangent. The resulting phase diagram is shown in figure 4.4. Additionally, the ‘‘conventional’’ stability limit between an in-plane and out-of-plane magnetization,  $K_2^{eff} = 0$  is plotted as a dotted line.<sup>4</sup>

It is remarkable that the sample containing 150 nm of Ni is the only sample that should be in the canted state, but this is also the only sample for which the cone state occurs ( $|K_4^{eff}| > |K_2^{eff}|$ ). Possibly, an inhomogeneous sample magnetization, due to the surface anisotropy, may give rise to an anomalous behavior of the torque that is misinterpreted as a fourth order anisotropy term.

## 4.2 Magnetic Domains

The magnetostatic energy of a sample in which the direction of the sample magnetization is distributed between the lowest energy axes is smaller than the magnetostatic energy of a sample with a homogeneous magnetization in one of these direction. However,

<sup>4</sup>Solving equation 4.10 one finds  $d = -2K_s/(K_d + K_{me})$ .

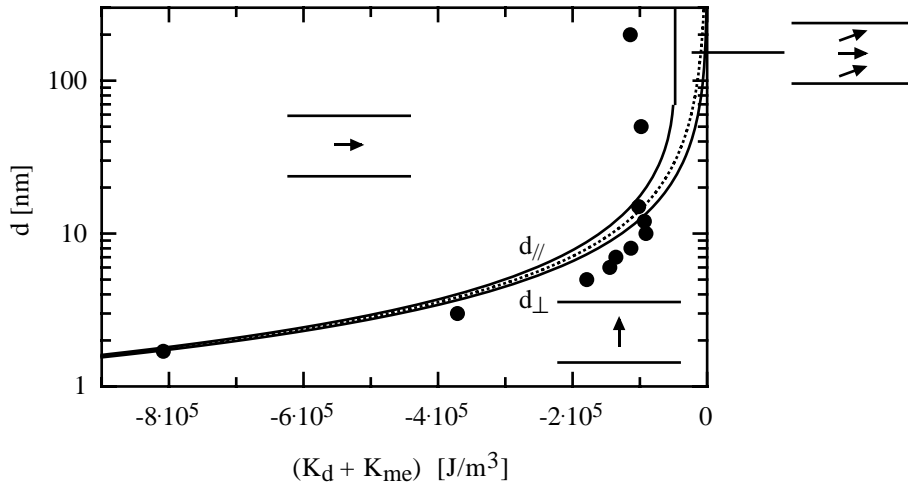


Figure 4.4: Boundaries of the surface domain state. The classical boundary between the in-plane and the out-of-plane states is indicated by the dotted line. The dots indicate the position of the Cu/Ni/Cu samples.

an instantaneous change of the magnetization direction is energetically unfavorable due to the exchange energy. On the other hand, a gradual change of the magnetization leads to an increase in the anisotropy energy. A minimum of the sum of these energy terms is reached by the formation of domains in which the magnetization is approximately homogeneously magnetized along an easy direction, separated by domain walls. The size of the domains is determined by the balance between the global decrease in magnetostatic energy and the local increase in the energy needed to create the walls [65].

#### 4.2.1 Stray Field of the Magnetic Domains

It was found in chapter 3 that the MFM images the sample stray field when performing measurements on magnetically hard samples. Therefore, if one wishes to know more about the magnetization of such a sample, it is necessary to know the relation between the sample magnetization, and the stray field of the sample. The relation between the stray field and the magnetization of the sample can be described in Fourier space in a similar manner as was used in section 3.2. Although this relation has been derived in the literature [29, 66], its derivation is repeated in appendix A in a more elegant way. For a sample that has a magnetic domain structure with a magnetization,  $\mathbf{M}$ , uniform throughout its thickness,  $d$ , the stray field above the sample surface can be computed in Fourier space using:

$$\mathbf{H}(\mathbf{k}) = -\frac{\nabla (1 - e^{-kd})e^{-kz}}{k} \begin{pmatrix} -ik_x/k \\ -ik_y/k \\ 1 \end{pmatrix} \cdot \mathbf{M}(\mathbf{k}) \quad , \quad (4.14)$$

where  $z$  is the distance to the surface of the sample. Following the findings of paragraph 3.2.1, only the component of the field in the  $z$ -direction is considered. For the simple

case of a sample, magnetized perpendicular to its surface ( $\mathbf{M} = (0, 0, M_z)$ ), equation 4.14 simplifies to:

$$H_z(\mathbf{k}) = \frac{(1 - e^{-kd}) e^{-kz}}{2} M_z(\mathbf{k}) \quad (4.15)$$

$$= \mathbf{HTF}_z(\mathbf{k}) M_z(\mathbf{k}) \quad , \quad (4.16)$$

whereas for an in-plane magnetization configuration,  $\mathbf{M} = (M_x, M_y, 0)$ , the z-component of the stray field is calculated using:

$$H_z(\mathbf{k}) = \frac{(1 - e^{-kd}) e^{-kz}}{2} \begin{pmatrix} -ik_x/k \\ -ik_y/k \\ 1 \end{pmatrix} \cdot \begin{pmatrix} M_x(\mathbf{k}) \\ M_y(\mathbf{k}) \\ 0 \end{pmatrix} \quad (4.17)$$

$$= \mathbf{HTF}_{x,y}(\mathbf{k}) \cdot \mathbf{M}(\mathbf{k}) \quad , \quad (4.18)$$

where  $\mathbf{HTF}_z(\mathbf{k})$  and  $\mathbf{HTF}_{x,y}(\mathbf{k})$  are called the field-transfer functions for a perpendicular and an in-plane magnetization structure, respectively.

If one wishes to determine the magnetization pattern from the stray field, equations 4.15 and 4.17 need to be solved for  $M_z$  and  $(M_x, M_y, 0)$ , respectively. However, there are limitations to doing this. To start, the average magnetization of the sample can't be determined, since for  $k = 0$ , the first factor in both equations vanishes. In other words, the average magnetization of an infinite thin film sample does not generate stray field, therefore its magnetization can't be determined from a stray field measurement. While no further limitations exist for the perpendicular magnetization pattern, the equation for the in-plane pattern has two unknowns, namely  $M_x$  and  $M_y$ . In fact, the divergence free (or solenoidal) part of the magnetization can't be determined, since it does not generate stray field. The curl-free, (or irrotational) part of the magnetization,  $\mathbf{M}_{cf}$ , can be determined using the constraint

$$\nabla \times \mathbf{M}_{cf} = \mathbf{0} \quad \Rightarrow \quad ik_y M_{cf,x}(\mathbf{k}) - ik_x M_{cf,y}(\mathbf{k}) = 0 \quad . \quad (4.19)$$

However, with additional constraints the total magnetization can in some cases be reconstructed. For example, if it is known that the magnitude of the magnetization is constant, the additional constraint  $M_x^2 + M_y^2 = M^2$  is imposed.

## 4.2.2 Domain Walls

To calculate the energy of the walls, their structure must be known. Generally, the structure of a wall can be described as a combination of two extreme cases: the Bloch wall and the Néel wall. In the Bloch wall, the magnetization changes in a divergence free manner, whereas in the Néel wall, the magnetization changes in a rotation free manner. As a consequence, no magnetic volume charges occur in a Bloch wall. Besides this, the surface charges of a layer with an easy axis perpendicular to its surface are reduced. The combination of these factors gives the Bloch type wall a lower magnetostatic energy than the Néel type, making it the preferred wall in magnetic layers with a perpendicular easy axis. To determine the domain wall energy and structure of a Bloch wall, an anisotropy constant  $K_2$  is used that excludes the shape anisotropy ( $K_2 = K_2^{eff} - K_d, K_4 = K_4^{eff}$ ),

see figure 4.2a. For  $0 < -K_4 < K_2$ , the wall surface energy density  $\gamma_w$ , and the wall width  $\delta_w$  of such a wall are given by [9]:

$$\gamma_w = 2\sqrt{A} \left[ \sqrt{K_2 + K_4} + \frac{K_2}{\sqrt{-K_4}} \arctan \sqrt{\frac{-K_4}{K_2 + K_4}} \right] \quad (4.20)$$

$$\delta_w = \pi \sqrt{A/K_2} \quad , \quad (4.21)$$

The calculated values of the wall width are shown in figure 4.5. For samples with a thickness comparable to the Bloch wall width, the sample magnetization can vary considerably throughout the sample thickness and the samples are not considered to be magnetic thin films anymore by convention. This is the case for Ni layers thicker than approximately 30 nm.

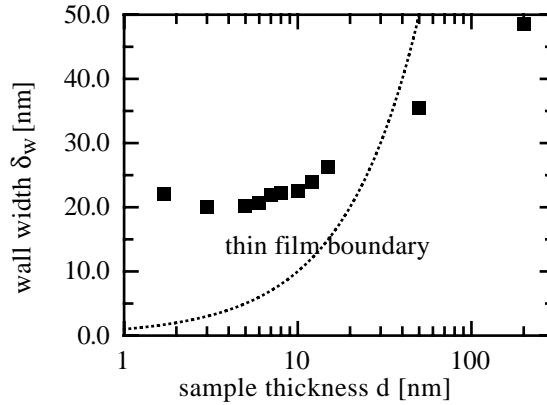


Figure 4.5: Wall width as a function of Ni layer thickness. Layers to the left of the dotted line  $d = \delta_w$  can be considered thin films.

To simplify the equations describing the domain wall somewhat, the contribution of  $K_4$  can be neglected. Then one obtains the more familiar expression  $\gamma_w = 4\sqrt{AK_2}$ , which gives an approximately 4% larger energy than the exact expression. The  $z$ -component of the magnetization in an isolated domain wall, parallel to the  $yz$ -plane of the simplified wall is given by:

$$m_z(x) = \tanh(\pi x/\delta_w) \quad . \quad (4.22)$$

The total magnetic moment of such a wall in the  $y$ -direction is equal to  $\delta_w dM_s$ . If the walls approach one another to a distance comparable to the domain wall width, it is to be expected that the wall structure will change. Such wall structures were shown by Kaczér [67] to behave like:

$$m_z(x) = \sin(\theta_0) \operatorname{sn}(\pi x/\delta_w, \sin(\theta_0)) \quad , \quad (4.23)$$

with  $\operatorname{sn}(z, k)$  the Jacobi sine [41]. The value of  $\theta_0$  must be determined numerically from the equation:

$$\lambda_d = 4\delta_w/\pi K(\sin(\theta_0)) \quad , \quad (4.24)$$

with  $\lambda_d$  the domain period and  $K(z)$  the complete elliptic integral of the first kind.

The Bloch wall changes the magnetic surface charges compared to a homogeneously magnetized domain. Therefore, it is necessary to estimate the difference between a binary domain surface charge pattern, as was used for the calibration of the tip, and the real domain pattern. In order to do this, it is assumed that a wall correction can be achieved by multiplying the Fourier transform of the square pattern with the Fourier transform of a wall transfer function. This function is computed by dividing the Fourier transform of equation 4.22 by the Fourier transform of a step-like wall:

$$M_{z,walls}(\mathbf{k}) = \frac{k\delta_w/2}{\sinh(k\delta_w/2)} M_{z,square}(\mathbf{k}) \quad (4.25)$$

This approximation stays valid, as long as the walls are not too curved, and they are so far apart that they do not influence one another. From equation 4.25, one finds that the wavelength where the magnetization of the actual pattern becomes  $\sqrt{2}$  (-3 dB) smaller than that of a square pattern lies at approximately  $2\delta_w$ . For smaller wavelengths, the error in the step-like pattern approximation increases rapidly. Thus, the step-like magnetization pattern approximation used in the calibration procedure becomes doubtful for magnetization wavelengths smaller than 50 nm for the calibration sample containing 10 nm of Ni.

### 4.3 Influence of Surface Anisotropy on the Magnetization Structure in Cu/Ni/Cu Sandwiches

In previous studies on similar samples, the relation between anisotropy and domain size [68] was verified in the range where the effective anisotropy is positive [69, 70].<sup>5</sup> In this thesis, the MFM is used to investigate the behavior of samples containing a 15 and 200 nm thick Ni layer with a negative effective anisotropy. In the analysis of the measurements, the magnitude and the shape of the signal were investigated in addition to the size of the domains, which has become possible due to the advances described in chapter 3.

The sample containing 200 nm of Ni was the first to be studied. From the hysteresis loop, it is found that the in-plane remanent magnetization is  $0.42M_s$ , whereas there is no out-of-plane remanent magnetization (figure 4.6). Thus one might expect to see typical in-plane domains in MFM measurements. However, the MFM measurements on these samples showed a typical domain structure for a sample in which the magnetization is oriented perpendicular to its surface. A relatively regular domain structure could be obtained in the remanent state after applying an in-plane field to the sample of approximately 10 kA/m (figure 4.7a). In this state, the domain walls are found to align with the applied magnetic field. The typical period of the domains,  $\lambda_d$ , was determined to be  $0.23 \mu\text{m}$  from the maximum in the Fourier spectrum of the image. Several models of the structure of the domains were considered, which are shown in figure 4.8. Each of these models will be described in more detail in the following. Finally, a similar analysis will be applied to the sample containing 15 nm of Ni.

---

<sup>5</sup>It is remarkable that good agreement between theory and experiment was found, without taking the  $\mu^*$  effect into account [34, 71]. This effect should have its strongest influence on the domain size for this type of samples, where  $K_2$  and  $K_d$  have a comparable magnitude.



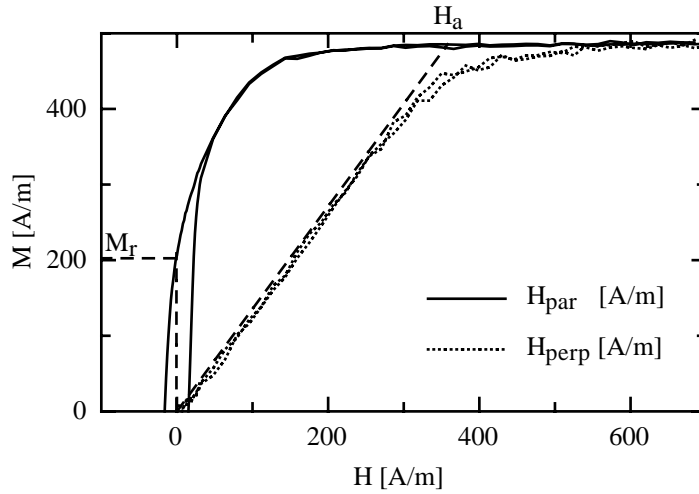


Figure 4.6: Hysteresis loops of the sample containing 200 nm of Ni measured using Vibrating Sample Magnetometry. The magnetization was once measured in the field direction with the field applied perpendicular to the sample plane, and once with the applied field parallel to the sample plane. The anisotropy constant of the sample was determined from the anisotropy field,  $H_a$ :  $K_2^{eff} = \frac{1}{2}\mu_0 M_s H_a$ . The remanent magnetization,  $M_r$ , for the in-plane applied field is  $0.42M_s$ .

#### 4.3.1 Surface Domains

It was first thought that the domain contrast shown in figure 4.7a was due to domains with a magnetization perpendicular to the surface, located at the sample surface. These perpendicular component should decay to an in-plane magnetization with a decay length of approximately  $\sqrt{A/K_d} = 8 \text{ nm}$  [72] (figure 4.8a). The observation of such domains would be a direct proof that the anisotropy of the Cu/Ni interface is positive.

However, quantitative analysis of the magnitude of the MFM signal showed that the the signal of the sample was much too large: The domain pattern was estimated by using a discrimination level, as was used in the calibration method. As a simple model for the magnetization structure of these domains, a homogeneously magnetized surface layer was used. To explain the magnitude of the MFM signal, this layer should be approximately 40 nm thick, which is much thicker than the expected 8 nm. An exponential decay of the perpendicular magnetization would need a decay length of much more than 40 nm to explain the measured signal. Moreover, strain measurements showed that these samples had a higher strain than expected from extrapolating the  $d^{-2/3}$  decay of the strain, determined from the measurements on the thin samples. The measured strain was  $3.2 \cdot 10^{-3}$ , versus a strain of  $0.3 \cdot 10^{-3}$  expected from the fitted power law (see section 4.1.1). This strain in turn gives rise to a considerable volume anisotropy term, compared to the surface anisotropy term ( $K_{me} = 43 \cdot 10^3$  instead of  $4.1 \cdot 10^3 \text{ J/m}^3$ , compared to  $2K_s/d = 7.1 \cdot 10^3 \text{ J/m}^3$ ).

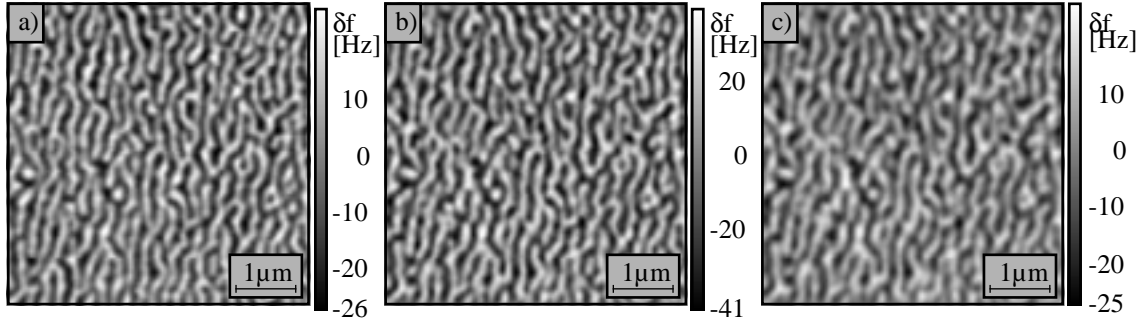


Figure 4.7: Measurement and simulations for different wall profiles.

- a) Measurement of a Cu/200 nm Ni/Cu sample
- b) Simulation, using a magnetization structure with a wall width of 47 nm: the signal shape is correct, but its size is too large
- c) Simulation, using the approximate magnetization structure for wall width of 94 nm: the signal size is correct, but the shape is not.

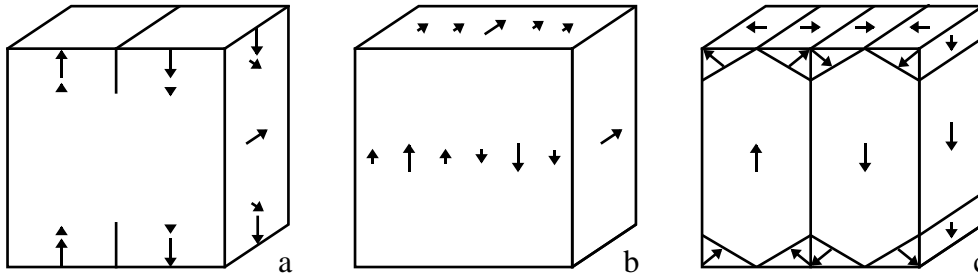


Figure 4.8: Schematic representation of the magnetization structures considered for the Cu/200 nm Ni/Cu sample.

- a) Surface domain structure
- b) Sinusoidally varying magnetization, constant throughout the sample thickness
- c) Canted closure domains

### 4.3.2 Homogeneous Weak Stripes

Due to the large anisotropy, a different magnetization structure of the domains can be expected. In this structure, the sample magnetization is better aligned with the easy axis throughout the sample (figure 4.8b).

An exact solution for the nucleation of such a state was first presented by Muller [73], but described more clearly in paragraph 3.7.2 of the book by Hubert and Schäfer [9].<sup>6</sup> It was shown that a so-called weak stripe pattern will nucleate at zero applied field in a magnetic layer thicker than a certain critical thickness. In case  $K_2 \ll -K_d$ , this critical thickness is twice the Bloch-wall width. As  $K_2$  approaches  $-K_d$ , the critical thickness rapidly decreases to zero. Using the values for the anisotropy and wall width of the layer containing 200 nm Ni, one finds that the weak stripe domains can be

<sup>6</sup>This theory can quite easily be expanded to include the surface domain state, but this was omitted by the authors. It is not presented in this thesis due to the limited amount of available time.

removed by applying an in-plane field larger than 86 kA/m. The predicted period of the nucleated sine-wave magnetization pattern that occurs on reducing the applied field is  $1.25d = 250$  nm, which compares well with the observed domain period, even though the observed domain period was obtained by applying a much smaller field.

However, this nucleation model can not predict the final shape of the formed magnetization structure, because it is based on linearization of the micromagnetic equations. Thus, either the nucleated sinusoidal pattern might simply increase in amplitude after its nucleation, or higher harmonics may appear, to form a “normal” magnetization pattern with domain walls.

To find the magnetization structure, it is assumed that the formed structure is described by equation 4.23. If one uses the wall width  $\delta_w = 47$  nm, a normal domain structure is obtained (solid line in figure 4.9). In order to emulate the influence of the smoothing of the magnetization transitions by the domain walls, the binary domain transition was filtered using a low-pass filter similar to the one given in equation 4.25. Due to the irregularity of the domains, it is somewhat problematic to compare these profiles to the ones calculated for the average domain size using equation 4.23. However, for a section of the measurement where the domain size is equal to the average domain size, the agreement is quite good, as is demonstrated by the squares in figure 4.9. The simulation of the MFM measurements using the magnetization structure with a wall width of 47 nm is shown in figure 4.7b. By comparing the magnitude of the simulated signal to the measured signal, it is found that the simulated signal is too large by a factor 1.6. (Note the difference in the contrast scales for the measured and simulated image.)

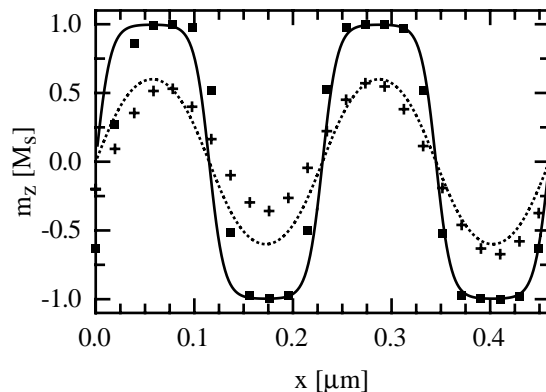


Figure 4.9: Magnetization structure for different wall widths. The solid line shows a simulation with actual wall width  $\delta_w = 47$  nm, the dotted line shows a simulation for a  $\delta_w = 103$  nm. The plotted points are suitable cuts from the magnetization structures used for the simulations of the MFM measurements.

The amplitude of the simulated signal can be decreased by decreasing the magnetization variation. This in turn can be achieved by increasing the wall width. As a rough simulation of the increase of the wall width, the magnetization pattern was smoothed until a 0.6 times smaller amplitude of the signal was obtained (figure 4.7c). By comparing the smoothed magnetization pattern (crosses in figure 4.9), to a pattern predicted

by equation 4.23 (dotted line in figure 4.9), it is found that the wall width should be a factor two larger, to obtain a decrease of the simulated signal by a factor 0.6. This corresponds to a factor four times smaller anisotropy than measured, therefore this magnetization state is unlikely to occur.

The existence of a smooth, sinusoidal-like magnetization pattern can also be excluded by comparing the shape of the simulated signal for this magnetization structure to the shape of the measured signal. By visual comparison of the simulations for the normal and the sinusoidal domain pattern in figure 4.7, one gets the impression that the simulated measurement computed from the sinusoidal structure is too smooth. A more quantitative view is obtained by comparing the behavior of magnitude of the spectral components of these simulated MFM measurements to those of the actual measurement (figure 4.10). The spectral components of the image, simulated with the actual domain wall width shows no significant deviation from the measurement, whereas the spectral components of the image, simulated with the double wall width are a factor 10 smaller for the second harmonic. Thus, from the analysis of behavior of the higher spectral components of the image, the magnetization profile is obtained with the calculated wall width, rather than the double wall width, needed to explain a more sinusoidal pattern.

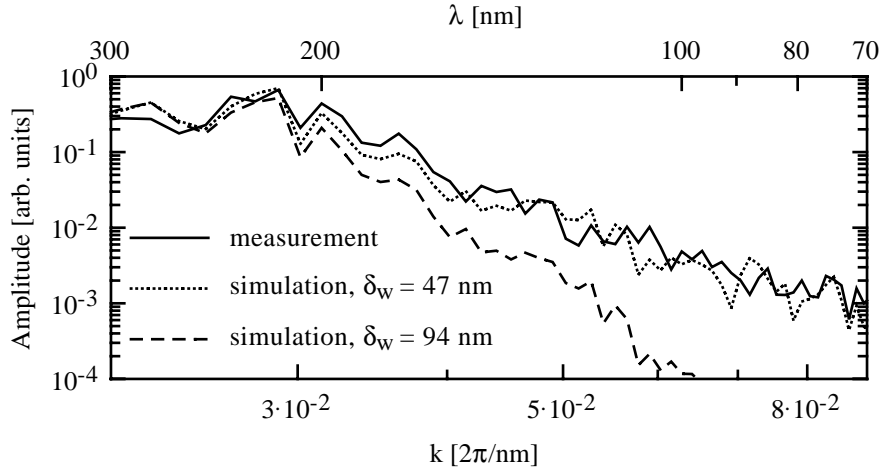


Figure 4.10: Normalized amplitude spectra of simulated measurements for the actual wall width,  $\delta_w$ , and the double wall width, compared to the amplitude spectrum of the measured image.

### 4.3.3 Partial Closure Structure

Because the size and shape of the measured signal can not be explained by the formation of a homogeneous weak stripe structure, it must be assumed that the sample magnetization is inhomogeneous through its thickness. The reduction of the stray field may be due to the formation of so called partial closure domains (figure 4.8c): close to the surface of the sample, the magnetization rotates in a divergence free manner, to increase the angle between the magnetization and the surface normal at the sample surface. Since the magnetization rotates in a divergence-free way, no magnetic charges

are formed inside the layer, and equation 4.15 can still be used if  $M_z$  is decreased to  $M_z \cos(\theta)$ , with  $\theta$  the angle between the magnetization and the surface normal (see also the derivation of the equation in appendix A). To obtain the necessary reduction of the signal by a factor 1.6,  $\theta$  must be  $90 + / - 37^\circ$ . This was also the case for the maximal angle of the sinusoidal pattern, but now the angle inside the film is  $90 + / - 90^\circ$ , and the in-plane magnetization component at the surface lies in a direction perpendicular to the wall, instead of parallel to it.

It is interesting that the remanent in-plane magnetization, determined from the hysteresis loop (figure 4.6) can be explained in this model, even though the schematic representation of the magnetization in figure 4.8c shows no magnetization component parallel to the domain walls. The remanent magnetization could be due to the in-plane magnetization inside the domain wall, which has an average in-plane magnetization of approximately  $M_s 2\delta_w / \lambda_d = 0.41M_s$ . Thus, the direction of the macroscopic magnetic moment of the sample is determined by the direction of the walls between domains, and the dominant direction of the microscopic magnetization of the sample is perpendicular to the direction of the macroscopic magnetic moment of the sample.

#### 4.3.4 Domains in 15 nm Ni Samples

A similar analysis of measurements on the sample containing 15 nm of Ni was attempted. According to equations 4.12 and 4.13, surface domains may nucleate, even for infinitely extended domain sizes. Besides this, the layer thickness is much smaller than the 26 nm wall width, therefore the canted closure state can (probably) be excluded. However, an additional state may be possible, if one believes that the cone states, mentioned in section 4.1.2 exist. In this state, domains may form in which the angle with the surface normal takes the values  $90 + / - 34^\circ$ .<sup>7</sup>

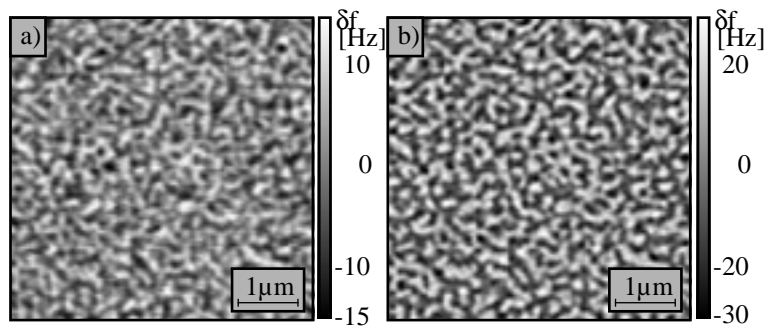


Figure 4.11: Domain structure of a Cu/15 nm Ni/Cu sample.

- a) MFM measurement. Note that the noise is much larger than the thermal noise limit, indicating that modification of the sample occurs.
- b) Simulation, using a magnetization structure with a wall width of 26 nm. The size of the measured signal is approximately a factor 2 smaller, and its shape is not reproduced very well.

<sup>7</sup>Strictly speaking, the expressions for the domain wall width, derived in section 4.2.2 can not be applied if the measured values of  $K_4$  are correct. It is possible to calculate the structure and energy of such a wall [9], but this was not pursued here.

The evaluation of the measurements on these samples however, is more difficult due to the poor signal-to-noise ratio of the measurements (figure 4.11a). Clearly, the magnitude of the noise is much larger than the thermal noise (0.4 Hz, see section 2.3). A possible source for the noise could be modification of the sample magnetization. A simulated measurement was calculated from the measured magnetization pattern (figure 4.11b). The correspondence between the measurement and the simulation is rather poor, which could be due to the modification of the sample by the tip. Nevertheless, it is clear that the signal is smaller than can be expected for a layer that is homogeneously magnetized perpendicular to its surface. However, it is even more difficult to decide what the domain structure is, because no analysis of the shape of the measured signal is possible in this case.

## Chapter 5

# MFM on Superconductors, Applied to YBCO Samples

When superconductivity was discovered by Kamerlingh–Onnes, it was through the experimental observation that the resistivity of certain materials disappeared below a certain critical temperature  $T_c$ . After this discovery, it took approximately twenty years before Meissner and Oxenfeld discovered that applied fields smaller than a critical field  $H_c(T/T_c)$  are expelled from the inside of the superconductor, resulting in a repulsive magnetic interaction. When the local field, given by the sum of the applied field and the field due to the Meissner expulsion is larger than the critical field, the field can penetrate the superconductor locally, and normal conducting regions are formed. The behavior of these coexisting regions are described by the Ginsburg–Landau equations, using a complex order parameter  $\psi$ :

$$\left(i\nabla + 2\pi\frac{\mathbf{A}}{\phi_0}\right)^2\psi = \frac{1}{\xi^2}(\psi - |\psi|^2\psi), \quad (5.1)$$

$$\nabla^2\mathbf{A} = \frac{1}{\lambda^2}\left(|\psi|^2\mathbf{A} + i\frac{\phi_0}{4\pi}(\psi^*\nabla\psi - \psi\nabla\psi^*)\right), \quad (5.2)$$

with  $\phi_0$  the superconducting flux quantum,  $\mathbf{A}$  the magnetic vector potential and  $|\psi|$  the density of superconducting particles. The parameter  $\xi$  is called the Ginsburg–Landau coherence length, and is a characteristic length over which the order parameter changes in size. The parameter  $\lambda$  is called the penetration depth, and is a characteristic length over which the vector potential, and thereby the magnetic field can vary inside the superconductor. It was found that, although  $\xi$  and  $\lambda$  vary as a function of temperature, their ratio, called the Ginsburg–Landau parameter,  $\kappa \equiv \lambda/\xi$ , is approximately constant. Furthermore, in the limit  $\kappa \rightarrow \infty$ ,  $|\psi|$  is constant, and the second Ginsburg–Landau equation reduces to the simpler equation found previously by F. and H. London. F. London also found that the fluxoid is quantized, where the fluxoid  $\phi'$  is defined as:

$$\phi' = \frac{\mu_0}{\lambda^2} \oint_l \mathbf{j} d\mathbf{l} + \int_S \mathbf{B} d\mathbf{s} = n \frac{h}{2e}, \quad (5.3)$$

with  $\mathbf{B}$  the magnetic flux density,  $h$  Plancks constant,  $e$  the electron charge,  $\mathbf{j}$  the current density vector, and  $l$  a closed path inside the superconductor that encloses the

surface  $S$ . In the case the integral of the current is zero, the total amount of magnetic flux is quantized with increments of  $\phi_0 = \frac{h}{2e}$ <sup>1</sup>. Abrikosov found that a magnetic domain structure is only occurs in superconductors with  $\kappa < 1/\sqrt{2}$ . These superconductors are called type-I superconductors. However, for superconductors with  $\kappa < 1/\sqrt{2}$ , the energy of the domain walls becomes negative between the external fields  $H_{c1}$  and  $H_{c2}$ . This leads to the formation of a structure of screening current vortices around small, normal conducting cores, with each vortex containing one flux quant. The superconductors where this occurs are called type-II superconductors. These superconductors generally have a higher critical temperature and field, and are therefore interesting for technical applications. The interest in this type of superconductors revived due to the discovery of the group of so called High- $T_c$  superconducting materials by Bednorz and Müller [74], some of which have a critical temperature above the boiling point of liquid nitrogen.

Material	Nb	NbSe <sub>2</sub>	YBa <sub>2</sub> Cu <sub>3</sub> O <sub>7-x</sub>
$\lambda$ [nm]	32	200	140
$\xi$ [nm]	39	7.7	1.4

Table 5.1:  $\lambda$  and  $\xi$  for different superconducting materials.

Using the low temperature MFM, both the Meissner forces due to the screening of the tip field from the inside of the superconductor and the forces due to the stray field of the vortex structures in the superconductor can be measured. The contrast formation process on the superconductors will be investigated in more detail in section 5.1. The results of this investigation are used in section 5.2 to estimate what information can be extracted from the MFM measurements by the evaluation of the image contrast in older measurements.

## 5.1 Contrast Formation on Superconductors

In previous work, all types of MFM contrast formation, as described in chapter 3 have been investigated theoretically: negligible modification [75, 76], reversible modification [35, 76, 77], and irreversible modification [78]. However, due to the lack of experimental data on the tip structure, this work has mainly focussed on the image formation process in the case of simple model tips, such as monopoles and dipoles. In the following, the contrast formation models for negligible and for reversible sample modification are discussed. Furthermore, the applicability of these models is expanded to include both realistic tip models and the influence of the finite thickness of the superconducting layer.

As was the case for ferromagnets, the imaging mechanism is fully understood when the stray field of the superconducting sample, and the stray field of the tip are known. One source of the sample stray field is the field generated by the current distribution, that in turn is caused by the Meissner expulsion of the tip field. This leads to a type of contrast formation that is due reversible modification of the sample stray field, that is discussed in section 5.1.1. A second source of the sample stray field is the presence of

<sup>1</sup>Actually London found  $\phi_0 = \frac{h}{e}$ , later it was shown in the BCS-theory that the superconducting current is carried by pairs of electrons, so-called Cooper pairs, with charge  $2e$ .



a vortex. When the MFM tip does not modify the vortex–core, the contrast formation can be explained using negligible modification of the sample, as shown in section 5.1.2. A third source of stray field are normal–conducting domains in type–I superconductors. However, the imaging of these domains by MFM has not been considered yet, which is partly due to the fact that our instrument could not (conveniently) reach temperatures below the critical temperature of these superconductors. Lead, that has one of the highest  $T_c$ 's of the type–I superconductors, has a critical temperature of 7.2 K.

### 5.1.1 Stray Field due to Meissner Expulsion

The field due to the Meissner expulsion of the tip can be modeled in the London limit, as long as  $\kappa \gg 1/\sqrt{2}$  and the field of the MFM tip at the surface of the superconductor is much smaller than the critical field of the superconductor. Hug et al.[35] derived the force for a point monopole tip, whilst Coffey [76] found the force on a tip with rotational symmetry, and derived a closed form expression for the point monopole tip. Here, the approach in [79, 77] is extended to include a calibrated MFM tip, and the flux repulsion for a thin superconducting film is derived.

In the following, our discussion is limited a superconductor that carries no external currents, and without changing electric fields. In the London limit, the  $z$ –component of the magnetic field  $H_1$  outside, and the field  $H_2$  inside a homogeneous superconductor is determined by the differential equations:

$$\begin{aligned}\nabla^2 H_1 &= 0 \\ \nabla^2 H_2 &= \frac{H_2}{\lambda^2} \quad ,\end{aligned}\tag{5.4}$$

with the boundary conditions  $H_1 = H_2$  and  $H_1' = H_2'$ , where the  $'$  designates the partial derivative with respect to  $z$ . In 2-D Fourier space, these equations can be rewritten using the relation  $\partial^2 H(x, y, z)/\partial x^2 + \partial^2 H(x, y, z)/\partial y^2 \rightarrow (k_x^2 + k_y^2)H(\mathbf{k}, z) = k^2 H(\mathbf{k}, z)$ , which was also used in section 3.2.1:

$$\begin{aligned}H_1''(\mathbf{k}, z) &= k^2 H_1(\mathbf{k}, z) \\ H_2''(\mathbf{k}, z) &= (k^2 + 1/\lambda^2)H_2(\mathbf{k}, z) \quad ,\end{aligned}\tag{5.5}$$

and one finds the general solution:

$$\begin{aligned}H_1(\mathbf{k}, z) &= H_{1\downarrow}(\mathbf{k})e^{z k} + H_{1\uparrow}(\mathbf{k})e^{-z k} \\ H_2(\mathbf{k}, z) &= H_{2\downarrow}(\mathbf{k})e^{z\sqrt{k^2+1/\lambda^2}} + H_{2\uparrow}(\mathbf{k})e^{-z\sqrt{k^2+1/\lambda^2}} \quad ,\end{aligned}\tag{5.6}$$

with the boundary conditions:  $H_{1\downarrow} + H_{1\uparrow} = H_{2\downarrow} + H_{2\uparrow}$  and  $H_{1\downarrow}' + H_{1\uparrow}' = H_{2\downarrow}' + H_{2\uparrow}'$ .

As was pointed out by Coffey [79], this description is analogous to the description of non-relativistic quantum mechanics by the Schrödinger equation, or the description of the propagation of evanescent plane electromagnetic waves with normal incidence to a surface. In the latter case, both the transversal components of the B– and the E–fields are continuous at the interface, whereas here the H– and the H'–fields are continuous. Analogous to the optical case, one can define a reflection coefficient for the reflection at a single surface:  $r_1 \equiv H_{1\uparrow}/H_{1\downarrow}$ <sup>2</sup> and a transmission coefficient  $t_1 \equiv H_{2\downarrow}/H_{1\downarrow} = 1 + r_1$ .

---

<sup>2</sup>Coffey uses a slightly different definition of the reflection coefficient:  $r_{\text{Coffey}} = -r$ .

Solving the boundary conditions using the definition of the reflection coefficient and equations 5.6, one finds that the reflection coefficient is given by:

$$r_1 = \frac{k - \sqrt{k^2 + 1/\lambda^2}}{k + \sqrt{k^2 + 1/\lambda^2}}, \quad (5.7)$$

Furthermore, a propagation coefficient  $p$  can be used that describes the propagation of the magnetic field as a function of  $z$ .<sup>3</sup> If a tip-equivalent surface charge distribution  $\sigma_{tip}(\mathbf{k})$  (see section 3.2.2) is located at a distance  $z$  from the superconductor then  $H_{1\downarrow}(\mathbf{k}) = e^{-z k} \sigma_{tip}(\mathbf{k})$ , as is shown schematically in figure 5.1a. In this case, the field

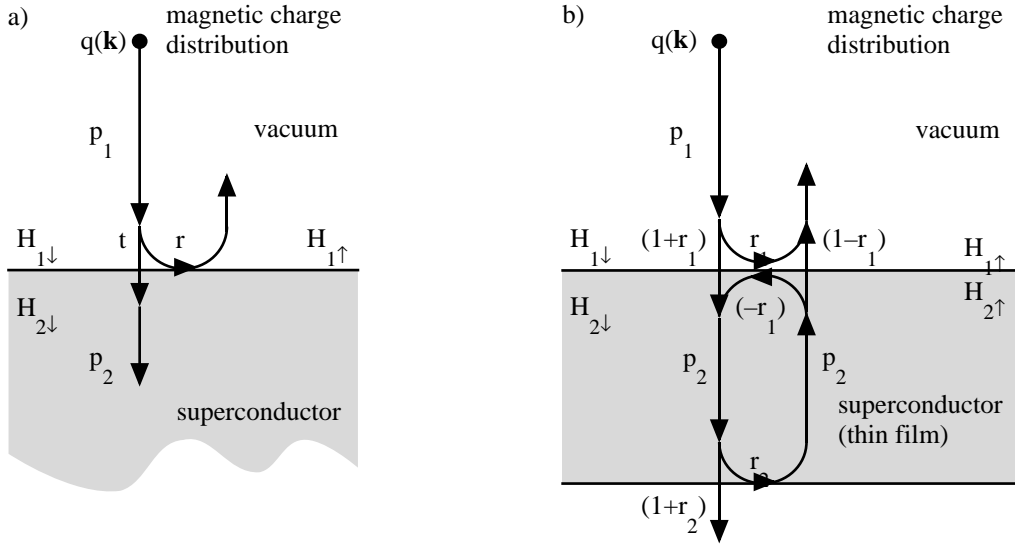


Figure 5.1: Schematic representation of the calculation of the Meissner repulsion of the tip-field

- a) for an infinite superconductor
- b) for a superconducting layer.

reflected by the superconductor,  $H_{refl}$ , at the location of the tip equivalent charge is given by:

$$\begin{aligned} H_{refl}(\mathbf{k}, z) &= -1/2 \sigma_{tip}(\mathbf{k}) p_1^2(z) r(\mathbf{k}) \\ r(\mathbf{k}) &= r_1, \quad p_1(z) = e^{-z k}, \end{aligned} \quad (5.8)$$

The transmitted part of the field in the inside the superconductor at a depth  $z'$  is given by:

$$\begin{aligned} H_{trans}(\mathbf{k}, z, z') &= -1/2 \sigma_{tip}(\mathbf{k}) p_1(z) t(\mathbf{k}) p_2(z') \\ t(\mathbf{k}) &= (1 + r_1), \quad p_2(z') = e^{-z' \sqrt{k^2 + 1/\lambda^2}}, \end{aligned} \quad (5.9)$$

<sup>3</sup>Coffey showed that, even for an inhomogeneous superconductor, where the penetration depth depends on  $z$ ,  $\lambda(z)$  can in principle be determined through the  $k$ -dependence of the reflection coefficient, which can be estimated from measured force-distance curves [77, 79].

For a thin superconducting layer one must take multiple reflections into account, as is shown schematically in figure 5.1b. One finds:

$$\begin{aligned} H_{1\uparrow} &= r_1 H_{1\downarrow} + (1 - r_1) H_{2\uparrow} \\ H_{2\downarrow} &= (1 + r_1) H_{1\downarrow} - r_1 H_{2\uparrow} \\ H_{2\uparrow} &= p_2 r_2 p_2 H_{2\downarrow} \quad , \end{aligned}$$

with  $p_2 = e^{-d\sqrt{k^2+1/\lambda^2}}$ , and  $d$  the thickness of the superconducting layer. The solution is given by:

$$r = H_{1\uparrow}/H_{1\downarrow} = \frac{r_1 + r_2 p_2^2}{1 + r_1 r_2 p_2^2} \quad (5.10)$$

$$= r_1 \frac{1 - p_2^2}{1 - r_1^2 p_2^2} \quad , \quad (5.11)$$

$$t = p_2 \frac{1 - r_1^2}{1 - p_2^2 r_1^2} \quad , \quad (5.12)$$

using  $r_2 = -r_1$ . As is the case for optics, the reflection coefficient for the surface of a sample consisting of any number of layers can be calculated by the recursive application of equation 5.10, starting with the interface that is furthest away from the surface of the superconductor, by inserting the reflection coefficient of the lower layer stack for  $r_2$ .

Using the calculated field, the force,  $F_n$ , acting on the MFM lever can be calculated in Fourier space using equation 3.13. The difference between the negligible modification case and the (homogeneous) reversible modification case lies in the fact that the screening current moves with the tip when it moves laterally. This makes the interaction constant as a function of lateral position, and equal to the force at the position  $x = 0, y = 0$  in the negligible modification case. Evaluating the inverse Fourier transform for  $x = 0, y = 0$  one finds:

$$F_n = \frac{\mu_0 \cos(\theta)}{4\pi^2} \int_{-\infty}^{\infty} -1/2 \sigma_{tip}(\mathbf{k}) p_1^2(z) r(\mathbf{k}) \sigma_{tip}^*(\mathbf{k}) d\mathbf{k} \quad , \quad (5.13)$$

with  $\theta$  the canting angle between the lever normal and the sample surface normal, as was shown in fig. 2.1. Inserting  $r$  from equation 5.8 one finds the force caused by the flux expulsion from a semi-infinite sample:

$$F_n = \frac{\mu_0 \cos(\theta)}{8\pi^2} \int_{-\infty}^{\infty} |\sigma_{tip}(\mathbf{k})|^2 \frac{\sqrt{k^2 + 1/\lambda^2} - k}{\sqrt{k^2 + 1/\lambda^2} + k} e^{-2kz} d\mathbf{k} \quad . \quad (5.14)$$

Inserting  $\theta = 0$ ,  $\sigma_{tip}(\mathbf{k}) = q_0$ , and transforming to polar coordinates, equation 5.13 can be reformed to equation 13 in [35] (note that the unit of  $q$  is [Wb] in [35], whereas it is [Am] here). In the case  $1/k \gg \lambda$ , the equation reduces to the complete flux expulsion model, where the tip “feels” its mirror image at a distance  $2z$ . For  $1/k \ll \lambda$  the force becomes zero. Therefore, magnitude of the penetration depth dependent part of the force is determined by the magnitude of the tip stray-field components with a

wavelength comparable to  $\lambda$ . These stray field components do not reach the sample at tip-sample distances much larger than  $\lambda$ , therefore the approach curve should be approximately equal to that of the complete flux expulsion model at large distances.

In contrast to the field distribution of a theoretical tip model, the field distribution of a real MFM tip can not be scaled by  $\lambda$ , therefore the behavior of the force, or force derivative as a function of distance must be calculated for each specific tip. This calculation is demonstrated for the microfabricated Si-tip of which the stray field was determined in section 3.3.2. For comparison to the measurements, not the force, but the frequency shift was calculated as a function of tip-sample distance using equation 2.5 and the lever properties listed in table 2.1. It is noteworthy that all Fourier components must be multiplied with  $2k$  instead of  $k$  to calculate the force derivative from the force. This is due to the interaction between the tip and the sample. In figure 5.2, results are shown of calculations for a semi-infinite superconductor and a thin-film superconductor.

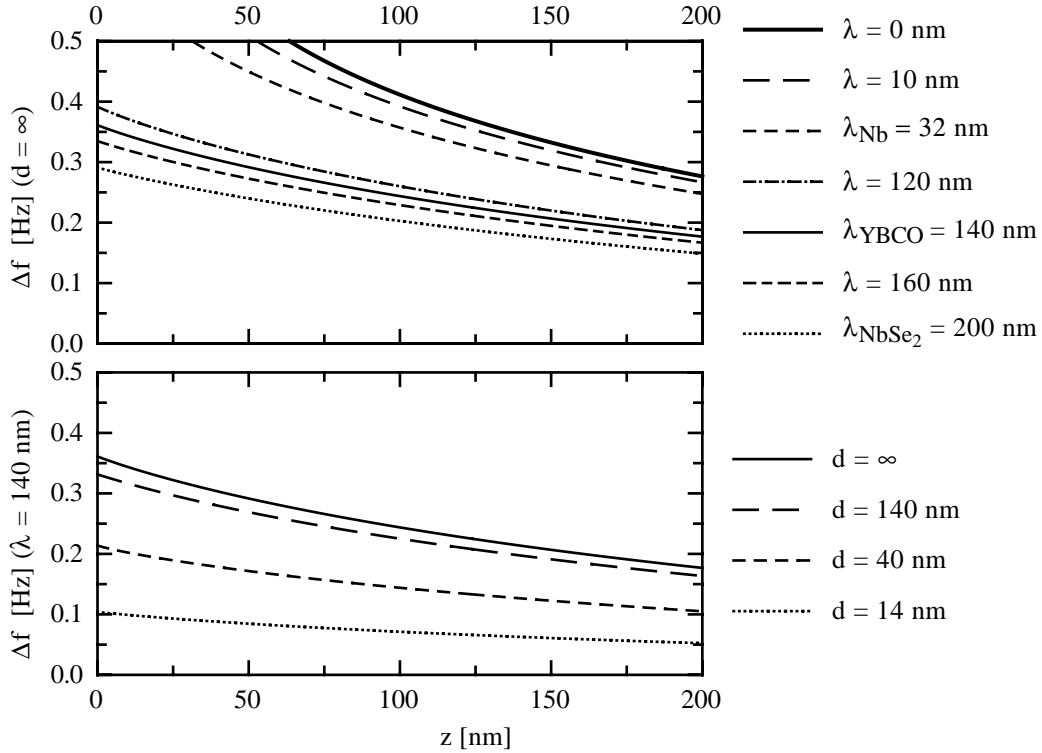


Figure 5.2: Calculated frequency shift versus distance due to the Meissner Force. Upper figure: frequency shift for several values of  $\lambda$  on an infinite sample. Lower figure: frequency shift as a function of sample thickness  $h$  for a sample with the penetration depth of YBCO,  $\lambda_{\text{YBCO}} = 140$  nm.

It is clear that changes in the penetration depth of a semi-infinite superconductor can be measured more accurately for small penetration depths. For YBCO samples ( $\lambda = 140$  nm), a change in the penetration depth in the order of 20 nm should be detectable in measurements with a small bandwidth, provided the Meissner force can be separated

from other forces, such as electrostatic and Van-der-Waals forces. The accuracy of absolute measurements of  $\lambda$  is determined by the accuracy of the tip-calibration, and should lie in the order of 10 %. The effect of the finite film thickness becomes noticeable when the film thickness decreases below  $\lambda$ .

### 5.1.2 The Vortex Stray Field

If vortices are formed in a type-II superconductor, the expression for the field inside the superconductor in equation 5.4 must be modified in order to include the core of the vortex:

$$\nabla^2 H_2 = \frac{H_2}{\lambda^2} + V(x, y) \quad , \quad (5.15)$$

where  $V(x, y)$  is the ‘vorticity’ of the vortex, which can not be calculated from the London model, but must be determined from the Ginsburg-Landau equations. The field of a vortex can be calculated similar to the flux repulsion of the MFM tip, as was shown by Coffey and Phipps [80].

A particular solution for the vortex-field equation 5.15,  $M_v(\mathbf{k})$ , is:

$$M_v(\mathbf{k}) = -\frac{V(\mathbf{k})}{k^2 + 1/\lambda^2} \quad , \quad (5.16)$$

which can be interpreted as the magnetization of the vortex core. The magnetic moment of the sample is given by the integral of the magnetization of the vortex cores and the magnetization due to the Meissner expulsion of the externally applied field. Note that the homogeneous magnetization due to the Meissner expulsion of the external field will not give a contribution to the contrast, as long as the measurement is not too close to the sample edge, as was already pointed out in section 4.2.1. Furthermore, the vortex structures imaged in this thesis were obtained by cooling the sample from above  $T_c$  to below  $T_c$  in the presence of an applied field. In these samples no Meissner expulsion of the applied field occurs, because the zero internal field is achieved by ‘transporting’ the external field through the superconducting layer in the form of vortices. Therefore, the number of vortices is proportional to the external field:  $n_{vortex} = \mu_0 H_{ext}/\phi_0$ .

Like the ferromagnetic samples in section 4.2.1, the magnetization of the vortex core has a stray field, which is repelled by the superconductor similar to the stray field of the MFM tip. For a vortex in a semi-infinite superconductor, the field outside the superconductor is given by the sum of the stray field of the vortex core and the stray field that is expelled by the superconductor:

$$H_v(\mathbf{k}, z) = 1/2 M_v(\mathbf{k}) p_1(z) (1 - r_1) \quad , \quad (5.17)$$

with  $p_1(z)$  and  $r_1$  as defined in section 5.1.1. For a thin film superconductor, the vortex stray field is given by:

$$\begin{aligned} H_v(\mathbf{k}, z) &= 1/2 M_v(\mathbf{k}) p_1(z) (1 - r - t) \\ &= 1/2 M_v(\mathbf{k}) \frac{(1 - r_1)(1 - p_2)}{1 + p_2 r_1} \\ &= M_v(\mathbf{k}) \frac{1}{1 + k/\sqrt{k^2 + 1/\lambda^2} \coth(d/2\sqrt{k^2 + 1/\lambda^2})} \quad , \quad (5.18) \end{aligned}$$

with  $t, r, p_1$  and  $p_2$  the same as for the flux repulsion from a thin superconducting layer. In addition to the terms that were also needed to calculate the Meissner expulsion, the  $t$  term is needed here to calculate the total field, because the effect of the field transmitted from the lower end of the vortex through the superconductor must be taken into account.

Fritz [75] calculated the stray field produced by an isolated vortex in an semi-infinite superconductor as a function of the anisotropy of the superconductor between the ab- and c-directions, and the Ginsburg-Landau parameter  $\kappa$ . As a side result, a simple approximation for the vortex structure was found. In this approximation, the influence of the coherence length on the vortex structure is modeled using the Ginsburg-Landau theory, as done by Clem [81, 82, 83] for an infinite superconductor. Additionally, the widening of the vortex close to the superconductor surface, located in the xy-plane, is modeled in the London limit ( $\kappa \rightarrow \infty$ ). Ignoring the anisotropy of the superconductor, the result by Fritz can be obtained using Clem's solution of the vortex field as  $\mathbf{M}_v(\mathbf{k})$ :

$$M_v(\mathbf{k}) = \frac{\phi_0}{\lambda \mu_0 K_1(\xi_v/\lambda)} \frac{K_1(\xi_v \sqrt{k^2 + 1/\lambda^2})}{\sqrt{k^2 + 1/\lambda^2}} \quad , \quad (5.19)$$

where  $K_1$  is the first order modified Bessel function of the second kind and  $\xi_v$  is a variational parameter for the radius of the normal conducting core. For small values of  $\xi$ ,  $\xi_v$  is found to be equal to  $\sqrt{2}\xi$  (see figure 1 in [75]). Inserting equation 5.19 into equation 5.18, the vortex field is found:<sup>4</sup>

$$H_v(\mathbf{k}, z) = \frac{\phi_0}{\lambda \mu_0 K_1(\xi_v/\lambda)} \frac{K_1(\xi_v \sqrt{k^2 + 1/\lambda^2})}{\sqrt{k^2 + 1/\lambda^2} + k \coth(d/2 \sqrt{k^2 + 1/\lambda^2})} e^{-kz} \quad . \quad (5.20)$$

For  $\kappa \rightarrow \infty$ , equation 5.20 becomes the solution found by Chang *et al.* and Irz *et al.* [84, 85], and with the additional limit  $d \rightarrow \infty$ , it becomes the solution found by Pearl [86] for a superconductor with an infinitely small core. The vortex field given by equation 5.20 is plotted in direct space in figure 5.3 for three different superconductors, Nb, NbSe<sub>2</sub> and YBa<sub>2</sub>Cu<sub>3</sub>O<sub>7-x</sub>. The flux density in Tesla is plotted as a function of the distance from the vortex center in panel a, the field normalized for the maximum flux density is plotted as a function of the radial distance normalized for  $\lambda$  in panel b .

To describe the behavior of the vortex field close to the center of the vortex, the vortex radius can be defined as the distance at which the field decays to a fraction  $1/e$  of the maximum field value. This radius is indicated by the square symbols in figure 5.3. The vortex radius according to this definition is slightly larger than the penetration depth for Nb, but about 4 times smaller than the penetration depth in the case of YBa<sub>2</sub>Cu<sub>3</sub>O<sub>7-x</sub>.

A problem of this definition is that it does not do justice to the long range behavior of the vortex, and that it goes to zero for the Pearl vortex model, due to the (unphysical) fact that the flux density goes to infinity at the center of the vortex in this model. To circumvent these problems, an alternative definition of the radius is proposed that uses

---

<sup>4</sup>The difference with Fritz' result is due to the different coordinate system used to describe the field.

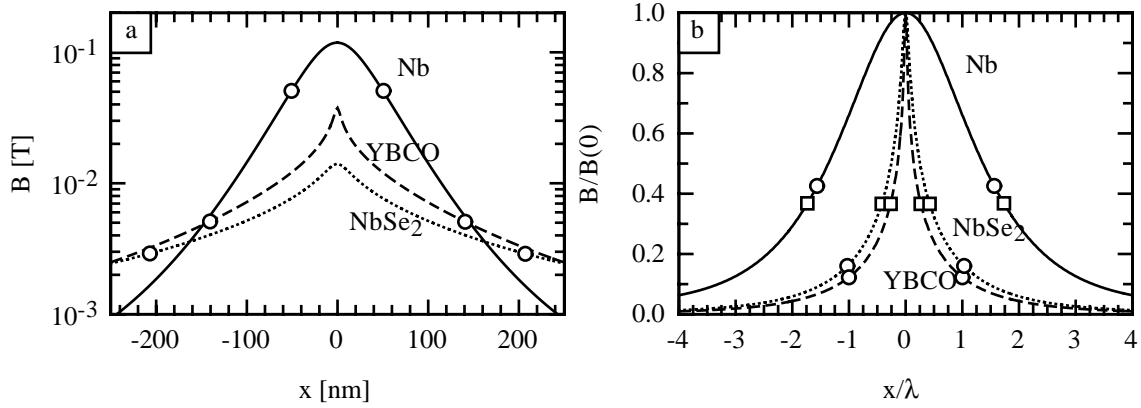


Figure 5.3:  $t$ -component of the flux density distribution of a vortex at the surface of a semi-infinite superconductor ( $z = 0$ ) for three different superconductors: Nb (solid line), NbSe<sub>2</sub> (dotted line) and YBa<sub>2</sub>Cu<sub>3</sub>O<sub>7-x</sub> (dashed line). The squares indicate the position of the  $1/e$  vortex radius, whereas the circles are plotted at the position of the weighed average vortex radius according to equation 5.21).

a) Flux density versus distance

b) Flux density, normalized for maximum density versus distance normalized by  $\lambda$

the weighed average vortex radius,  $\lambda_v$ :

$$\lambda_v \equiv \frac{2\pi \int_0^{\infty} r B_z(r) dr}{2\pi \int_0^{\infty} B_z(r) dr} . \quad (5.21)$$

The numerator in equation 5.21 is equal to  $\phi_0$  for a radially symmetric vortex, and the denominator can be evaluated using the previously obtained results using a coordinate a transform to spherical coordinates:

$$\begin{aligned} B_z(r) &= \frac{1}{2\pi} \int_0^{\infty} B_z(k) k J_0(k r) dk \\ 2\pi \int_0^{\infty} B_z(r) dr &= \int_0^{\infty} B_z(k) \int_0^{\infty} k J_0(k r) dr dk \\ &= \int_0^{\infty} B_z(k) dk , \end{aligned} \quad (5.22)$$

where  $J_0$  is the zeroth order Bessel function of the first kind. Analytical results are obtained for Pearls vortex in a semi-infinite superconductor: Deep inside the superconductor, one finds  $\lambda_v = 2\lambda/\pi$ , whereas at the surface of the superconductor  $\lambda_v = \lambda$ . For more complicated cases, equation 5.21 must be evaluated numerically. In figure 5.4 the magnetic vortex radius at the surface of the superconductor is plotted as a function of  $\kappa$  and layer thickness, obtained using equation 5.20. The weighed average radius is

approximately equal to one for layers thicker than  $1/3 \lambda$  and  $\kappa$  values larger than 10. Some caution must be used when interpreting the plotted results, because the following points were neglected in the derivation of 5.20:

1. The anisotropy of the superconductor. However, for the materials discussed here the anisotropy is quite small. Probably, the approach used here can be expanded to describe anisotropic superconductors.
2. Due to the use of the London limit in the derivation of equation 5.20, the widening of the magnetic radius of the vortex at the surface is not accompanied by a widening of the vortex core. As discussed in [75], this is approximately correct for high  $\kappa$ -values. For  $\kappa$ -values below 10,  $\psi_{vortex}(r, z)$ , widens by more than 40% close to the surface, which will lead to an additional increase of the vortex radius.

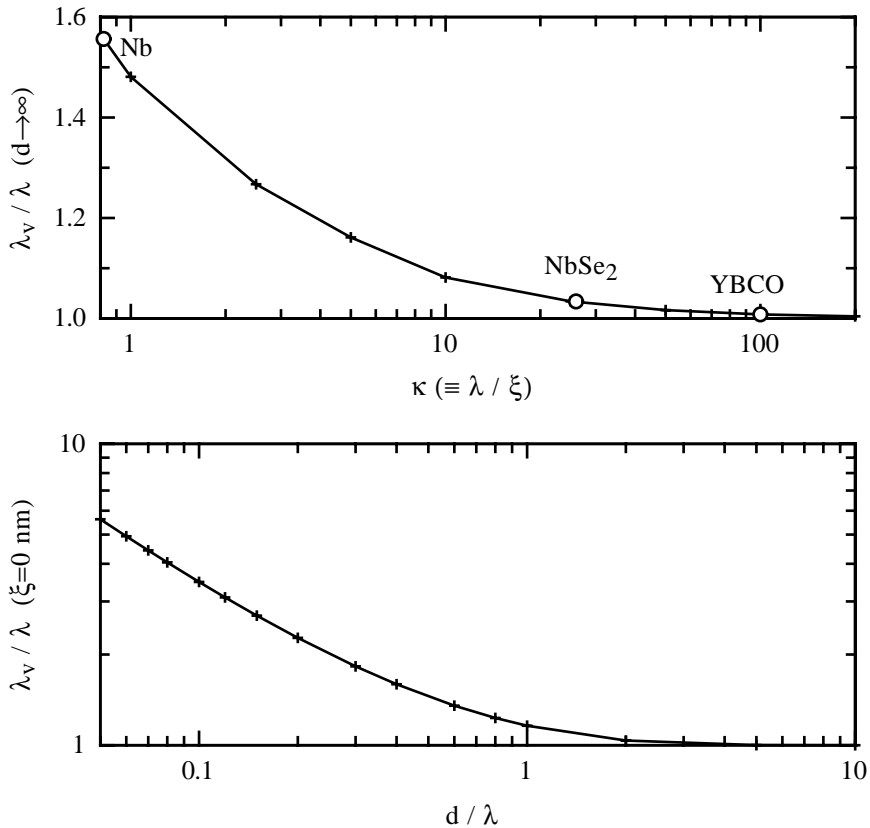


Figure 5.4: Behavior of the vortex radius.

Upper figure: radius of a vortex in a semi-infinite superconductor as a function of  $\kappa$ . The vortex radii for different superconducting materials are indicated by the circles. Lower figure: Dependence of the vortex radius on layer thickness in a superconductor with  $\xi \rightarrow 0$ . The vortex radius increases significantly for layer thicknesses below  $1/3 \lambda$ .



## 5.2 Evaluation of the Experimental Image Contrast

Because the method for quantitative evaluation of MFM measurements was developed more or less simultaneously with the possibility to perform measurements on superconductors, all measurements up to now were made with uncalibrated tips. Due to instrumental problems it was not possible to perform any new measurements, therefore the measurements that were published previously in Bruno Stiefel's thesis [10] are used. However, even from these uncalibrated measurements, some conclusions can be drawn.

### 5.2.1 Cause of the Vortex Contrast

As a first application of the contrast formation theory, the cause of the contrast formation mechanism in vortex imaging can be investigated. In the London limit, the contrast due to the Meissner screening and the contrast due to the vortex stray field are superimposed. One could suppose that the contrast formation of the vortex is mainly caused by the decrease in the Meissner repulsion of the tip, due to the change of the screening current distribution around the vortex core. In this case, the repulsive interaction between the tip and sample should decrease close to the vortex core, independent of the direction of the applied field that was used to create the vortex. On the other hand, if the contrast formation is mainly caused by the interaction between the tip and the stray field of the vortex, the interaction over the vortex is attractive when the vortices are generated by a field parallel to the tip magnetization, whereas it is repulsive when the vortices are generated by a field anti-parallel to the tip magnetization. To test which of the contrast mechanisms is dominant, an experiment was performed on a sample consisting of an approximately 140 nm thick  $\text{YBa}_2\text{Cu}_3\text{O}_{7-x}$  layer on a (100)  $\text{SrTiO}_3$  substrate, produced by laser ablation in the group of Dr. B. Dam [87]. As is shown in figure 5.5, the MFM measurements made of vortex structures produced by an external field anti-parallel and parallel to the tip magnetization clearly show that the interaction of the MFM tip with the stray field of the vortices is the dominant contrast mechanism.

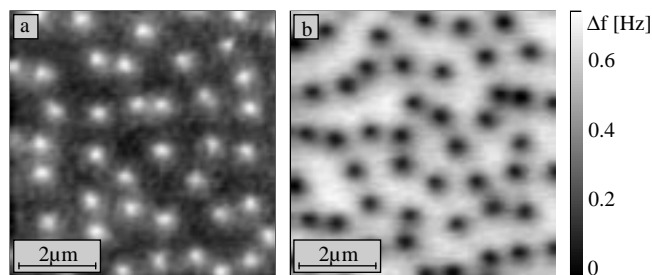


Figure 5.5: MFM images at a single location of the magnetic stray field of a 140 nm thick  $\text{YBa}_2\text{Cu}_3\text{O}_{7-x}$  layer. The sample was field cooled in an external field,  $B_{ext}$ , oriented perpendicular to the thin film plane (i.e. parallel to the  $c$ -axis of the  $\text{YBa}_2\text{Cu}_3\text{O}_{7-x}$  structure). The magnitude of  $B_{ext}$  was equal for both images (2 mT), but its direction was anti-parallel to the magnetization direction of the MFM-tip in Fig. 5.5a and parallel in Fig. 5.5b.

To estimate whether the contrast due to a change in the Meissner force in the

neighborhood of the vortex can be neglected or not, the theory described in the previous section can be used. To find the order of magnitude of the contrast, it is assumed that the effect of the vortex core is approximately equal to that of a hole with a diameter of the vortex radius. The maximum decrease of the Meissner repulsion, occurring above the center of the hole, is probably smaller than the decrease of the repulsion due to an increase of the effective distance between the tip and the superconductor by the radius of the hole. The calculated frequency shift versus distance curves in figure 5.2 can be used to estimate the distance dependence of the tip repulsion,  $F_z$ , because the tip used to produce the measurements shown in figure 5.5 was prepared similar to the calibrated tip. From the slope of the curve calculated a 140 nm thick YBCO layer, one finds that a change in the effective distance by 2 nm would give a signal smaller than  $3 \mu\text{Hz}$ . This is well below the noise level in the measurement of approximately  $50 \mu\text{Hz}$ , therefore it can be concluded that the measurement contrast is entirely due to the stray field of the vortices.

In principle, the test of the exponential decay of the measured interaction that was described in section 3.2.5 can be used to check whether part of the contrast formation is due to some other form of reversible, or irreversible interaction such as a movement or bending of the vortex core in the direction of the scanning MFM tip, but such measurements were not performed yet.

## 5.2.2 Dependence of the Contrast on $\lambda$ and $\xi$

To find how sensitive the measured contrast is to changes in the superconducting properties  $\lambda$  and  $\xi$ , the measured contrast can be compared to the contrast calculated for several parameter values, assuming that the sample magnetization is negligibly modified by the tip. The measurement was made under the same condition as the measurement in figure 5.5a, but with a reduced the scan range. An section of the measurement was used in which the vortex is exactly in the center of the image (figure 5.6a).

The calculation of the tip-sample interaction is more complicated in this case, because the tip calibration used to calculate the Meissner force versus distance curves can not be used here. This is due to the problem that the tip is only calibrated for those spatial frequencies that are contained in the calibration measurements. The size of the calibration measurements was  $5 \mu\text{m}$ , whereas the size of the measurement in figure 5.6a was only  $0.75 \mu\text{m}$ , therefore these measurements contain a different spatial frequency range. As an alternative for a calibrated tip, the calibration was estimated using the calibration function of the geometry based tip model in paragraph 3.4.3. As was pointed out there, the image contrast of this model is somewhat too sharp and too large. These effects were compensated for by an increased effective measuring distance and a decrease of the overall strength of the tip field. First the measurement was deconvolved by the simulated tip field. Then the effective distance and the multiplication factor for the tip field were determined by fitting the deconvolved field with the field of a vortex calculated using equation 5.18 with the parameters  $h = 140 \text{ nm}$ ,  $\lambda = 140 \text{ nm}$ ,  $\xi = 1.4 \text{ nm}$ . A good fit was obtained for an effective distance of 147 nm, and a tip-field strength that was a factor 0.49 smaller than the simulated field (compare the solid and the dotted line in figure 5.6c).

The fitted calibration allows the prediction of the accuracy with which different

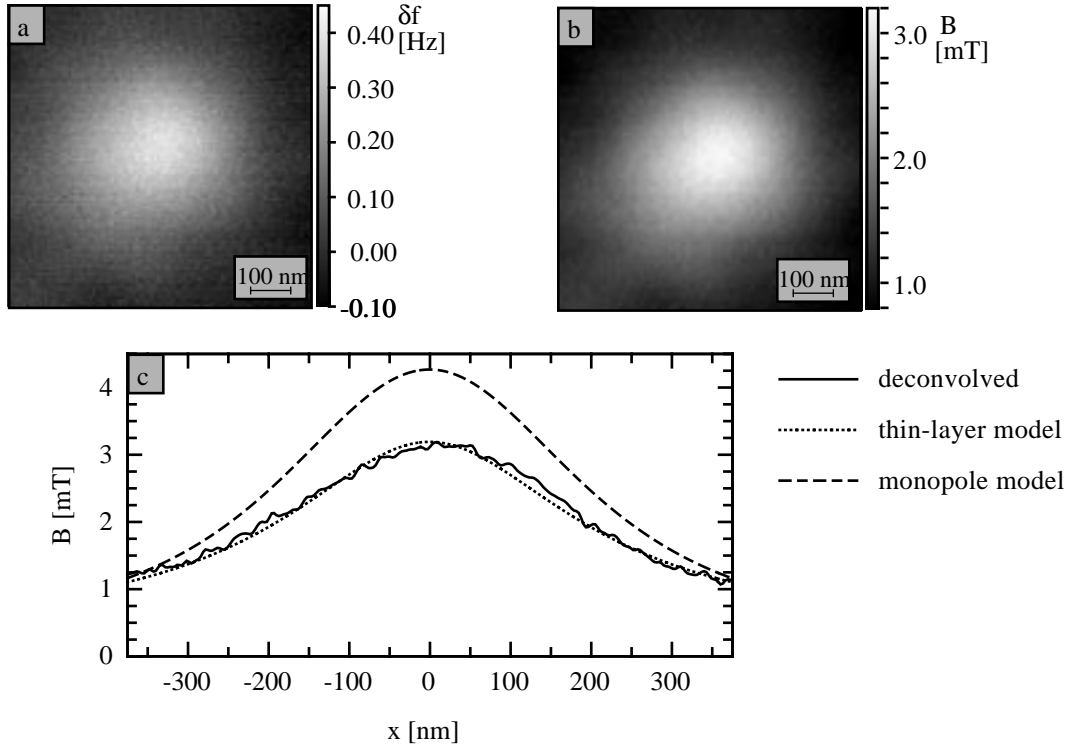


Figure 5.6: Fit of the flux density distribution of a single vortex. a single vortex in 140 nm thick layer of  $\text{YBa}_2\text{Cu}_3\text{O}_{7-x}$ .

- a) Original measurement.  
 b) Deconvolved flux density at an effective tip-sample distance of 147 nm.  
 c) Line-sections from the deconvolved flux density (solid line), the flux density calculated using equation 5.18 (dotted line) and the flux density of the monopole model of a vortex (dashed line).

models and parameter sets can be distinguished from one another, based on the measurement data. An often used approximation of the stray field distribution of the vortex far away from its core is a point monopole with charge  $2\phi_0$ , located at a distance  $\lambda$  below the surface of the superconductor. The flux distribution of this model is drawn in figure 5.6c as a dashed line. Clearly, the stray field of the simple model is significantly different from the field calculated using equation 5.18: the peak field is much larger, and it decays much more rapidly.

By evaluation of the behavior of the integrated squared deviation between the calculated field and the ‘measured’ field as a function of  $\lambda$  and  $\xi$ , it was found that the detection limit for changes in the value of  $\lambda$  is mainly determined by the amount of topography artifacts in the image and the accuracy with which the tip-to-sample distance can be determined. The accuracy of the absolute determination of  $\lambda$  is mainly limited by the accuracy of the tip-calibration, which is currently approximately 10%. Changes in the magnitude of  $\xi$  on the other hand, can only be determined if the value of  $\lambda$  is known, and even then only if  $\xi$  increases by more than a factor of 4. Nevertheless,  $\xi$  may still be determined by measurements with a better resolution, or in supercon-

ductors with lower  $\kappa$  values. However, one should realize that in this case of low  $\kappa$  values, a more sophisticated model is needed, as the approximations used to calculate the vortex stray field become questionable and the Meissner-type vortex contrast may give a non-negligible contribution to the overall contrast.

# Chapter 6

## Conclusion

In the following, the most important results of each chapter will be discussed, and suggestions for further work will be made.

### 6.1 Instrument

The signal-to-noise ratio of the static and dynamic measurement modes was investigated theoretically and experimentally. The surprising result was found that, theoretically, the static measurement mode is superior to the dynamic measurement mode for the normal operating conditions of the magnetic force microscope if one only considers noise due to thermal vibrations of the cantilever. However, this thermal noise limit is not reached experimentally in the static measurement modes, making the dynamic modes superior from the signal-to-noise point of view. Experimentally, it was shown that, apart from signal-to-noise ratio considerations, equivalent information is contained in the in the cantilever deflection measured in the static mode and the resonance frequency shift measured in the dynamic mode with small vibration amplitudes. Furthermore, it was shown that the image contrast of dynamic mode measurements changes when the vibration amplitude becomes too large. It may be interesting to study the contrast formation of dynamic modes with large vibration amplitudes in future work, as these modes should have a higher signal-to-noise ratio for stray field components that vary on a large length scale.

### 6.2 Contrast Formation

The contrast formation mechanism of magnetic force microscopy was investigated in the case when the modification of the sample by the stray field of the tip is negligible. It was shown that the contrast formation mechanism can be described elegantly in Fourier space. It was demonstrated that a non-zero angle between the normals of the cantilever surface and the normal of the sample surface creates a distortion in the image contrast, and that this distortion can easily be removed by an operation in Fourier space.

A method for calibrating the MFM signal was proposed that uses calibration measurements on a perpendicularly magnetized sample. A calibration function of the instrument is determined by a deconvolution of the measured signal with a simulation

of the stray field of the sample. The simulated stray field is calculated from a magnetization pattern that is estimated from the MFM measurement. The accuracy of the calibration was improved by averaging over several calibration measurements, and by the use of an iterative procedure, in which the found calibration function is used to obtain a more accurate estimate of the sample magnetization pattern. The difference was calculated between the calibration measurements and simulations, obtained using the calibration function. This difference is still too large to be completely explained by the statistical errors in the calibration function, which indicates that the calibration can be further improved. A possible source of the remaining difference is the implementation of the deconvolution operation of the calibration measurement with the simulated measurement as a division in Fourier space. It is expected that more advanced numerical methods for finding the the calibration will give a more accurate result.

It was shown that the stray field of the tip can be calculated from the calibration of the instrument. It was found that the flux density at the end of the tips, used in the experiments described here, is of the order of 10 mT, and decays rapidly with increasing distance from the tip.

The contrast predicted by the calibration functions was compared to the contrast predicted by some simple tip models. Furthermore, measurements were made on a different sample than the sample on which the instrument was calibrated to test the accuracy of the contrast predicted by the calibration function. These measurements show the same shape and size of the contrast as the contrast calculated using the instrument calibration. The contrast of a microfabricated silicon type tip was compared to the contrast of a electron beam induced deposition (EBID) type tip. It was found that the EBID type tip has a higher resolution and a lower stray field than the microfabricated Si type tip. Thus, the calibration of the tips can help to optimize the MFM tips. The comparison of the calibration functions to some simple tip models showed these simple models do not explain the measured image contrast quantitatively, and in some cases even give a qualitatively wrong result.

The measurement sensitivity of the MFM was calculated for the microfabricated silicon type tip and compared to the sensitivity scanning Hall probe and scanning SQUID microscopes. It was found that at room temperature, the MFM has a better sensitivity than Hall probes at magnetization wavelengths shorter than  $1.4\ \mu\text{m}$ . In the LHe temperature range, the MFM is more sensitive than the SQUID microscope for wavelengths shorter than  $4\ \mu\text{m}$ , and more sensitive than the scanning Hall microscopes for wavelengths shorter than  $0.85\ \mu\text{m}$ .

It is expected that the magnetization of ultrathin magnetic films and nanostructures can be measured using calibrated MFM. To get more confidence in the calibration method, it would be interesting to compare the stray field of the MFM tip determined from the instrument calibration function to the stray field determined by other methods, such as Lorentz microscopy or electron holography. Finally, calibrated MFM can be used to locally apply a known field to a sample. This could be used to map the sensitivity of field sensors.

### 6.3 MFM on Ferromagnetic Samples

Calibrated measurements were used to analyze the magnetization structure of domains in Cu/Ni/Cu/Si(001) samples. It was hoped that the occurrence of a surface domain structure would give direct evidence that the surface anisotropy of these samples favors a magnetization oriented perpendicular to the sample surface. Analysis of measurements on a sample containing 200 nm of Ni showed that its stray field distribution is similar to that of a sample with domains, magnetized perpendicular to the sample surface, but the magnitude of the stray field is a factor 0.6 smaller than the stray field of such perpendicular domains. Comparison of the distribution and magnitude of the measured stray field to the stray field of model magnetization structures showed that no surface domain structure exists in these samples. However, no definitive statement can be made on which alternative magnetization structure occurs, without evaluation of the energies of the different magnetization structures. This would require finite element calculations, which are beyond the scope of this thesis. Measurements on a sample containing 15 nm of Ni illustrates the importance of good measurement quality,<sup>1</sup> as it is not possible to perform reliable quantitative analysis on this sample, due to modification of the sample by the tip.

A possible method for the direct determination of the surface anisotropy would be the determination of the susceptibility, and thereby the anisotropy, of these samples as a function of the depth in the sample. This can be done from measured force–distance curves, using a similar method as was proposed by Coffey for determining the penetration depth in superconductors.

### 6.4 MFM on Superconducting Samples

A method was presented that allows the calculation of the interaction between a tip with an arbitrary stray field distribution and a superconducting sample. It was shown that this method can be applied to the calculation of both the interaction due to Meissner expulsion of the stray field of tip and the interaction between the tip and the stray field emanating from a vortex.

The shift in resonance frequency due to the Meissner repulsion was calculated for a microfabricated silicon type lever as a function of distance for samples with different penetration depths and thicknesses. It was shown that with present tips, it should be possible to determine the penetration depth from the frequency shift–versus distance measurements with an accuracy of approximately 10 nm.

To quantify the size of a vortex, two definitions of its magnetic radius were proposed: the  $1/e$  radius and the weighted average radius. It was shown that for large values of the Ginsburg–Landau parameter  $\kappa$ , the radius of the vortex decreases asymptotically towards zero or to the penetration depth, depending on the definition of the vortex radius. Furthermore, the dependence of the vortex radius on the sample thickness was calculated. It was shown that the vortex radius increases significantly for thicknesses below one third of the penetration depth.

The theory of the tip–sample interaction was used to analyze the vortex contrast for

---

<sup>1</sup>i.e. measurements with a high signal–to–noise ratio and negligible modification of the sample.

YBCO samples. It was found that the vortex contrast is due to the interaction between the magnetic MFM tip and the stray field of the vortex, whereas the decrease in Meissner repulsion above the vortex core gives a negligible contribution to the contrast. It was shown that the calculation of the vortex stray field using the contrast theory presented here gives significantly different results than calculation using the simple model of a vortex as a point monopole with twice the flux of the superconducting flux quantum, located at a the penetration depth below the sample. From evaluation of the behavior of the difference between the measured and the simulated signal, it was concluded that it should be possible to determine changes in the penetration depth with an accuracy of a few nanometers as long as the influence of topography artifacts is negligible. Furthermore, it was found that the accuracy of the absolute value of the penetration depth is mainly determined by the accuracy of the calibration of the measurement. Thus, it is found that the present accuracy of the determination of the penetration depth, from the measurement of the vortex signal, would also be approximately 10 nm. In YBCO samples, the coherence length is too small to be determined from present measurements. Possibly, this can be done using measurements made with better magnetic tips at a smaller tip-to-sample distance.

As a suggestion for future work, it may be interesting to repeat the measurements of a vortex configuration as a function of temperature made by Bruno Stiefel with calibrated tips. These measurements are particularly interesting because they should show the change of the vortex stray field due to the increase in the penetration depth, the coherence length and the ratio between the sample thickness and the penetration depth. The changes in the penetration depth and the coherence length should only result in a scaling of the lateral dimensions of the vortex stray field, whereas the change in the ratio between the sample thickness and the penetration depth should result in a change in the shape of the vortex stray field.



## Appendix A

# Stray Field of a Magnetic Layer in Fourier Space

It is instructive to derive the relation between the sample magnetization, and the stray field of the sample, because this is not done very clearly in literature [29]. For a sample with a volume charge  $\rho$ , that is independent of the depth in the sample, and with a magnetic surface charge  $\sigma_{top} = -\sigma_{bottom} = \sigma$ , the differential equations for the scalar magnetic potential in Fourier space, can be given using the relations derived in section 3.2.1:

inside:	outside:
$\nabla^2 \phi_{M,i} = -\rho(\mathbf{k})$	$\nabla^2 \phi_{M,(a,b)} = 0$
$\phi_{M,i}(\mathbf{k}, z) = A_1(\mathbf{k})e^{kz} + A_2(\mathbf{k})e^{-kz} + \frac{\rho(\mathbf{k})}{k^2}$	$\phi_{M,a} = A_3(\mathbf{k})e^{-kz}$ (above sample) $\phi_{M,b} = A_4(\mathbf{k})e^{kz}$ (below sample)

Using the boundary conditions for  $z = 0$  and  $z = -d$ :

$$\phi_{M,i}(\mathbf{k}, z) = \phi_{M,(a,b)}(\mathbf{k}, z) \quad \text{and} \quad \frac{\partial^2 \phi_{M,i}(\mathbf{k}, z)}{\partial z^2} - \frac{\partial^2 \phi_{M,(a,b)}(\mathbf{k}, z)}{\partial z^2} = \sigma(\mathbf{k}) \quad ,$$

one finds:

$$\begin{aligned} A_1(\mathbf{k}) &= \frac{1}{2} \left( \frac{\sigma(\mathbf{k})}{k} - \frac{\rho(\mathbf{k})}{k^2} \right) \\ A_2(\mathbf{k}) &= -\frac{e^{-kd}}{2} \left( \frac{\sigma(\mathbf{k})}{k} + \frac{\rho(\mathbf{k})}{k^2} \right) \\ A_3(\mathbf{k}) &= -\frac{1 - e^{-kd}}{2} \left( \frac{\sigma(\mathbf{k})}{k} + \frac{\rho(\mathbf{k})}{k^2} \right) \\ A_4(\mathbf{k}) &= -\frac{1 - e^{kd}}{2} \left( \frac{\sigma(\mathbf{k})}{k} - \frac{\rho(\mathbf{k})}{k^2} \right) \end{aligned}$$

Inserting the  $A$ 's, one gets:

$$\phi_{M,i}(\mathbf{k}, z) = \left[ \frac{\rho(\mathbf{k})}{k^2} \left( 1 - e^{-kd/2} \cosh(k(z + d/2)) \right) \right]$$

$$+ \frac{\sigma(\mathbf{k})}{k} e^{-k d/2} \sinh(k(z + d/2)) \Big] \quad (\text{A.1})$$

$$\phi_{M,a}(\mathbf{k}, z) = \sinh(k d/2) \left( \frac{\rho(\mathbf{k})}{k^2} + \frac{\sigma(\mathbf{k})}{k} \right) e^{-k(z+d/2)} \quad (\text{A.2})$$

$$\phi_{M,b}(\mathbf{k}, z) = \sinh(k d/2) \left( \frac{\rho(\mathbf{k})}{k^2} - \frac{\sigma(\mathbf{k})}{k} \right) e^{k(z+d/2)} \quad (\text{A.3})$$

If it is assumed that the sample has a magnetic domain structure with a uniform magnetization,  $\mathbf{M}$ , throughout its thickness,  $d$ ,  $\rho$  and  $\sigma$  can be replaced by:  $\rho = -\nabla \cdot \mathbf{M} = -ik_x M_x - ik_y M_y$  and  $\sigma = M_z$ :

$$\begin{aligned} \mathbf{H}(\mathbf{k}) &= -\nabla \phi_{M,a}(\mathbf{k}) \\ &= -\frac{\nabla}{k} \sinh(k d/2) e^{-k(z+d/2)} \begin{pmatrix} -ik_x/k \\ -ik_y/k \\ 1 \end{pmatrix} \cdot \mathbf{M}(\mathbf{k}) \end{aligned} \quad (\text{A.4})$$

The demagnetizing energy density,  $E_d$ , can be calculated using the integral:

$$E_d = \frac{\mu_0}{2V} \left( \int_V \rho \phi_{M,i} dV + \int_S \sigma \phi_{M,i} dS \right), \quad (\text{A.5})$$

which can be written as the result two correlation operations of the scalar potential with the surface charge and the volume charge respectively, evaluated only at  $(x,y) = 0$ . Therefore, the integral can be written as an integral over the Fourier coefficients of this correlation operation in Fourier space:

$$\begin{aligned} E_d &= \frac{\mu_0}{8\pi^2 V_s} \int_{\mathbf{k}} \int_{-d}^0 \rho^*(\mathbf{k}) \phi_{M,i}(\mathbf{k}, z) dz + \sigma^*(\mathbf{k}) (\phi_{M,i}(\mathbf{k}, 0) - \phi_{M,i}(\mathbf{k}, -d)) d\mathbf{k} \\ &= \frac{\mu_0}{8\pi^2 V_s} \int_{\mathbf{k}} \frac{|\rho(\mathbf{k})|^2}{k^2} \left( d - \frac{2e^{-k d/2}}{k} \sinh(k d/2) \right) + \frac{|\sigma(\mathbf{k})|^2 2e^{-k d/2}}{k} \sinh(k d/2) d\mathbf{k} \\ &= \frac{\mu_0}{8\pi^2 V_s} \int_{\mathbf{k}} \frac{|\rho(\mathbf{k})|^2 k d + (|\sigma(\mathbf{k})| k)^2 - |\rho(\mathbf{k})|^2 (1 - e^{-k d})}{k^3} d\mathbf{k} \end{aligned} \quad (\text{A.6})$$

# Bibliography

- [1] P. Weiss. L'hypothèse du champs moléculaire et la propriété ferromagnétique. *J. de Phys.*, 6:661–690, 1907.
- [2] L. v. Hámód and P. A. Thiessen. über die Sichtbarmachung von Bezirken verschiedenen ferromagnetischen Zustandes fester Körper. *Z. Phys.*, 71:442–444, 1931.
- [3] F. Bitter. On inhomogeneities in the magnetization of ferromagnetic materials. *Phys. Rev.*, 38:1903–1905, 1931.
- [4] A. L. Schawlow, B. T. Matthias, H. W. Lewis, and G. E. Delvin. Structure of the intermediate state in superconductors. *Phys. Rev.*, 95:1344–1345, 1954.
- [5] G. Binnig, C. F. Quate, and Ch. Gerber. Atomic force microscopy. *Phys. Rev. Lett.*, 56:930–933, 1986.
- [6] Y. Martin and H. K. Wickramasinghe. Magnetic imaging by "force microscopy" with 1000Å resolution. *Appl. Phys. Lett.*, 50:1455, 1987.
- [7] J. J. Saenz, N. Garcia, P. Grütter, E. Meyer, H. Heinzelmann, R. Wiesendanger, L. Rosenthaler, H. R. Hidber, and H.-J. Güntherodt. Magnetic domain structure by measuring magnetic forces. *J. Appl. Phys.*, 62:4293–4295, 1987.
- [8] A. Moser, H. J. Hug, I. Parashikov, B. Stiefel, O. Fritz, A. Baratoff, H. Thomas, H.-J. Güntherodt, and P. Chaudhari. Observation of single vortices condensed into a vortex-glass by magnetic force microscopy. *Phys. Rev. Lett.*, 74:1847–1850, 1995.
- [9] A. Hubert and R. Schäfer. *Magnetic Domains. The Analysis of Magnetic Domain Structures*. Springer-Verlag, Postfach 311340, D-10643 Berlin, Germany, 1998.
- [10] B. Stiefel. *Magnetic Force Microscopy at Low Temperatures in Ultra High Vacuum. Application on High Temperature Superconductors*. PhD thesis, Universität Basel, 1998.
- [11] Hans J. Hug, B. Stiefel, P. J. A. van Schendel, A. Moser, S. Martin, and H.-J. Güntherodt. A low temperature ultra high vacuum scanning force microscope. *Rev. Sci. Instr.*, 70:3625–3640, 1999.
- [12] E. Meyer and H. Heinzelmann. Scanning force microscopy (sfm). In R. Wiesendanger and H.-J. Güntherodt, editors, *Scanning Tunneling Microscopy II*, volume 28 of *Springer Series in Surface Science*. Springer-Verlag, Tiergartenstrasse 17, D-6900 Heidelberg, Germany, 1992.
- [13] F. J. Giessibl. Forces and frequency shifts in atomic-resolution dynamic-force microscopy. *Phys. Rev. B*, 56:16010–16015, 1997.
- [14] C. V. Heer. *Statistical Mechanics, Kinetic Theory, and Stochastic Processes*. Academic Press New York and London, 111 Fifth Avenue, 10003 New York, USA, 1992.
- [15] D. Rugar, H. J. Mamin, and P. Guethner. Improved fiber-optic interferometer for atomic force microscopy. *Appl. Phys. Lett.*, 55:2588–2590, 1989.

- [16] L. Abelmann, S. Porthun, M. Haast, C. Lodder, A. Moser, M. E. Best, P. J. A. van Schendel, B. Stiefel, H. J. Hug, G. P. Heydon, A. Farley, S. R. Hoon, T. Pfaffelhuber, R. Proksch, and K. Babcock. Comparing the resolution of magnetic force microscopes using the camst reference sample. *J. of Magn. Magn. Mater.*, 190:135–147, 1998.
- [17] T. R. Albrecht, P. Grütter, D. Horne, and D. Rugar. Frequency modulation detection using high- $Q$  cantilevers for enhanced force microscope sensitivity. *J. Appl. Phys.*, 69(2):668–673, 1991.
- [18] S. Porthun, L. Abelmann, S. J. L. Vellekoop, J. C. Lodder, and H. J. Hug. Optimization of lateral resolution in magnetic force microscopy. *Appl. Phys. A*, 66:1185–1189, 1998.
- [19] S. Porthun. *High resolution magnetic force microscopy: Instrumentation and application for recording media*. PhD thesis, University of Twente, 1996.
- [20] ThermoMicroscopes, 1171 Borregas Avenue, Sunnyvale, CA 94089, USA.
- [21] Nanosensors, Dr. Olaf Wolter GmbH, IMO–Building, Im Amtmann 6, D-35578 Wetzlar–Blankenfeld, Germany.
- [22] M. Rührig, S. Porthun, and J. C. Lodder. Magnetic force microscopy using electron-beam fabricated tips. *Rev. Sci. Instr.*, 165:3225, 1994.
- [23] Thomas Zuber. EBD–Spitzen für hochauflösende Raum– und Tieftemperatur Magnetkraftmikroskopie. Master’s thesis, Universität Basel, 1997.
- [24] H. J. Hug, B. Stiefel, P. J. A. van Schendel, A. Moser, R. Hofer, S. Martin, H.-J. Güntherodt, S. Porthun, L. Abelmann, J. C. Lodder, G. Bochi, and R. C. O’Handley. Quantitative magnetic force microscopy on perpendicularly magnetized samples. *J. Appl. Phys.*, 83:5609–5620, 1998.
- [25] E. Stoll and O. Marti. Restoration of scanning–tunneling–microscope data blurred by limited resolution, and hampered by  $1/f$ -like noise. *Surf. Sci.*, 181:222, 1987.
- [26] J. Saenz, N. Garcia, and J. C. Slonczewski. Theory of magnetic imaging by force microscopy. *Appl. Phys. Lett.*, 53:1449–1451, 1988.
- [27] D. Rugar, H. J. Mamin, P. Güthner, P. Lambert, J. E. Stern, I. McFadyen, and T. Yogi. Magnetic force microscopy: General principles and application to longitudinal recording media. *J. Appl. Phys.*, 68:1169, 1990.
- [28] M. Mansuripur and R. Giles. Computation of fields and forces in magnetic force microscopy. *IEEE Trans. Magn.*, 25:3467, 1989.
- [29] C. Schönenberger and S. F. Alvarado. Understanding magnetic force microscopy. *Z. Phys. B*, 80:373–383, 1990.
- [30] B. J. Roth, N. G. Sepulveda, and J. P. Wikswo. Using a magnetometer to image a two-dimensional current distribution. *J. Appl. Phys.*, 65:361, 1989.
- [31] R. J. Wijngaarden, K. Heeck, H. J. W. Spoelder, R. Surdeanu, and R. Griessen. Fast determination of 2d current patterns in flat conductors from measurement of their magnetic field. *Physica C*, 295:177–185, 1998.
- [32] Ch. Jooss, R. Warthmann, A. Forkl, and H. Kronmüller. High-resolution magneto-optical imaging of critical currents in  $YBa_2Cu_3O_{7-\delta}$  thin films. *Physica C*, 299:215–230, 1998.
- [33] D. W. Abraham and F. A. McDonald. Theory of magnetic force microscope images. *Appl. Phys. Lett.*, 56:1181–1183, 1990.
- [34] H. J. Williams, R. M. Bozorth, and W. Shockley. Magnetic domain patterns on single crystals of silicon iron. *Phys. Rev.*, 75:155–178, 1949.

- [35] H. J. Hug, Th. Jung, H.-J. Güntherodt, and H. Thomas. Theoretical estimates of forces acting on a magnetic force microscope tip over a high temperature superconductor. *Physica C*, 175:357–362, 1991.
- [36] W. Gutmannsbauer, H. J. Hug, and E. Meyer. Scanning probe microscopy for nanometer inspection and industrial applications. *Microelectronic Engineering*, 32:389–409, 1996.
- [37] P. Grütter, Y. Liu, and P. LeBlanc. Magnetic dissipation force microscopy. *Appl. Phys. Lett.*, 71(2):279–281, 1997.
- [38] Y. Liu, B. Elleman, and P. Grütter. Theory of magnetic dissipation imaging. *Appl. Phys. Lett.*, 71:1418–1420, 1997.
- [39] H. J. Hug, A. Moser, I. Parashikov, B. Stiefel, O. Fritz, H.-J. Güntherodt, and H. Thomas. Observation and manipulation of vortices in a  $\text{YBa}_2\text{Cu}_3\text{O}_7$  thin film with a low temperature magnetic force microscope. *Physica C*, 235–240:2695–2696, 1994.
- [40] A. Moser, H. J. Hug, B. Stiefel, and H.-J. Güntherodt. Low Temperature Magnetic Force Microscopy on High- $T_c$ -Superconductors. *J. of Magn. Magn. Mater.*, 190–192(4):114–123, 1998.
- [41] I. N. Bronstein, K. A. Semendjajew, G. Musiol, and H. Mühlig. *Taschenbuch der Mathematik*. Verlag Harri Deutsch, Frankfurt am Main, Thun, 4th edition, 1999.
- [42] E. O. Brigham. *The Fast Fourier Transform*. Prentice–Hall, 1974.
- [43] W. H. Press, B. P. Flannery, S. A. Teukolsky, and W. T. Vetterling. *Numerical Recipes in Pascal*. Cambridge University Press, 1989.
- [44] R. D. Gomez, E. R. Burke, and I. D. Mayergoyz. Component–resolved imaging of surface magnetic fields. *J. Appl. Phys.*, 75:5910–5912, 1994.
- [45] S. Foss, R. Proksch, E. D. Dahlberg, B. Moskowitz, and B. Walsh. Localized micromagnetic perturbation of domain walls in magnetite using a magnetic force microscope. *Appl. Phys. Lett.*, 69:3426–3428, 1996.
- [46] D. Belliard, A. Thiaville, S. Lemerle, A. Lagrange, J. Ferré, and J. Miltat. Investigation of the domain contrast in magnetic force microscopy. *J. Appl. Phys.*, 81(8):3849–3851, 1997.
- [47] R. Madabhushi, R. D. Gomez, E. R. Burke, and I. D. Mayergoyz. Magnetic Biasing and MFM Image Reconstruction. *IEEE Trans. Magn.*, 32(5):4147–4149, 1996.
- [48] T. Chang, M. Lagerquist, Jian-Gang Zhu, J. H. Judy, P. B. Fischer, and S. Y. Chou. Deconvolution of magnetic force images by fourier analysis. *IEEE Trans. Magn.*, 28:3138–3140, 1992.
- [49] J.-G. Zhu, X. Lin, and R. C. Shi. Magnetic force microscopy image restoration technique for removing tip dependence. *J. Appl. Phys.*, 83(11):6223–6225, 1998.
- [50] D. G. Streblichenko, M. R. Scheinfein, M. Mankos, and K. Babcock. Quantitative magnetometry using electron holography: Field profiles near magnetic force microscope tips. *IEEE Trans. Magn.*, 32:4124–4129, 1996.
- [51] R. P. Ferrier, S. McVitie, A. Gallagher, and W. A. P. Nicholson. Characterisation of MFM Tip Fields by Electron Tomography. *IEEE Trans. Magn.*, 33(5):4062–4064, 1997.
- [52] H. J. Mamin, D. Rugar, J. E. Stern, B. D. Terris, and S. E. Lambert. Force microscopy on magnetization patterns in longitudinal recording media. *Appl. Phys. Lett.*, 53:1563–1565, 1988.
- [53] Viola Barwich. Magnetische Anisotropien von Cu/Ni/Cu–Schichtsystemen. Master’s thesis, Universität Basel, 1998.

- [54] A. Oral, S. J. Bending, and M. Henini. Real-time scanning hall probe microscopy. *Appl. Phys. Lett.*, 69:1324–1326, 1996.
- [55] K. A. Moler, J. R. Kirtley, R. Liang, D. Bonn, and W. N. Hardy. Scanning squid microscopy of sparsely twinned  $\text{YBa}_2\text{Cu}_3\text{O}_{7-\delta}$ . *Phys. Rev. B*, 55(18):12753–12758, 1997.
- [56] K. Ha. *Magnetoelastic Coupling in Epitaxial Cu/Ni/Cu/Si(001) Thin Films*. PhD thesis, Massachusetts Institute of Technology, 1999.
- [57] K. Ha and R. C. O’Handley. Nonlinear magnetoelastic anisotropy in Cu/Ni/Cu/Si(001) films. *J. Appl. Phys.*, 85(8):5282–5284, 1999.
- [58] E. P. Wohlfahrt. Iron, cobalt and nickel. In E. P. Wohlfahrt, editor, *Ferromagnetic Materials*, volume I. North-Holland Publishing Company, 1980.
- [59] G. Bochi, C. A. Ballentine, H. E. Inglefield, C. V. Thompson, R. C. O’Handley, H. J. Hug, B. Stiefel, A. Moser, and H.-J. Güntherodt. Perpendicular magnetic anisotropy, domains, and misfit strain in epitaxial  $\text{Ni/Cu}_{1-x}\text{Ni}_x/\text{Cu/Si}(001)$  thin films. *Phys. Rev. B*, 52:7311–7321, 1995.
- [60] R. Jungblut, M. T. Johnson, J. aan de Stegge, A. Reinders, and F. J. A. den Broeder. Orientational and structural dependence of magnetic anisotropy of cu/nic/cu sandwiches: misfit interface anisotropy. *J. Appl. Phys.*, 75(10):6424–6426, 1994.
- [61] J. W. Matthews. Accommodation of misfit between single-crystal films of beta -cobalt and copper. *Thin Solid Films*, 5(5/6):118–125, 1970.
- [62] H. E. Inglefield, C. A. Ballentine, G. Bochi, S. S. Bogomolov, R. C. O’Handley, and C. V. Thompson. *Proceedings of the MRS Spring 1993 Meeting, San Francisco, CA.*, 308:765, 1993.
- [63] S. Blügel. Magnetische Anisotropie und Magnetostriktion (Theorie). In *Magnetische Schichtsysteme*, 30. IFF Ferienkurs. Forschungszentrum Jülich GmbH, 1999.
- [64] H. Thomas. private communication to Dr. H. J. Hug, 1995. University of Basel, Switzerland.
- [65] C. Kittel. Physical theory of ferromagnetic domains. *Rev. of Mod. Phys.*, 21(4):541–583, 1949.
- [66] M. Mansuripur. Demagnetizing field computation for dynamic simulation of the magnetization reversal process. *IEEE Trans. Magn.*, 24(7):2326–23268, 1988.
- [67] J. Kaczer, M. Zelezný, and P. Šuda. Transitional periodic domain structure in thin films of magnetically uniaxial materials. *Czech. J. Phys. B*, 13:579–585, 1963.
- [68] B. Kaplan and G. A. Gehring. The domain structure in ultrathin magnetic films. *J. of Magn. Magn. Mater.*, 128:111, 1993.
- [69] G. Bochi, H. J. Hug, D. I. Paul, B. Stiefel, A. Moser, I. Parashikov, H.-J. Güntherodt, and R. C. O’Handley. Magnetic domain structure in ultrathin films. *Phys. Rev. Lett.*, 75:1839–1843, 1995.
- [70] H. J. Hug, G. Bochi, D. I. Paul, B. Stiefel, A. Moser, I. Parashikov, A. Klicznik, D. Lipp, H.-J. Güntherodt, and R. C. O’Handley. Magnetic domain structure in ultrathin Cu/Ni/Cu/Si(001)-films. *J. Appl. Phys.*, 79:5609–5614, 1996.
- [71] C. Kooy and U. Enz. Experimental and theoretical study of the domain configuration in thin layers of  $\text{BaFe}_{12}\text{O}_{19}$ . *Philips Res. Rep.*, 15:7–29, 1960.
- [72] R. C. O’Handley and J. P. Woods. Static magnetization direction under perpendicular surface anisotropy. *Phys. Rev. B*, 42:6568–6573, 1990.

- [73] M. W. Muller. Distribution of the magnetization in a ferromagnet. *Phys. Rev.*, 122:1485–1489, 1961.
- [74] J. G. Bednorz and K. A. Müller. Possible high  $T_c$  superconductivity in the Ba-La-Cu-O system. *Z. Phys. B*, 64:189–193, 1986.
- [75] O. Fritz, M. Wülfert, A. Wadas, H. J. Hug, H.-J. Güntherodt, and H. Thomas. Magnetic field and order parameter of an anisotropic type II superconductor with an isolated flux line. *Phys. Rev. B*, 47:384–389, 1993.
- [76] M. W. Coffey. Closed form magnetostatic interaction energies and forces in magnetic force microscopy. *J. Phys. A: Math. Gen.*, 28:4201–4211, 1995.
- [77] M. W. Coffey. Theory of inverse magnetic force microscopy of superconductors in half-space geometry. *Phys. Rev. Lett.*, 83(8):1648–1651, 1999.
- [78] J. C. Wei, L. Hong, and T. J. Yang. Magnetic force signal of vortex creation in type-II superconducting thin films. *Physica C*, 280:311–316, 1997.
- [79] M. W. Coffey. Fundamental inversion problem for the magnetic-force microscopy of superconductors. *Phys. Rev. B*, 57(18):11648–11653, 1998.
- [80] M. W. Coffey and E. T. Phipps. Vortices in stratified superconductors: Application to magnetic force microscopy. *Phys. Rev. B*, 53(1):389–401, 1996.
- [81] J. R. Clem. Simple model for the vortex core in a Type II superconductor. *J. Low Temp. Phys.*, 18:427, 1975.
- [82] R.P. Huebener. *Magnetic Flux Structures in Superconductors*. Springer-Verlag, 1979.
- [83] J. R. Clem. Two-dimensional vortices in a stack of thin superconducting films. a model for high-temperature superconducting multilayers. *Phys. Rev. B*, 43:7837–7846, 1991.
- [84] A. M. Chang, H. D. Hallen, H. F. Hess, H. L. Kao, J. Kwo, A. Sudbo, and T. Y. Chang. Scanning hall probe microscopy of a vortex and field fluctuations in  $\text{La}_{1.85}\text{Sr}_{0.15}\text{CuO}_4$ . *Europhys. Lett.*, 20:645–650, 1992.
- [85] D. Yu. Irz, V. N. Ryzhov, and E. E. Tareyeva. Vortex-vortex interaction in a superconducting film of finite thickness. *Phys. Lett. A*, 207:374–378, 1995.
- [86] J. Pearl. Structure of superconductive vortices near a metal-air interface. *J. Appl. Phys.*, 37(11):4139–4141, 1966.
- [87] B. Dam, J. Rector, M. F. Chang, S. Kars, D. G. Groot, and R. Griessen. Laser ablation threshold of  $\text{YBa}_2\text{Cu}_3\text{O}_{6+x}$ . *Appl. Phys. Lett.*, 65:1581–1583, 1994.





# Acknowledgments

The work in this thesis could not have been performed without the support of many people, who I would like to thank at this point.

First of all, I thank professor Güntherodt for making the low-temperature scanning force microscopy project possible by his continuous support in even the most dire times.

I thank professor Güntherodt and professor Meyer for agreeing to be referee for my thesis.

Of course, the instrument would never have been built without the persistence of Hans Hug, who taught me that nothing doesn't work without a reason, and that this reason can always be found. He is also responsible for getting me to Basel, for which I am very thankful.

I also thank Hans, Regina Hoffmann and Mark Lantz for critically reading the manuscript of this thesis. Without them, the text this thesis would have been (even more) unreadable

In addition to them, I would like to thank all other past and present co-workers in the LTSFM group, who shared the best and the worst moments with me, and whose contributions can be found in all parts of this thesis: Sascha Martin, Andreas Moser, Alexander Klicznik, Bruno Stiefel, Ralph Herzog, Daniel Renggli, Thomas Zuber, Viola Barwich, Oliver Knauff and Peter Kappenberger.

I thank all past and present members of Groups of Güntherodt and Meier and the electronics lab for making the last three and a half years a pleasant time. Specifically, I would like to thank Frau Vetter for taking care of everything and everyone.

Many other people of the University of Basel have helped me. I would like to thank:

- The people from the Mechanical workshops, for constructing all kinds of small and large parts,
- Professor Schönenberger for use of his electron microscope for imaging tips,
- Professor Guggenheim and Daniel Matthys for their help with growing EBID tips using their electron microscope.

Of the people from outside the university, I should first thank Cock Lodder of the In-

formation Storage and Technology Group at the University of Twente, whose course on materials science got me involved in this field in the first place. Then I should also thank Steffen Porthun, who introduced me to both the theory and the praxis of the magnetic force microscope, and Leon Abelmann who provided the CAMST reference sample, and whom it is always a pleasure to meet and discuss with.

Furthermore, I would like to thank the visitors, whose stay in our group has been a welcome change in the daily routine:

- Bob O'Handley and Kin Ha, of the Massachusetts Institute of Technology, for providing the Cu/Ni/Cu samples, and for many discussions on magnetism, anisotropy and everything.
- Jan Aarts of the Camerling-Onnes Laboratory in Leiden
- Thomas Ihn and Jörg Rychen of the ETH Zürich, whom I wish the best of luck with the construction of their low temperature scanning probe microscope.

I also thank Bernhard Dam for providing the YBCO samples.

I thank my parents for always stressing the importance of intellectual growth, and for enthusiastically supporting me, even when moving to another country.

Finally, I thank Agnes Howald, who has had to endure the long working hours that were needed to finish this thesis. The time spent with her has always refreshed and inspired me.

# Curriculum Vitae

3. May 1972 Born in Ugchelen, The Netherlands, Son of Johannes Antonius Joseph van Schendel and Antonia Wilhelmina Maria van Schendel–Smits.
- 1978-1984 Elementary school “Touwladder”, Ugchelen The Netherlands.
- 1984-1990 Gymnasium “Veluws College”, Apeldoorn, The Netherlands.
- 1990-1995 Study of Electrical Engineering at the University of Twente, The Netherlands
- Dec. 1995 MSc. Thesis: “The Shape and Size of Magneto–optically Written Domains in CoNi/Pt Multilayers”
- 1996-1999 Ph.D. thesis in Physics at the University of Basel, Switzerland under Prof. Dr. H.-J. Güntherodt

# Publications

- Q. Meng, D. M. Donnet, P. J. A. van Schendel and J. C. Lodder: *Optimisation of CuNi/Pt Multilayers Compared with Co/Pt Multilayers for Thermomagnetic Writing*, Proceedings of Magneto-Optical Recording International Symposium '96 (MORIS '96), J. Mag. Soc. Japan Vol. 20 Supplement S1: 53–56, (1996)
- P. J. A. van Schendel, S. Porthun, D. M. Donnet and J. C. Lodder: *Shape Characterisation of Magneto-Optically Written Domains Using Parametric Fourier Descriptors*, Proceedings of Magneto-Optical Recording International Symposium '96 (MORIS '96), J. Mag. Soc. Japan Vol. 20 Supplement S1: 373–376, (1996)
- L. Abelmann, S. Porthun, M. Haast, C. Lodder, A. Moser, M. E. Best, P. J. A. van Schendel, B. Stiefel, H. J. Hug, G. P. Heydon, A. Farley, S. R. Hoon, T. Pfaffelhuber, R. Proksch and K. Babcock: *Comparing the resolution of magnetic force microscopes using the CAMST reference sample*, J. Magn. Magn. Mat. 190: 135–147 (1998)
- H. J. Hug, B. Stiefel, P.J.A. van Schendel, A. Moser, R. Hofer, S. Martin, H.-J. Güntherodt, S. Porthun, L. Abelmann, J.C. Lodder, G. Bochi and R.C. O'Handley: *Quantitative Magnetic Force Microscopy on Perpendicularly Magnetized Samples*, J. Appl. Phys. 83: 5609–5620 (1998).
- H. J. Hug, B. Stiefel, P. J. A. van Schendel, A. Moser, S. Martin, and H.-J. Güntherodt: *A low temperature ultra high vacuum scanning force microscope*, Rev. Sci. Instr. 70:3625–3640, (1999).
- H. J. Hug, P. J. A. van Schendel, B. Stiefel, Ch.Loppacher, S. Martin, H.-J. Güntherodt, J. M. Huijbregtse, B. Dam, and R. Griessen: *Understanding Vortex Imaging by MFM*, submitted to Phys. Rev. B.,
- P. J. A. van Schendel, H. J. Hug, B. Stiefel, S. Martin, and H.-J. Güntherodt: *A Method for the Calibration of Magnetic Force Microscopy Tips*, submitted to J. Appl. Phys.